Effects of Increasing Laser Power on Microstructure Formed during Selective Laser Melting of Co-29Cr-6Mo Alloy

Kourosh Darvish

A thesis submitted to Auckland University of Technology in fulfilment of the requirements for the degree of Doctor of Philosophy (PhD)

2018

School of Engineering, Computer and Mathematical Sciences

Abstract

Powder-bed fusion Selective Laser Melting (SLM) is the major metal additive manufacturing method capable of producing parts of highly complex geometries. It has been shown to be a promising manufacturing technique for the fabrication of biomedical (implant) and aerospace structure parts, in particular F75 Co-29Cr-6Mo alloy parts. For biomedical and aerospace applications, high mechanical integrity of parts is required. For this, knowledge on process control of SLM to attain suitable microstructure needs to be gained. Early in this study, preliminary SLM experiments were conducted using the default parameters advised by the machine manufacturer. Our preliminary results have shown that tensile elongation and fatigue strength values satisfied the requirement of ASTM F75 standard. However, they were lower than the values of the alloy made from other conventional manufacturing processes. Our examination has clearly shown that lack of fusion (LOF) was a major defect causing the property values to be significantly lower. Since a track width in SLM additive process ranges 50-150 μm, the related LOFs are in micron size and thus are treated as part of microstructure.

As will be detailed, it was clear that how laser power, *P*, affects the amount and size distribution of LOF was not well understood. It was also clear that solidification mode and grain growth during SLM have not been well studied. Solidification microstructure is widely understood to relate well to mechanical properties. Furthermore, there has basically been no study to understand the effect of *P* on grain growth and on cell size. *P* is perhaps the most important parameter in SLM. Thus, the overall aim of this research is to study how *P* affects the amount and size of LOF and affects grain growth during SLM of F75 Co-29Cr-6Mo alloy.

Experimentally, SLM samples were made with *P* ranging from 180 – 360 W while other parameters (scan speed = 700 mm/s, powder layer thickness = 30 μm, hatch spacing =

125 μm and scan direction rotating 67° after each layer) are kept unchanged. Surface features of tracks were examined using a scanning electron microscope (SEM). Metallography samples were then prepared. LOF sizes were determined primarily using an imaging analysis software (ImageJ) but LOFs were also revealed through the use of Synchrotron radiation. Solidification microstructures were studied using the SEM and cell sizes were determined based on the measurements made using SEM images. Growth orientation of cells was determined using electron back-scatter diffraction (EBSD) and by analysis of the data. Finally, cell size is theoretically related to temperature gradient and growth rate, attempting to understand the thermal condition of solidification, which cannot be experimentally determined.

It has been found that, when the base condition (P = 180 W) was used, the track was insufficient to overlap and prevent LOF. Increasing P improves the shape stability of the tracks. Cross-sections of tracks have showed a gradual increase in size but the shape of tracks has not changed significantly suggesting that the mode of melting over the 180-360 W range was conduction. It will be shown that there is a rapid decay in the amount of LOF as P increases from 180 W to 220 W, as the result of the geometrical effect of the track size on overlapping coverage. Residual LOF has remained even when P has increased to > 300W. For the first time, evidence of large size spatters causing large size LOF will be presented and the high laser beam penetrating capability to reduce the spatter effect is discussed.

On grain growth, we will also start by presenting the results for the base condition (P = 180 W). Our observation of epitaxial growth in the melt/track boundary has agreed well with that observed in literature. Also agreeing with most in literature is the cell growth immediately from the melt boundary, without a planar zone. We will explain this based on constitutional supercooling criteria, considering the growth velocity and thermal gradient. Epitaxial growth has been found to have two possible crystallographic

orientations of <100>: either a continuation of the same <100> orientation as in previous track or a change of 90° to another <100> orientation. The selection is in response to scan direction-dependent heat flux direction. The crystal growth direction in relation to heat flux direction also explains that a grain (a group of cells) after epitaxial growth could either stop or continue to the track surface. No equiaxed grains were observed, and this can be explained by the continuation of cellular growth in the whole track.

We have found that over the whole 180-360 W, the mode and the overall preferred grain growth is not significantly affected by P. This is because, as has already been explained, the shape of track did not change sufficiently over the range of P values used and thus growth direction did not vary significantly during epitaxial growth. It has also been found that P does not affect cell size (λ_1). This suggests, since growth rate (R) relates to scan speed (v) which is unchanged, P does not significantly affect the temperature gradient of the solidification front (G). From the measured λ_1 and estimated R, G and thus cooling rate ($\dot{T}$) can be estimated following the commonly used primary arm spacing model. The estimated G and $\dot{T}$ which could not be directly measured will be compared with those predicted by simulation and the estimated $\dot{T}$ will also be compared with those determined by using an emperical relationship from literature. The present results aid the understanding of the thermal condition during SLM solidification relative to the wide range of other solidification processes.

Acknowledgement

The acknowledgements are an optional but essential part of this thesis because it allows appreciation to go to those that have helped and given their support during the years that it takes to construct and complete a PhD.

I would first like to thank my supervisor Professor Zhan Chen for his help, guidance, encouragement and particularly patience during the experimental works and, more importantly, during the writing of this thesis. Thanks must also go to Dr Tim Pasang for his support.

To Mark Masterston for his consistent technical support and for all the equipment and training provided. Patrick Connor for his commitment in laboratory work especially during SEM and EBSD training.

The biggest motivating factor for me has been the love and support of my friends. My best support during this journey has been Alastair, I would like to thank him with my deepest gratitude. My sincere thanks go to Fahimeh, Umberto, Juri and Nithin for being a very good company during all these years. I am also grateful to my friends Sarang, Nina Mana, & Karl for their encouragement, suggestions and motivation.

I would also like to thank my parents for their support, financially and for always understanding the things I said, the things I didn't say, and the things I never planned on telling you. And last but not least, my sister Shaghayegh, for her encouragement over the last however many years. Thank you for understanding me always.

List of Publication

The following papers have been published over the course of this research.

Journal Paper:

- Darvish, K., et al., Selective laser melting of Co-29Cr-6Mo alloy with laser power 180–360W: Cellular growth, intercellular spacing and the related thermal condition. Materials Characterization, 2018. 135: p. 183-191.

- Chen, Z.W., M.A.L. Phan, and K. Darvish, Grain growth during selective laser melting of a Co–Cr–Mo alloy. Journal of Materials Science, 2017: p. 1-13.

- Darvish, K., Z.W. Chen, and T. Pasang, Reducing lack of fusion during selective laser melting of CoCrMo alloy: Effect of laser power on geometrical features of tracks. Materials & Design, 2016. 112: p. 357-366.

Conference Paper:

- Chen, Z.W., K. Darvish, and T. Pasang, Effects of Laser Power on Track Profile and Structure Formation during Selective Laser Melting of CoCrMo Alloy. Materials Science Forum, 2017. 879: p. 330-334.

Table of Content

List of Figures

List of Tables

Nomenclature

η	Angle Between Normal to S/L Interface and Building Direction
ϕ	Angle between the Cell Growth in [010] in a n-1 Layer Track and the Normal Direction of the Track Boundary
θ	Angle Between the Growth Directions of cell to the Normal Direction of Track Boundary
θ̇	Angle between the scan tracks and the direction normal to the cross section
σ_{min}	Minimum Stress
σ_{max}	Maximum Stress
r	Relative Density
Γ	Gibbs-Thomson Coefficient
ω	Angle Between the Direction Along the Elongated Cell and the Direction Normal to the Micrograph Plane
l_1	Cell Size
α̈	Absorptivity Coefficient
A_{tk}	Area of Track
CoCrMo	Cobalt Chromium Molybdenum (Co-29Cr-6Mo) by wt%
d	Beam Size
D	Thermal Diffusivity
D_L	Diffusion Coefficient of Solute in the Liquid,
E	Energy Density
f_{LOF}	LOF area fraction
G	Thermal Gradient
f_N	Frequency
h_{tk}	Height of Track
h	Layer Thickness
ΔH	Enthalpy Change

$\mathbf{K_{tc}}$	Thermal Conductivity
k	Partition Ratio
LOF	Lack of Fusion
$\mathbf{l_{mp}}$	Melt Pool Length
P	Laser Power
$\mathbf{P_{tk}}$	Track Penetration
R	Growth Velocity
$\mathbf{R_{load}}$	Load Ratio
$\mathbf{R_c}$	Critical Growth Velocity
$\mathbf{R_{tk}}$	Track Reinforcement
$\mathbf{q_e}$	External Heat Flux
SIMT	Strain-Induced Martensitic Transformation
$\mathbf{C_o}$	Solute-Content
T	Temperature
$\mathbf{\Delta T_0}$	Equilibrium Liquidus-Solidus Interval
TB	Track Boundary
$\dot{T}$	Cooling Rate
v	Scanning Velocity
w	Hatching Space
$\mathbf{W_{tk}}$	Width of Track

Attestation of Authorship

I hereby declare that this submission is my own work and that, to the best of my knowledge and belief, it contains no material previously published or written by another person (except where explicitly defined in the acknowledgements), nor material which to a substantial extent has been submitted for the award of any other degree or diploma of a university or other institution of higher learning.

Auckland Signature 

1 Introduction and Literature

1.1 Background of Selective Laser Melting (SLM) of Co-29Cr-6Mo Alloy

Additive manufacturing (AM) technology is well-known as one of the outstanding manufacturing methods that is based on the layer-by-layer material technology. This technology is defined as the procedure of fusing materials to fabricate objects from 3D model data, generally layer upon layer, as against subtractive manufacturing technologies.

AM is a field growing to maturity and shows great promise for manufacturing products with sophisticated geometries. AM technology can be used in aerospace and biomedical industries due to the layer-by-layer processing and the ability to manufacture small volumes of components without the need for tooling. Airbus Filton for instance is using AM machines which reinforces the argument that AM will grow in use for aerospace applications. However, looking over the research in the past three decades in AM, it becomes clear that there are limitations in mechanical properties which are inferior to conventionally fabricated materials. Considering that AM is on the rise, it is now a universal need to gain more knowledge in this field and study the cause of shorter life span of its products than the conventional methods [1-3].

Metal and alloys processing has become the latest trend in AM industry. As opposed to traditional manufacturing methods, metal additive manufacturing (MAM) is a unique material fabrication method for creating products based on incremental layer by layer procedure. Because of the layer by layer nature of this process, parts with complex geometry and structure with precision and accuracy which is not obtainable using traditional manufacturing techniques can be fabricated. Some of the advantages of MAM is given in Figure 1-1. Bone tissue engineering scaffold is an excellent example of usage

of MAM to mimic the interconnected porous network structure which is difficult to produce with conventional manufacturing techniques [4].

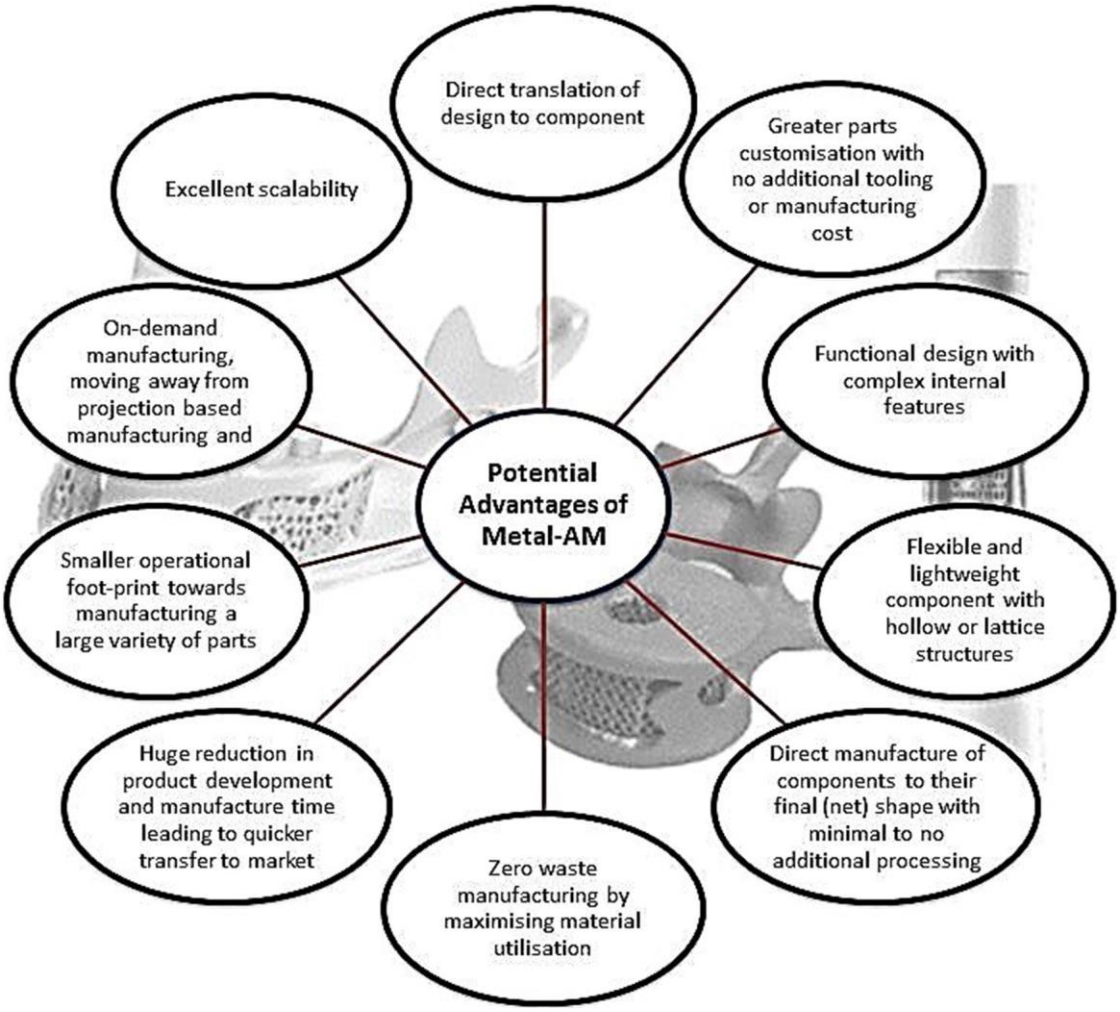

Figure 1-1 some potential advantages of MAM [4]

The theory of the combination of the MAM and biocompatible material is achievable due to the design-specific and material-specific system of MAM, in particular towards the specific clinical application such as hip or dental implants of patient. In the past decade, MAM has developed into the biomedical industry, and since then various studies have been done to enhance various quality characteristics of MAM in producing biomedical components.

However, owing to some limitations of MAM processes, MAM is not always the suitable choice for manufacturing. Slow build rate of this technique, high production costs, limited

number of alloy powders available and restricted size of the products are some of the limitations of this process. Also, parts can only be printed one at a time, preventing economics of scale, and poor mechanical properties such as low elongation and fatigue strength is another issue that has been reported in MAM and will be discussed more in the literature review in this chapter.

The current highlights of MAM categorised by the type of the layer for biomedical industries are divided into two primary groups; powder bed and powder-fed systems. Laser metal deposition, and laser engineered net shaping (LENS) are two types of powder-fed system. The laser process includes the heating of metallic powder particles to above the melting temperature that leads to formation of several melt pools which fuse together through a solidification process. Powder fed processes have high deposition rates and capable of producing large parts. However, parts fabricated using this method have a rough beaded surface that often requires machining to achieve the desired net shape.

Powder bed fusion systems apply thermal energy by either using a laser or electron beam to melt and fuse metallic powders together at certain parts of a powder bed. The powder bed method emphasizes the benefits including the capability to fabricate parts that are highly complex but with accuracy. It can also be used to fabricate parts without required support system, and a wide range of powders can be utilised in this system. Powder bed fusion technique is one of the first commercialized generations of AM techniques. Only a few types of powder bed techniques have the capability to process biocompatible power metals; selective laser melting (SLM), electron beam melting (EBM), and selective laser sintering (SLS) [5].

SLM as a division of laser-based powder bed fusion is a solid freeform fabrication process for producing three-dimensional (3D) parts with complex geometries by selectively melting successive layers of metallic powder particles on top of one another, employing the thermal energy radiated from a laser beam that is controlled by a computer.

Characteristics like high design flexibility, near-net-shape products, a high material utilization rate and time- and cost-saving make this method one of the most desirable manufacturing techniques in industry [6, 7].

SLM was developed in 2002 and was used for one of the earliest biomedical researches in the manufacturing of jaw and bone implants for dental and orthopedics applications. Nowadays SLM is one of the most well-known powder bed fusion processes in fabricating metallic biomaterials in comparison to other MAM methods.

The steps of SLM process illustrated in Figure 1-2 is as below:

1. The process starts by slicing the 3D CAD file data into thin layers, generating a 2D image of each layer similar to other MAM techniques.
2. Then a fine layer of powder particles is laid on the base plate connected to the piston.
3. The laser beam starts to scan the powder corresponds to the 3D CAD file data. The melt pool will form as a result of heating powder material above their melting temperature. Next the melt pool solidifies abruptly as the laser moves away.
4. After the scanning of first cross section completes, the building platform moves downwards by a quantity equal to the layer thickness.
5. The cycle starts again and a new layer of metal powder is deposited until the procedure is finished. At last the product will be cleaned and removed from the substrate.[8]

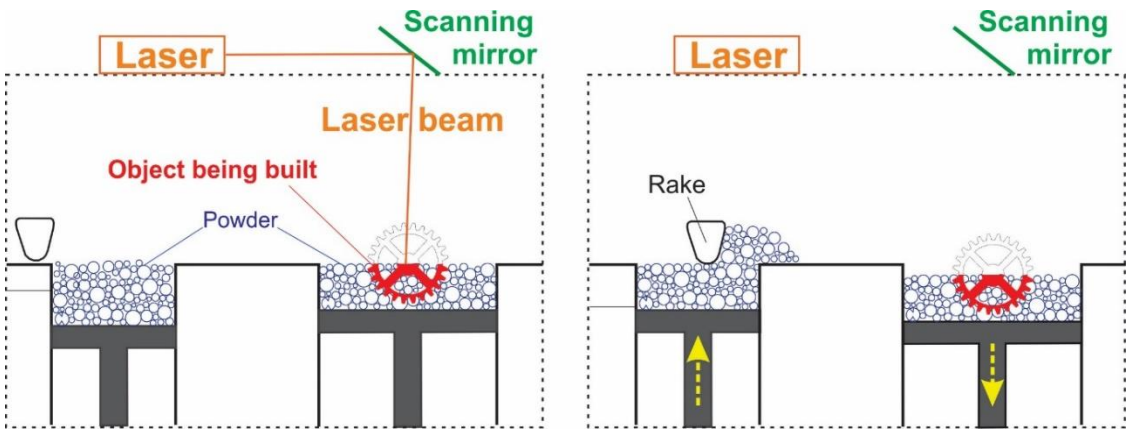

Figure 1-2 Schematic diagram illustrating the principle process inside the SLM chamber

Nowadays, metallic alloys are being used in various biocompatible devices. There are abundant sorts of metallic materials that are used in different industries, however only a limited number of them are biologically compatible to the human body for long term biocompatible applications. The biocompatibility property is one of the major issues in regard to the application of metallic materials. The continuous research on biocompatible metal suitable for SLM has helped to the development of biocompatible cobalt based materials. Cobalt-Chromium-Molybdenum (Co-Cr-Mo) alloy is a well-known cobalt based alloy which has widely been used in aerospace and biomedical areas in the past decades due to its excellent mechanical properties and biocompatibility. Because of the success of cobalt-based tool materials during WWI, they were then used in weld overlay form, plowshares, oil well drilling bits and internal combustion engines valves and valve seats. Newly the application has been widened up to joint and fracture fixation devices [9, 10].

Conventional Co alloys including the Co-29Cr-6Mo alloy used in this study are strengthened by a combination of carbides and solid solution strengthening. This has been explained in both ASM Specialty Handbook: Nickel. Cobalt, and their alloys and a review article “Wrought cobalt-based superalloys” in Journal of Materials Engineering and Performance. In the present study, C content is very low <0.05% and thus solute solution strengthening is the primary strengthening mechanism [11, 12].

Traditionally, investment casting and machining have been the processes for manufacturing CoCrMo alloy for dental and biomedical applications. However, fabrication techniques, such as casting, forging and cutting, are mainly difficult due to their high melting points of 1623-1723 K and high hardness. Also, unique size of each implant makes these processes expensive and time consuming [13]. With the strong activities of research and industrial applications of MAM, as reviewed by Koutsiukis et al. [14] CoCr alloys processed by SLM have been evaluated by various workers in recent

times. A decade ago, engineers at GE Aviation and France's Safran Aircraft Engines, began working on an innovative jet engine. After years of research and development a new fuel nozzle, Figure 1-3, was developed for Boeing's new 777X aircraft using cobalt alloys. However, this nozzle was too complex to be fabricated by conventional manufacturing process. Thus, MAM as an advanced manufacturing process capable of producing complex parts was proposed to produce this nozzle. it should be noted, getting to a level of technology to be able to make this product commercially available for the market took years of research on MAM [15] [16].

Figure 1-3 MAM fabricated GE fuel nozzle [16]

However, for using this alloy in biomedical and aerospace industries, this alloy has to show reasonable strength under static and cyclic loading. In fact, quality and reliability of SLM are currently a crucial issue for the technology. Despite the various advantages of SLM, fatigue resistance of as-built SLM components is inferior compared to traditionally fabricated parts from the same materials [17]. Therefore, before the application of this technology in medical or aerospace industry it is critical to understand what causes this low mechanical property.

SLM is a very dynamic process, with the melting and solidification behaviours affected significantly by both the part geometry and build strategy. Thus, there has been increasingly strong research effort on studying how SLM parameters affect the structure

and properties of products for medical/dental applications. During SLM, a part is built layer by layer and in each layer the high-speed scanning laser beam melts powders locally on its path, with the melt to solidify after the beam moves away, to form a dense layer. Thus, metal SLM may be viewed as a fusion welding on a very small scale at a very high speed of melting and solidification [1].

However, as reviewed by Frazier [18] and Uriondo et al. [19] there are a number of important challenges relating to AM part quantification process and defect detection. Increasingly, quality and reliability of parts manufactured by AM including SLM have been recognized as a crucial issue. In reviewing the work on AM defects and defect detection, Everton et al. [20] explain that a major defect is material discontinuity or lack of fusion (LOF) and their limited control and detection are a key barrier for the implementation of AM technologies. Figure 1-4 illustrates LOF between scan lines and solidified layers as the melt pool did not wet the underlying layer and the neighbouring scan lines. As a SLM part must normally require a very large "weld" distance, the amount of LOF can be high if how process control relating to the formation of LOF is not well understood and proper control is not made.

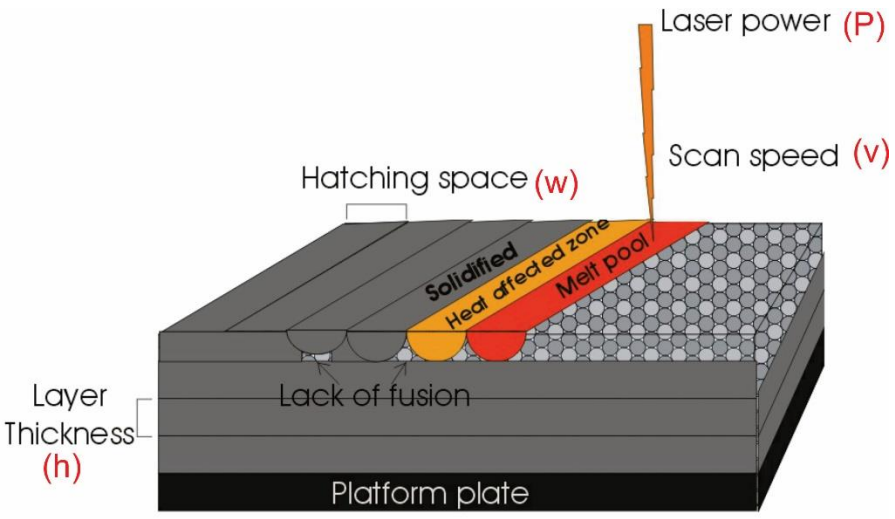

Figure 1-4 Schematic illustration of effective parameters in SLM

Since LOF is primarily caused by insufficient melting, it is expected that higher laser power (P) and lower scanning velocity (v) should aid melting of a larger amount of powder particles per unit time. This may be comparable to conventional fusion welding processes that the ratio, P/v, is the heat (energy) input from the heat source. In SLM, whether powder particles can be completely melted depends strongly on the volume of particles needed to be melted. This means in SLM smaller layer thickness (h) and smaller inter-scanline (hatch) spacing (w) should also be expected to promote a more complete melting of powder particles. Thus, energy for a unit volume of material in a unit time is suggestive of the amount of melting and has often been used. It relates to the major SLM parameters referred to as:

$$E = P / (v \times w \times h) \qquad \text{Equation 1-1}$$

As will be described, the literature review from studies at the time of the first part of the present research on LOF was insufficient and lacked a systematic view addressing some of the fundamental issues relating to it. It may be helpful to briefly outline a common LOF in SLM products. Figure 1-5a shows a gap between fusion boundaries in the CoCrMo sample which was built using the given parameter by SLM Renishaw machine. As Figure 1-5b illustrates, owing to the high aspect ratio of this LOF, it has the potential to serve as a source of preferential crack propagation and can adversely affect the mechanical properties of SLM parts. Thus, serious LOF should be a serious SLM quality issue.

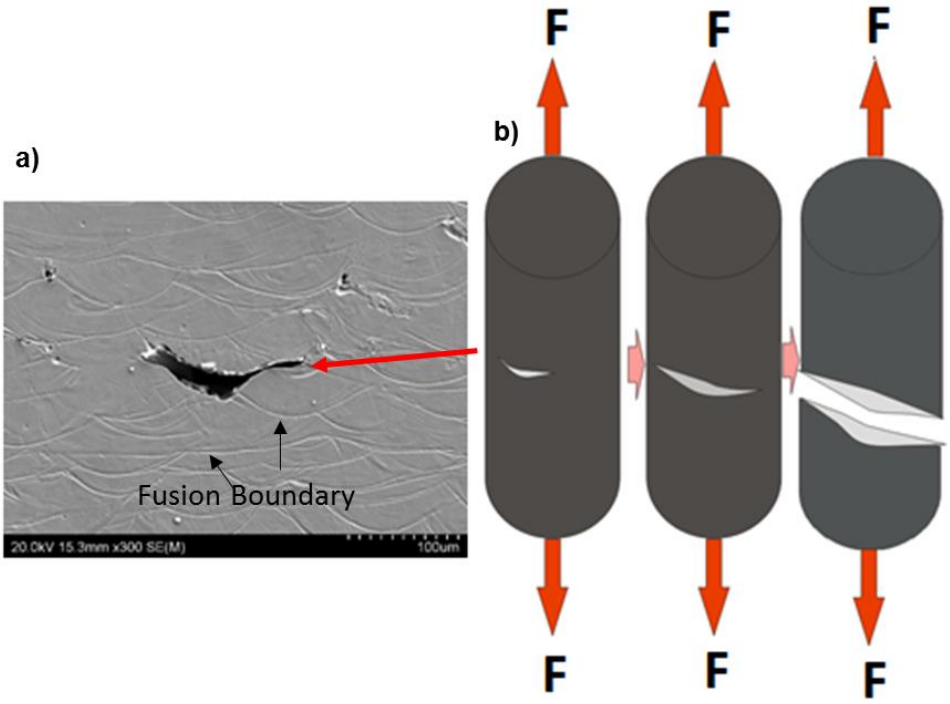

Figure 1-5 (a) LOF between fusion boundaries from the preliminary study on CoCrMo sample built using SLM, (b) effect of LOF on sample under loading

Furthermore, since microstructure of a part strongly effects the mechanical properties, for example strength and ductility, which influences the application of these parts in industry, it is crucial to study the microstructure of the material. The microstructure of SLM parts is different from conventional processes due to the rapid movement of the scanning beam. As has been shown in various studies using different materials, the grain structure/size and crystallographic texture of a SLM component depend on the melting and solidification of the melt pool which are influenced by the SLM processing parameters. Therefore, microstructure is a controlling factor on the mechanical properties of SLM products that can be controlled using SLM parameters [7] [21].

The above discussion briefly introduced the important effects of LOF and microstructure on the mechanical properties. In the following section, to illuminate the negative effect of LOF on mechanical properties, the results of the preliminary study on the tensile and fatigue properties are shown. This is followed by a review on the mechanical properties of different materials, CoCrMo in particular, in SLM to show how solidification

microstructure and LOF can significantly influence the mechanical properties of SLM products.

1.2 Two Major Microstructural Aspects of This Research (Preliminary Study)

In the preliminary stage the tensile and fatigue properties of CoCrMo samples using SLM process were made. Samples were fabricated using the default parameters specifically for Co-29Cr-6Mo alloy given by Renishaw: laser power 180W, scanning speed 700mm/s, hatching space 0.03mm and layer thickness 0.125mm and, the samples were built in a way that the long section is aligned to the building direction. Tensile samples built to the as specified dimensions of ASTM standards as shown in Figure 1-6.

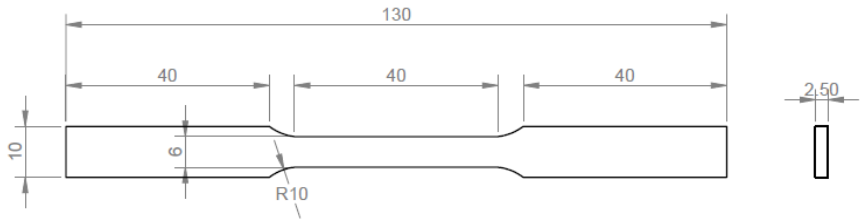

Figure 1-6 Dimension of tensile samples built using the default SLM parameters

Two tensile tests were performed on a Tinius Olsen H50KS tensile testing machine. The test was done using force of 50 KN at room temperature. Yield strength, ultimate tensile strength and elongation at fracture were measured according to the ASTM E8/E8M employing both an extensometer and the measured cross-head strain. As shown in Figure 1-7 the yield stress and UTS are determined to be around 600 MPa and 850 MPa respectively, with an observed sample elongation of 9.5%. Despite using the SLM energy density of 68.57 J/mm^3 in the SLM experiment, the elongation is 9.5% which is comparable to 11% elongation value in Takaichi et al.'s [22] experiment using energy density of 300 J/mm^3. The preliminary tensile elongation result presented satisfies the requirement of ASTM F75 standard, however, the elongation is lower than the elongation

of wrought CoCrMo which is around 20% [23], as will be illustrated soon this is influenced by the presence of LOF in the sample.

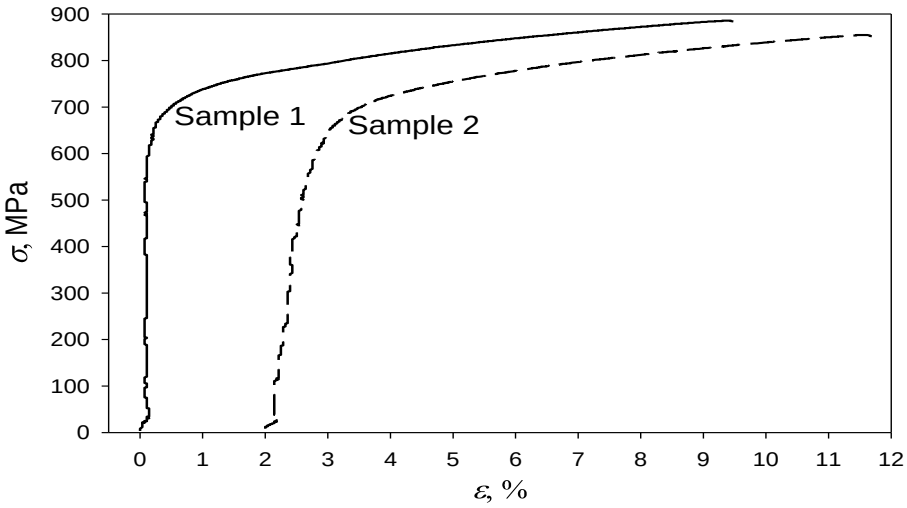

Figure 1-7 Stress-Strain curve of the as-built CoCrMo processed by SLM

Preliminary fatigue samples built to the as specified dimensions of ASTM standards as shown in Figure 1-8. Fatigue tests is performed as per ASTM E466-07 at a load ratio of $R_{load} = \frac{\sigma_{min}}{\sigma_{max}} = 0.1$ and frequency (f_N) of 20 Hz on a MTS fatigue machine at room temperature.

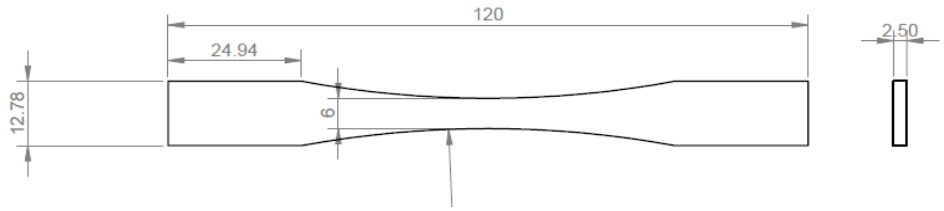

Figure 1-8 Dimension of fatigue samples built using the default SLM parameters

The fatigue behaviour of the vertical sample is shown in Figure 1-9. The fatigue life of as-built sample is low and, despite decreasing stress level from 500 MPa to 350 MPa the lifetime cycle increased negligibly from 25000 to 64000. At a low stress level of 180 MPa the lifetime cycle is only 730000, and the maximum stress level of run-out is 130 MPa which is extremely low. As will be shown and explained later, the presence of LOF in the

samples is likely to be the key contributor to the poor fatigue life compared to the wrought material with fatigue life of 624 MPa.

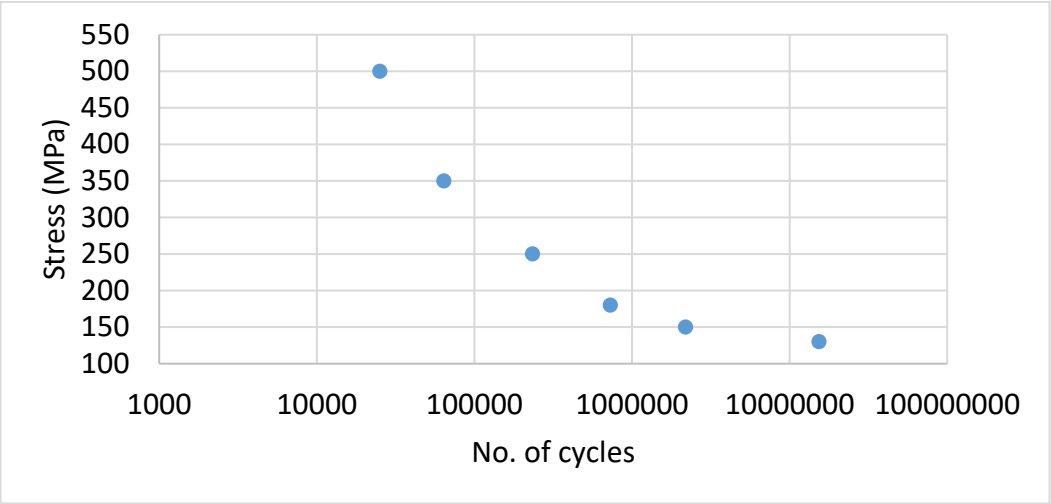

Figure 1-9 Measured S-N curve of as-built vertical sample processed by SLM

Unfortunately, the current knowledge on fatigue properties of CoCrMo alloys in AM is only limited to the data sheet given by EOS and Arcam companies. EOS and Arcam are two of the pioneers and leaders in the field of AM which have developed various commercialized AM machines. EOS claimed that using vertical as built samples, under 250 MPa stress amplitude and 44Hz testing frequency, the fatigue life would be approximately 10^7 and 10^6 cycles using 560 MPa and 660 MPa max stress, respectively, which is comparable to wrought CoCrMo with fatigue limit of 624 MPa [24]. Arcam [25] uses electron beam melting (EBM) for fabrication of samples. The fatigue limit of as-built samples were not given, but after hot isostatic pressing (HIP) and homogenisation (HOM) the fatigue limit using the rotating beam experiment reached 10 million cycles at 610 MPa load as Figure 1-10 shows. It is noticeable that although EOS claims that no post heat treatment was used, the fatigue limit is as high as the EBM manufactured sample with HIP treatment. Both companies claim that no machining or surface treatments have been used on the samples. It can be assumed that both machine manufactures have provided their best values of almost defect free samples, as a result the fatigue limits are

high and comparable to wrought material. Both manufacturers do not reveal any observation or analysis on the effect of surface condition, LOF or any heat treatment on fatigue limit.

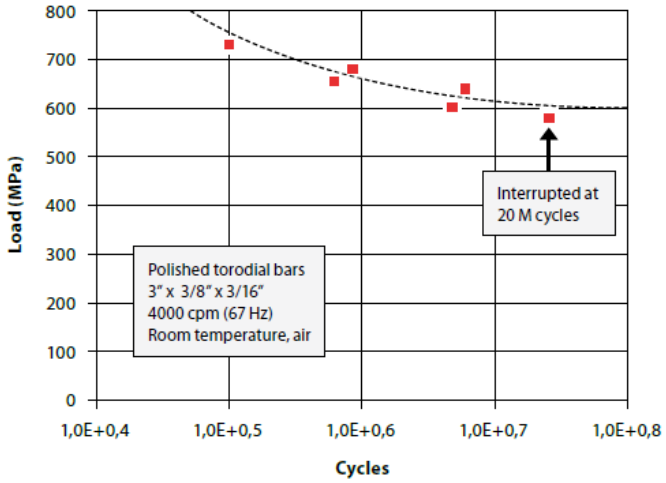

Figure 1-10 Arcam HIPed and homogenised CoCr under rotating beam fatigue test [25]

To investigate the reasons for having lower than the wrought elongation values and low fatigue strength, SEM analysis on fracture surface of tensile and fatigue samples is used. Figure 1-11 shows the SEM images taken from the fracture surface of vertical specimen after tensile test. A mixture of flat regions and step like regions, indicated by the white arrow, are observed in Figure 1-11(a). The flat surface observed in all the figures is likely to originate from LOFs that was formed during loading. The LOF shown in Figure 1-11 (c) has the size of 200 µm in diameter which is considerably larger than the hatching space (125 µm). Sub-size powder particles in a range of 5-15 µm in size which are smaller than the used powder particles with size of 15-45 µm for SLM processing of CoCrMo can be seen in Figure 1-11 (d). Although it is not clear at this stage but it is possible that these particles can be spatters of melt from melt pool that sinter to the solidified surface. However, for explaining the spatter formation a deeper examination on melt pool behaviour is required.

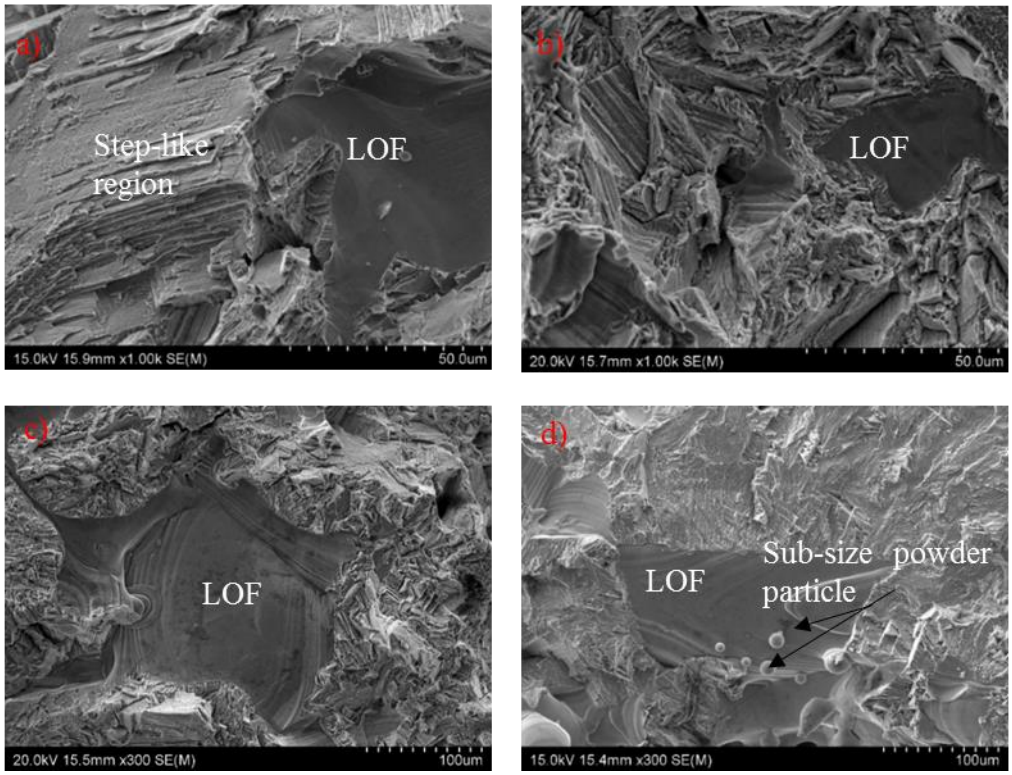

Figure 1-11 Fracture surfaces of the vertical SLM build after tensile testing (a) and (b) mix of flat and step like regions, (c) LOF with size of 200μm, (d) LOF with subsize powder particles

Solidification microstructure is another controlling factor on mechanical properties of MAM products. For instance, as indicated in Figure 1-12, in tensile test of cast CoCrMo alloy the crack propagates along the interfaces between γ-fcc and ε-hcp phases which leads to fracture. The ε-hcp phase is formed by strain-induced martensitic transformation (SIMT) of γ-fcc phase during loading [26]. Because of sensitivity of fracture to solidification microstructure, it is essential to understand the microstructure of the SLM processed alloy.

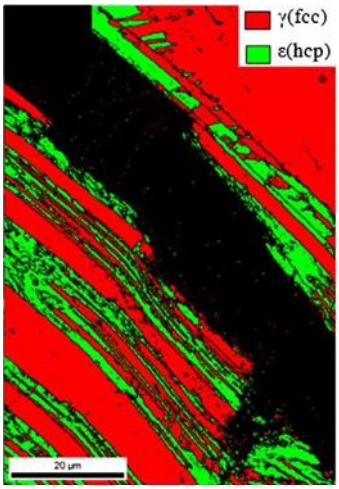

Figure 1-12 EBSD phase map of CoCrMo alloy strained in tension to 24.2%, showing the develop of fracture at the interface between the γ-fcc phase and strain-induced ε-hcp martensite. [26]

One main cause of the LOF is the track geometry of scan track and the sufficiency of overlapping and overlaying of tracks. Figure 1-13 is a schematic illustration of the dependency of micro LOF and the geometry of scan tracks. The scan tracks in Figure 1-13a & b are wavy and not stable in width which led to formation of LOF. The stable elongated tracks in Figure 1-13c have sufficient overlapping which omits the LOF formation. For supporting this relation more investigation on the geometry of scan tracks and LOF formation is needed. LOF is taken as a microstructure feature due to micro-scale size of it.

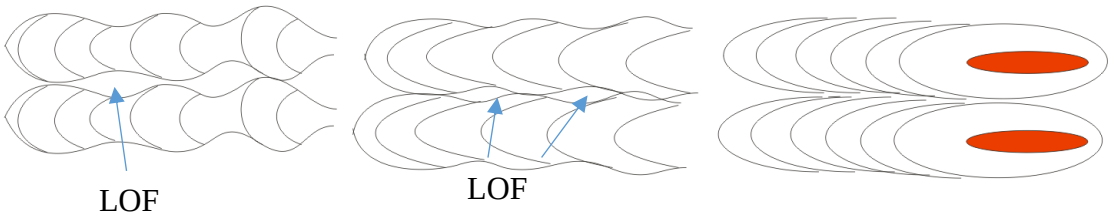

Figure 1-13 Effect of track geometry on LOF formation

To investigate the morphology and size of LOF, microstructure observation using SEM was conducted on the cross-section of preliminary tensile sample before fracture. The SEM image of vertical cross section parallel to the building direction is shown in Figure 1-14. Figure 1-14a & b shows different shapes of LOF in the specimen which as was

stated earlier can lead to early fracture of parts. LOF is a part of structure made using SLM, and the size of it is in the range of micron and can be as large as 200-300μm in size. Thus, it can be considered that LOF is a microstructure feature of SLM.

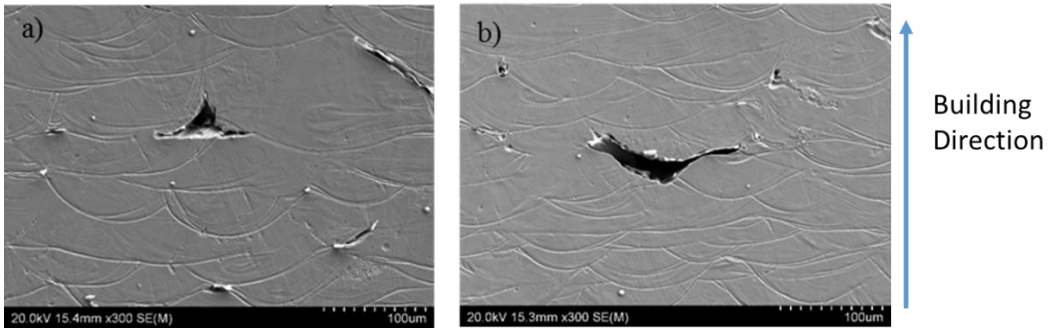

Figure 1-14 SEM images of microstructure of the SLM builds taken from the vertical cross section parallel to the building direction

As already stated, the dominant effect on tensile properties is the presense of LOF. Thus, we need to summarise the tensile data in relevant literature and examine the level of understanding in this aspect. There have been a number of studies in literature on tensile behaviour of CoCrMo alloys processed by SLM. SLM parameters, energy, building direction and tensile elongation of these studied are listed in Table 1-1. Building direction is considered vertical when the sample is built layer-by-layer on the grip section area and is considered horizontal when it is built on the long section of tensile sample. Elongation values vary considerably, from low 4.5% to high 16.4%. In the following, we evaluate the data in literature and make an attempt to improve the understanding of how SLM conditions affect tensile properties from the data provided by various researchers.

Table 1-1 Tensile elongation values reported by various sources

Ref.	Laser parameters	Building direction	Energy density	Elongation,ε
Takaichi et al. (CoCrMo) [22]	P=200W, H=0.2mm, v=50mm/s, L=0.05mm	Horizontal	400 J/mm3	4.5%
	P=200W, H=0.2mm, v=50mm/s, L=0.05mm	Vertical	400 J/mm3	10.7%
	P=200W, H=0.1mm, v=50mm/s, L=0.05mm	Vertical	800 J/mm3	16.4%
	P=150W, H=0.1mm, v=50mm/s, L=0.05mm	Vertical	600 J/mm3	15.5%
	P=100W, H=0.1mm, v=50mm/s, L=0.05mm	Vertical	400 J/mm3	12.2%
	P=150W, H=0.2mm, v=50mm/s, L=0.05mm	Vertical	300 J/mm3	11%
Song et al. (CoCrMo) [27]	P= 170W, H=0.08mm v=472mm/s, L=0.035mm	Vertical	128.63 J/mm3	3.6, 3.9 and 4.1%
	P= 170W, H=0.08mm v=472mm/s, L=0.035mm	Horizontal	128.63 J/mm3	5.6, 4.8 and 5.2%
Lu et al. (CoCrW) [28]	P=95W, H=0.07mm v=700mm/s, L=0.025mm, Line scan strategy	-	77.55 J/mm3	9.8%
	P=95W, H=0.1mm v=700mm/s, L=0.025mm, Island scan strategy	-	54.28 J/mm3	10%

As in the above table, elongation values vary considerly in Takaichi et al. [22] experiments. The elongation of vertical sample has the highest value at 10.7% and horizontal sample with 4.5%, respectively. As was stated by Takaichi, these results indicate that the mechanical properties of the SLM parts made along the different orientations are not identical, representing the anisotropy in the mechanical properties of SLM parts. The anisotropy of mechanical properties was claimed to be due to the unique SLM microstructure. However, there was no detail analysis on the effect of microstructure on elongation.

The possible reason for poor mechanical properties that was not mentioned in their study is the presence of defects particularly LOF in products. As can be illustrated and seen in Figure 1-15, LOF oriented between the fusion layers and can be anticipated that their deleterious impact is considerably more effective when they are perpendicular to the force direction. Thus, the orientation of LOF in vertical sample is more favourable for crack to grow than LOF in horizontal sample. However, in this case the elongation value of the vertical sample is lower than the horizontal sample which is contradictory to the data of Takaichi et al. which shows a higher elongation value for vertical sample (10.7%) than the horizontal one (4.5%). The other controlling factor is the amount of LOF in each layer. There is a possiblity that due to wider build area of horizontal sample there are more LOF on each of its layers than the vertical ones which led to lower tensile elongation in horizontal samples. As pointed out, Takaichi et al. have not considered the effect of LOF on tensile properties. As such, a thorough investigation into the size and amount of LOF in SLM processing using different SLM parameters is required.

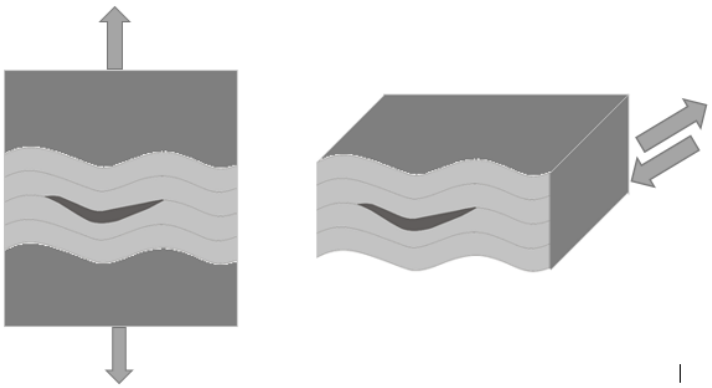

Figure 1-15 (a) vertical sample (b) horizontal sample, with LOF under tensile loading

Now we examine Song et al.'s data using Table 1-1. In Song et al.'s experiment [27], elongation values are low, ~ 4% for vertial and ~ 5% for horizontal built samples. The elongation values in their experiment are much lower than the Takaichi et al.'s experiment. Also, unlike Takaichi et al.'s result the value of vertical sample is slightly lower than the horizontal sample. Song et al. attributed the low values of elongation to

small grain sizes, although neither grain sizes were measured nor the meaning of grain sizes were clarified.

There is a possibility of having higher number of LOF in Song et al.'s experiment in comparison to Takaichi et al.'s experiment which can assist the crack propagation and results in lower elongation. Also, as LOF is more favourable of breakage in the vertical sample, the elongation of vertical samples should be lower than horiznotal samples. The high number of LOF can be related to the low energy input (128.63 J/mm^3) used by Song et al. which is about one third of the minmum energy (300 J/mm^3) input used in Takaichi et al.'s experiment.

Referring to Table 1-1, in Lu et al.'s investigation on CoCrW [28] the building orientation was not revealed but the elongation of CoCrW in both scanning strategies (line = 9.8%, Island= 10%) with employing approximately 60 J/mm^3 energy input is roughly the same as the elongation of vertical sample (10.7%) in Takaichi et al.'s experiment. Therefore, it is possible that both samples are built vertically. The rather poor ductility was explained by the presence of athermal ε-phase in the SLM product. The athermal ε-phase might induce stress concentration at their interfaces and/or grain boundaries which results in lower elongation and premature fracture [29]. Also, in Yamanaka et al.'s experiment on CoCrW alloys showed samples with less ε-phase have better ductility [30].

Although ε-phase can attribute to low elongation values, but round pores as illustrated in Figure 1-16 or LOF are seen to be the primary cause of low elongation. In addition, round unmelted particles on the outer surface of the samples may be responsible for poor elongation. It is possible that low energy input (60 J/mm^3) in Lu et al.'s experiment in comparison to Takaichi et al.'s energy input (>300 J/mm^3) might be the reason for the appearance of the claimed unmelted particles and round pores inside samples.

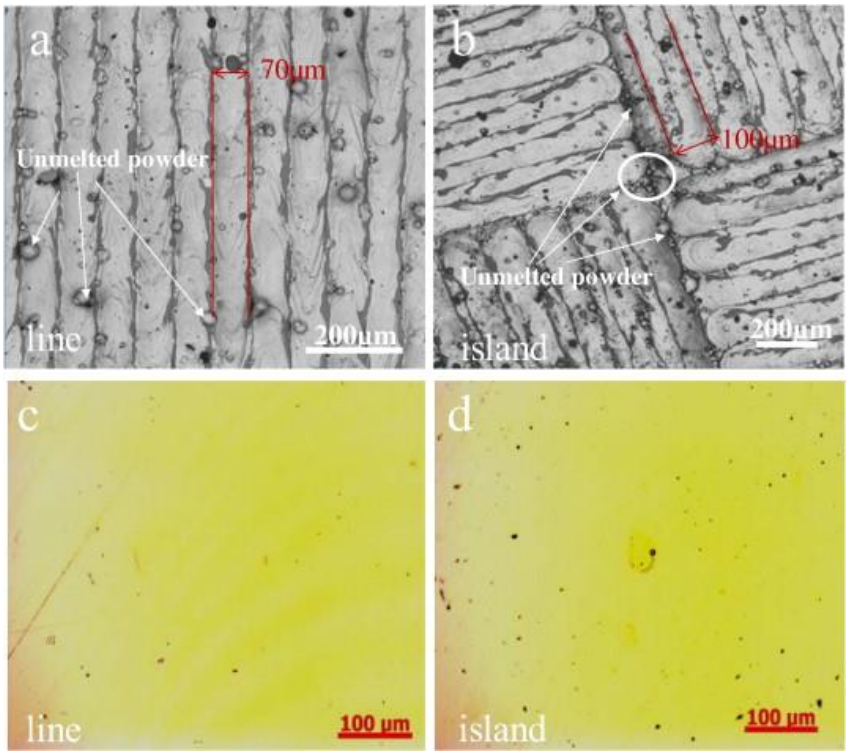

Figure 1-16 (a) surface morphology of unpolished line-formed alloy; (b) surface morphology of unpolished island-formed alloy; (c) optical micrograph of polished line-formed alloy; (d) optical micrograph of polished island-formed alloy from SLM work of Lu et. Al on CoCrW [28]

Figure 1-17 illustrates a summary of the energy densities and their corresponding elongation values that were discussed in this section. It is noticeable that in the experiment by Lu et al. the used energy inputs are 54.28 and 77.55 J/mm^3 which are approximately one sixth of the lowest energy input in Takaichi et al.'s experiment. But the elongations in both experiments are comparable, which is in contrast to Takaichi et al.'s claim that with increasing energy input the elongation should increase. In the mentioned studies LOF which has a significant effect on the mechanical propeties was not considered. Therefore, there is a lack of information on the size and amount of LOF and the effect of SLM condition on LOF formation. Thus, it is important to gain knowledge on how SLM parameters relate to the size and amount of LOF.

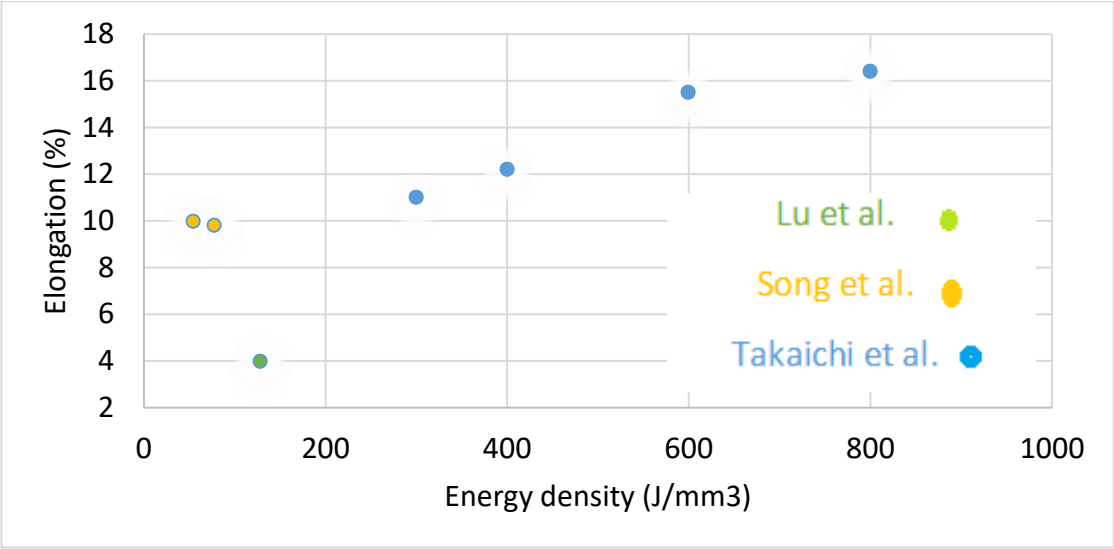

Figure 1-17 Energy density vs. elongation in processing of CoCr alloys using SLM

In general, during SLM a melt track is laid one next to another and then this track laying repeats in next layer. A track needs to lap sufficiently the previous one in order not to have LOF. Equation 1-1 suggests how process parameters may relate to the energy for melting during laser scanning. The melt track profile (shape and size and their consistency) should primarily determine whether sufficient lapping is achieved. If incomplete lapping/laying occurs, LOF results. LOF is a major defect in welding. SLM is a "welding" process and to build a small volume, a large distance of "welding" is required. Thus, how SLM parameters affect the track profile needs to be understood for minimizing the amount of LOF which is a microstructure feature and for a high build rate.

Microstructure development during the solidification stage of SLM needs to be understood significantly further as part of the effort for accelerating the deployment of SLM industrially, as explain by Babu [31]. The unique feature of SLM is the very small melt pool size (0.1-0.3 mm) and high scan speed (v = 0.5-1.5 m/s), together with the low chamber and base plate temperatures (< 200 °C). Thus, values of growth velocity (R) and temperature gradient (G) and the resulting cooling rate ($\dot{T} = G \cdot R$) are known to be very high during SLM solidification. In their comprehensive review on microstructural control of MAM materials, Collins et al. [32] suggest that laser power (P) is a major parameter

that can strongly affect G and thus $\dot{T}$. However, experimental data illustrating the P-G relationship may be seen lacking. Furthermore, solidification modes and microstructure formation during SLM of metallic alloys and of Co–Cr alloys in particular have not been sufficiently revealed and studied. Clearly, the understanding of microstructures formed is required for SLM Co–Cr to be applied more widely in biomedical fields, as corrosion and mechanical properties should relate closely to the microstructures of the SLM processed alloys.

As stated above, in SLM mechanical properties of products are significantly influenced by the refined microstructure caused from the rapid cooling and by formation of small solidification defects. However, as will be discussed more in literature review, the localized melting and solidification process which happens in SLM process is not yet fully understood. There is a lack of information on the solidification mechanism of CoCrMo alloy affected by rapid melting and cooling within the melt pool and requires further investigation. How laser power affects the microstructure evolution of SLM parts is another ambiguous area in SLM. Thermal gradient and cooling rate in the melt pool and their relationship with laser power are thus need to be studied.

Following the above introduction on SLM and two major microstructure aspects of it, and before detailing the aspects of this thesis; firstly, LOF formation and the effect of processing parameters on it is reviewed. In regard to unsatisfactory study in the understanding of LOF formation pointed out above, this research is performed with a motivation to observe and describe this feature and the effect of processing parameters on it during SLM processing of CoCrMo alloy. Secondly, a detailed review on spatter and how spattering in SLM can lead to LOF formation is given. Thirdly, limited knowledge and research on the microstructure development and the influence of laser parameter on the microstructure solidification in SLM are presented. It was planned to conduct crack propagation testing to investigate the effect of LOF and solidification

microstructure on the crack behaviour of CoCrMo products fabricated in SLM. However, because of the in-depth research and analysis on the microstructure of CoCrMo products and also the effect of laser power on it, which turned out to be conclusive for what was required, mechanical testing research section was exclude from my studies. Thus, the focus of last chapter is solely on microstructure of F75 CoCrMo.

For illuminating this area of research, a series of experiments and observations were conducted on CoCrMo parts built with different power values. Following the comprehensive literature reviews, the scope and sequences of this PhD research are given.

1.3 Effect of SLM Parameters on Lack of Fusion (LOF)

There has been a strong and continuous research effort on understanding how defects may form during SLM and how SLM parameters relate to the level of defects. Wei et al. [33] show, for AZ91D Mg alloy, trends of decreasing relative density (ρ) as either v or w increases and that using low v and small w values ρ can be close to 100% (but not 100%). As noted by them, high energy inputs resulted in serious evaporation. Thus, it is important that energy should be sufficiently high for achieving a high ρ value but not too high for causing undesirable outcomes. Furthermore, a low v value simply means a low production rate. Trend of increasing ρ when v decreases was also found for SLM of Al-10Si-0.3Mg alloy by Aboulkhair et al. [34] and is shown in Figure 1-18. The layer thickness, laser power and hatching space were kept constant at 40 µm, 100 W and 50 µm, respectively, while the scanning speed increased from 250 to 1000 mm/s.

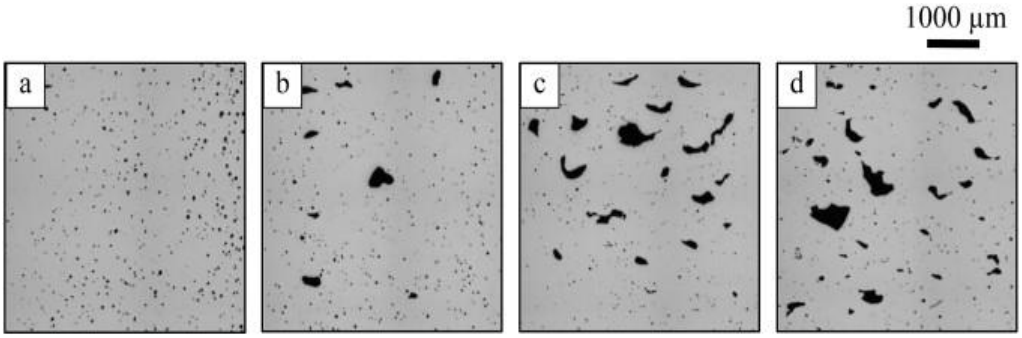

Figure 1-18 Evolution of LOF using Al-10Si-0.3Mg alloy with scanning speed: (a) 250 mm/s, (b) 500 mm/s, (c) 750 mm/s, and (d) 1000 mm/s while layer thickness 40µm, laser power 100W and hatching space 50µm were kept constant [34]

For the same Al alloy, Read et al. [35] observed the trend of decreasing porosity level as *E* increases, although the scatters in their data are generally very high. Figure 1-19 illustrates that the high porosity caused by the lack of consolidation is linked to the low energy density. The amount of porosity in the parts reduces with increasing the energy density. Nevertheless, between energy density levels of 60 J/mm^3 to 120 J/mm^3, the fraction of porosity is not influenced by the energy density and it is scattered. In this area of energy density other defects, such as keyhole formation owing to the evaporation of material has been observed within the material.

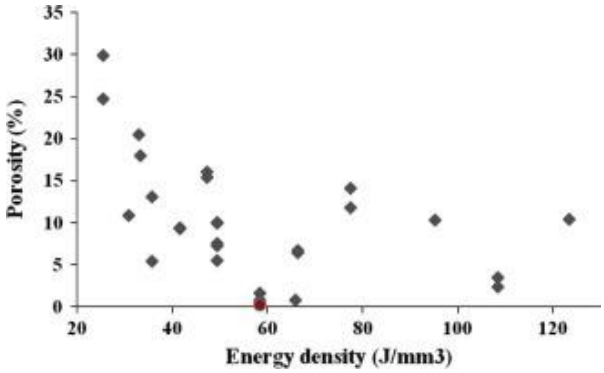

Figure 1-19 Porosity variation vs the energy density for AlSi10Mg alloy in SLM [35]

In Abele et al.'s experiment [36], it was shown that the porosity of specimens decreases by increasing energy density. Figure 1-20 reveals this in SLM of stainless steel powder. Also, there are numerous investigations considering the effect of SLM parameters on part density and process optimization. For instance, Gong et al. [37] studied the effect of laser power and scanning speed on porosity and density of Ti6Al4V. However, what these

studies did not reveal is the presence of microdefects like LOF which do not have a major influence on density of specimens but can be highly detrimental to the fatigue life and elongation. In other words, low porosity does not mean defect free. Accordingly, none of these studies show the effect of SLM parameters on LOF and how change of energy may influence the size, shape and formation of LOF.

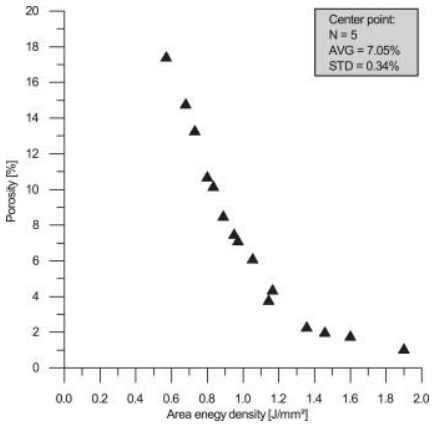

Figure 1-20 Influence of area energy density defined by Abele et al. on porosity of stainless steel [36]

In the research by Li & Gu [38], Figure 1-21 shows the microstructure of etched cross-sections of SLM CP Ti samples produced at different laser powers. It was revealed that at relatively low laser power (100 W), a large number of irregularly shaped micropores were observed between neighbouring layers but the cause of these micropores is not explained. Also, a few pores with near spherical shape can be seen in Figure 1-21a that were not described, but based on the appearance it can be suggested that they are gas pores that were unable to escape the melt during solidification. The main reason for the presence of gas pores in SLM produced parts is assumed to be the inert gas from the powder feedstock that has been imprisoned in the powder particles throughout the SLM processing [39].

When the power was increased to 150 W (Figure 1-21b), authors stated that dense, evenly distributed, and metallurgically bonded layers without any interlayer pores or cracks formed. However, it is clear that, a few planar LOFs denoted by red box are present. It

was explained by them that increasing energy input leads to wider and deeper melt pools which is accompanied with greater overlapping and re-melting that gives more opportunity to the trapped gas pores to escape. Thus, gas pore was not observed in Figure 1-21b & c.

When the power was further increased to 200 W, a number of planar LOF with an average length of 130 μm and a teardrop shape LOF were observed between neighbouring layers as shown in Figure 1-21c. However, Li & Gu claim that these pores are inter-layer cracks, and the cause is explained to be due to the high temperature gradient along the z-direction which led to thermal stress. Accordingly, thermal cracks tend to form between neighbouring layers to release stress in the z-direction. However, based on the shape, these pores are not similar to thermal microcracks, especially the teardrop pore which is similar to LOF between layers which was seen in Figure 1-21b.

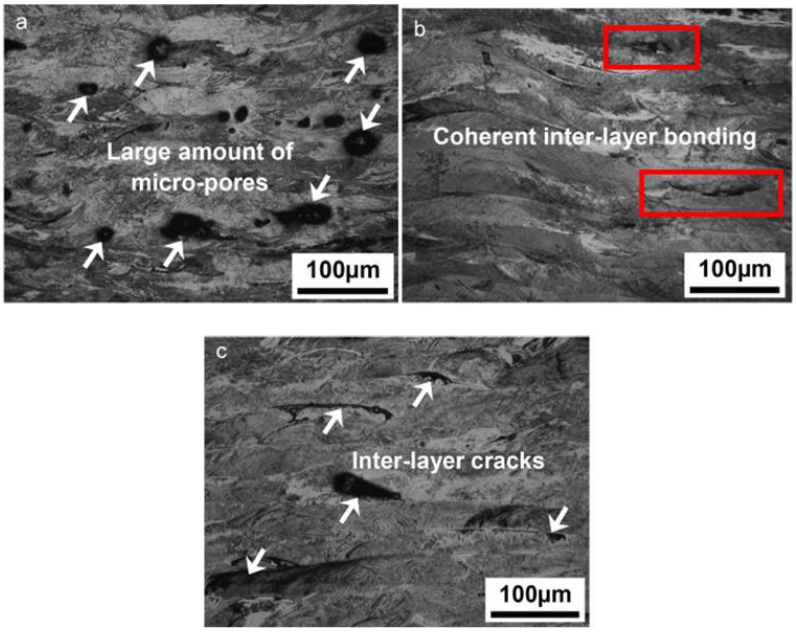

Figure 1-21 Cross-sectional microscopy images of SLM-processed CP Ti samples showing the morphology of the molten pool and the resulting interlayer microstructure for a fixed laser scan speed of 100 mm/s and laser power of (a) 100 W, (b) 150 W, and (c) 200 W [38]

In Kamath et al.'s study of SLM of 316L stainless steel [40], trends of increasing ρ when v decreases or P increases are clearly shown and the maximum ρ value is 99.81%. More recently, ρ value approaching 99.9% was achieved in Sun et al.'s study [41] of the same type of steel when the maximum laser energy within their experimental energy range was used. Similarly, how SLM parameters affect porosity level has been conducted using TiAl6V4 alloy [42, 43], CoCrMo alloy [44], Ni superalloys [45, 46], Mo [47], and Fe-Ni alloy [48]. Imaging based on synchrotron radiation was used in Zhou et al.' study [44] and image analysis of metallography samples was used to determine ρ in all the other cited studies. Clearly, in these studies, LOF is the predominant cause for ρ <1. In the work of Qiu et al. [48], close to zero porosity area fraction is achieved if v is not high. In all the studies cited above, the nature of LOF defect in relation to the track profile has not been studied in detail.

The study of Sun et al. [41] on stainless steel 316L studied the relationship between density and samples built with different building parameters but same energy density as presented in Figure 1-22a. In their micrographs of samples built with different conditions (Figure 1-22b, c &d) LOF and gas pores can be observed clearly. However, in their study LOF formation is not well explained and has only been referred to other studies that have been done on LOF with little analysis on the effect of track geometry on the amount, size distribution and formation of LOF.

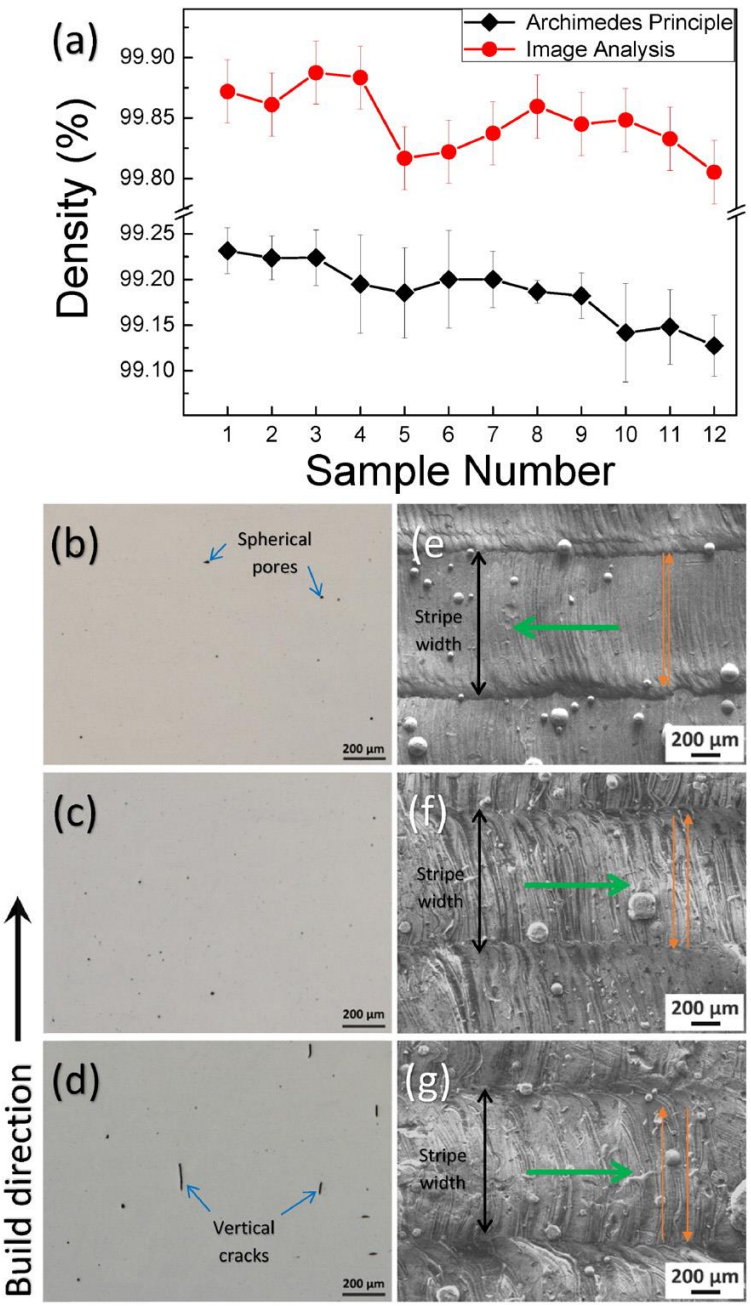

Figure 1-22 a Density graphs obtained using Archimedes and image analysis methods. The OM images of b, c & d showing the pores and LOF. Build direction is indicated for a, b and c. SEM images showing the topography of samples in Sun et al.'s study on stainless steel [41]

In the study by Chong et al. [49] on CoCrMo alloy, melt pool shape and geometry and LOF in the SLM fabricated part were studied using simulation and experimentally. In both techniques the depth and width of the melt pool increased by decreasing the scanning speed and increasing laser power. However, there is a larger discrepancy between simulation and experimental results for melt pool depth than for width. Experimentally,

the results indicate that the point to point variation in depth is possibly very large. Thus, simulation is not a reliable indicator for the melt pool geometry in SLM and needs further studies in future to be able to simulate accurate geometry. The melt pool shape was not changed significantly and had a round melt pool shape in all their samples built with different conditions. Also, samples built with relatively high scanning speed (2500 mm/s) tend to bead up with narrower head which is an effect of melt pool hydrodynamics.

The porosity comparison between simulation results and image analysis of their results is shown in Figure 1-23. There is a good correlation between the experimental and simulation results, and the reason for the porosity in samples is shown to be LOF. The formation of LOF was explained by the track geometry which is agreeable with this present study on track geometry and LOF and will be explained in detail in results and discussion chapter.

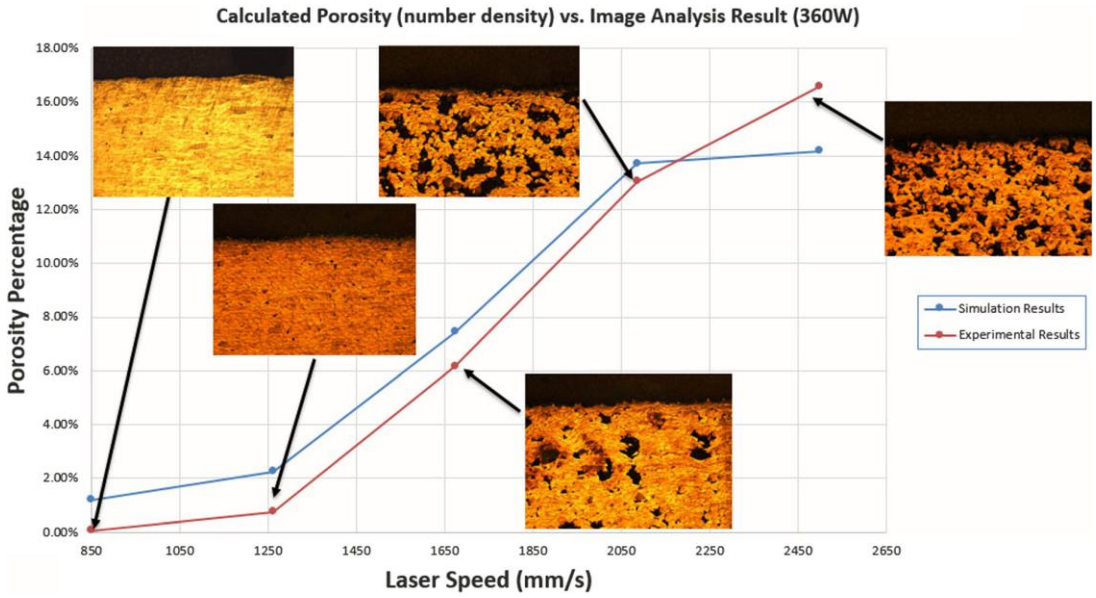

Figure 1-23 Porosity comparison, simulation versus experiment [49]

Similarly, Xia et al. [50] studied the porosity evolution using simulation and experimental methods on Inconel 718 alloy built with different scanning speed. Figure 1-24 shows LOF or ‘inter-layer porosity’, using their words, in their samples. It is clear that the bonding between the interfaced layers is weak at some points and by increasing scanning speed

the LOF becomes bigger in size. The interlayer porosity (LOF) is explained to be generated due to the decrease in the amount of accumulated energy and weakening of velocity of molten liquid flow. Albeit, this is a very recent and useful published paper however, the influence of track geometry on LOF formation is not fully considered and it has primary been linked to the melt flow and dynamic viscosity. Thus, it would be beneficial to relate the LOF formation to both geometry and melt flow of the melt pool.

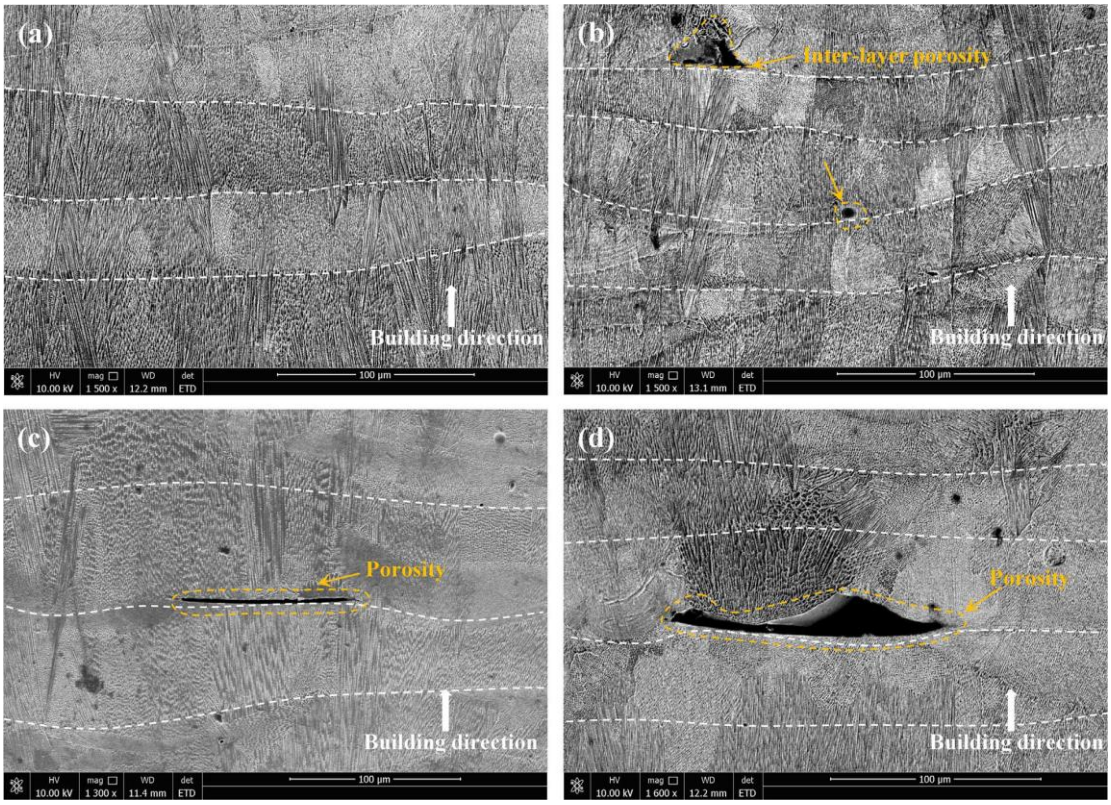

Figure 1-24 Cross-section FE-SEM morphologies of the SLM-processed Inconel 718 superalloy at different scanning speeds: (a) 200 mm/s, (b) 300 mm/s, (c) 400 mm/s, (d) 500 mm/s [50]

The aim of this study is thus to analyze the track profiles of a series of SLM samples made using a range of selected SLM conditions in order to explain geometrically the efficiency of lapping/laying in relation to LOF formation. The study was conducted using CoCrMo alloy. As reviewed by Koutsiukis et al. [14], structures and properties of SLM processed CoCrMo alloy has recently be studied quite intensively, but the referred aspect of how process parameters affect track profile and the amount of LOF has not been conducted.

CoCrMo alloy is a very important alloy for dental and biomedical applications for which, as reviewed by Pinkerton, SLM products are widely viewed suited to.

In their comprehensive study of 316L stainless steel SLM to relate ρ to v and P, Kamath et al.'s [40] conclusion has suggested that a higher laser power may be more influential for obtaining high ρ values. In the extensive work of Zhou et al. [44] on SLM of CoCrMo alloy, the sample made with the condition corresponding to the E_{max}, using a low v value, was stated to be 100% dense. However, all their other 9 samples with lower E values, including one recommended by manufacturer (E = 76 J/mm^3), were less than 99% dense due clearly to LOF. Their study has been restricted to P_{max} = 200 W, which is the limit of their machine. Thus, in the present study of using a more powerful machine, CoCrMo SLM samples were made from 180 W to 360 W while other parameters including the use of a moderate v value were kept unchanged.

1.4 Effect of SLM Spattering on LOF Formation

Spattering is a very common phenomenon in laser manufacturing that occurs due to the instability of melt pool in the process [51, 52]. As will be presented in results of chapter 3, for the first time in SLM studies, we have identified how large spatters cause large LOF in SLM products. Thus, a brief review on spatter, its formation and, the effect of spatter on LOF formation (which has gained significantly more attention after our journal publication) are given here.

During laser processing, the energy density radiated on the powdered metal is approximately 10^6-10^7 W/cm^2, at times when the powder particles melt, they vaporised into plasma to assist the powder bed to absorption of energy from the laser beam. Under the blow off impulse pressure, the melt pool becomes instable and is forced to let some of the liquid molten metal to escape the melt pool at a certain speed which leads to formation of spatters. In current SLM machines, spatters can be mostly prevented by

using a high velocity shielding gas flow in order to prevent powder bed contamination. However, a significant part of the metal spatters can still contaminate the powder bed surface [53].

Only a few research studies discussed spattering in SLM fabricated products. SLM process is involved with many different factors, including rapid melting and solidification of the powder accompanied by complete melt dynamics and heat transfer inside the melt pool. Thus, since spatter is governed by various factors, it is rather difficult to precisely outline the principle of spattering. Liu et al.'s [54] study on 316L stainless steel categorized spattering as liquid or powder based on the principles of spattering which occurs in the SLM process. Their tensile test and microstructure analysis revealed that spattering significantly lowers the quality of SLM parts. Simonelli et al. [55] examined the effect of spattering in SLM on different materials. Their results show that the SLM process is extremely sensitive to the amount of oxygen in the SLM chamber since oxide was observed to be rich at the surface of spatters. Even though spatters were recognised as an influencing factor on mechanical properties however, there was no link between LOF formation and spattering in SLM process before our journal paper on formation of LOF. In our paper, presented in the results section, the effect of spatters fused to the powder bed during the SLM processing on the large LOF formed in the parts are shown and discussed.

In 2017, Gunenthiram et al. [56] studied the effect of laser beam melting process parameters on spatter generation using 316L stainless steel. The evolution of size and number of spatter particles with altering laser parameters were recorded by a camera during the process. The size distribution of the spatters was between 20µm to 200µm in diameter which is much larger than the melted powder. A few droplets have the size of over 200µm. Influence of process conditions on generated spatter particles is shown in Figure 1-25. Increase in laser power globally increases the number of spatters as

illustrated in Figure 1-25a. Also, decrease in the scanning speed led to increase in the number of spatters, excluding the *P* 1520 W and *v* 0.33 m/s condition which showed lower spattering (Figure 1-25b). However, the correlation between spattering and LOF was not studied.

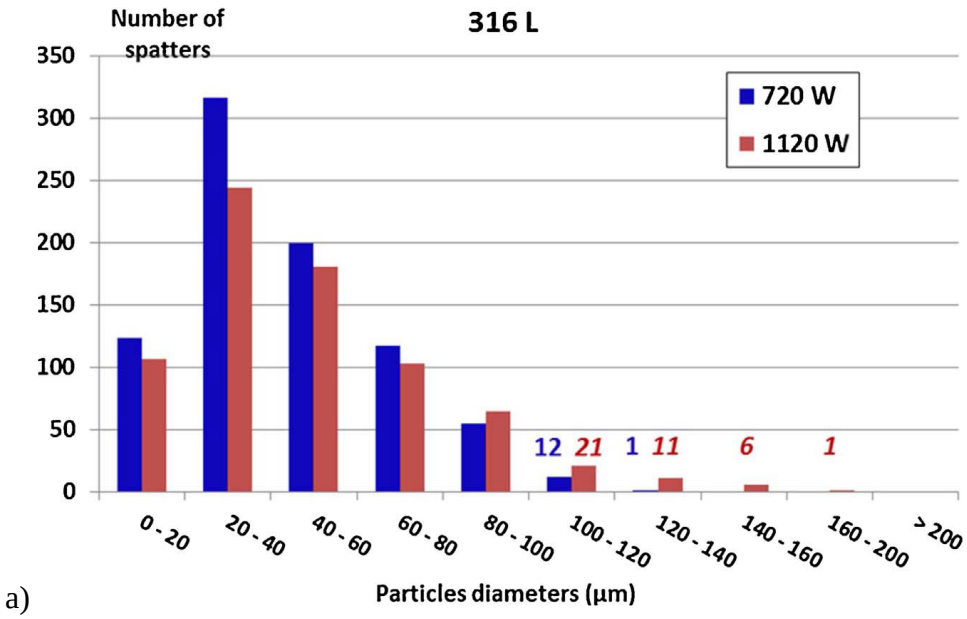

a)

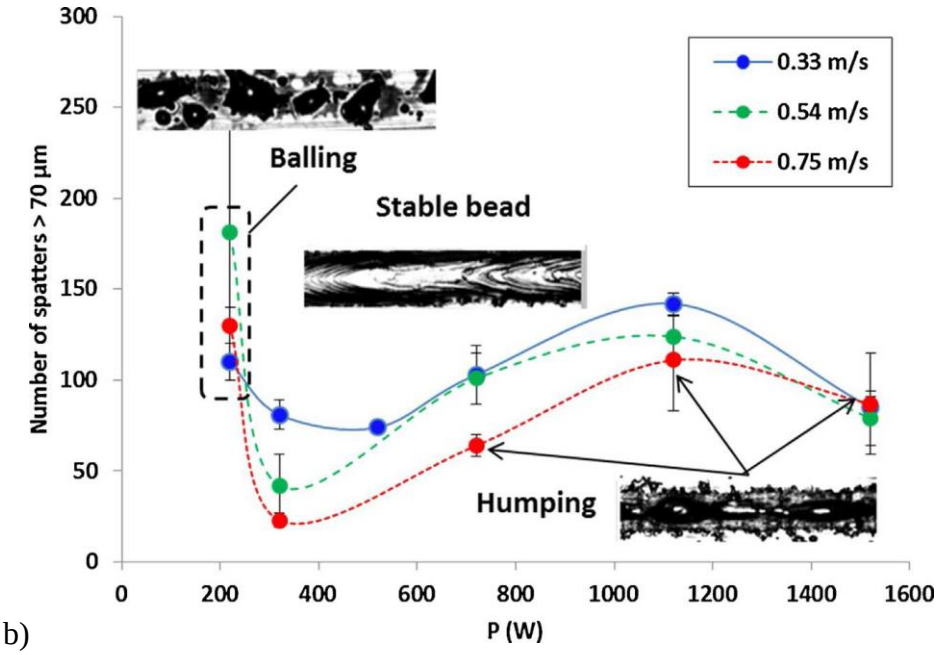

b)

Figure 1-25 Influence of laser power and scanning speed on spatters generation in the study of Gunenthiram et al. on stainless steel [56]

After the publication of our journal paper in the late 2016 on the effect of spatter on LOF formation, Wang et al. [53] followed the idea of LOF's influence on spatter and even used

the schematic illustration of LOF formation that was drawn by us, with a slight modification in their journal paper without citing our journal paper. In their work it was shown that the energy input influences spattering. Low energy input results in weak spattering at the rear of the melt pool. Increasing energy input led to stronger spatter and the number of spatter also increased.

Morphology of spatters was categorised into three different types by Wang et al. [53]. Figure 1-26 shows a schematic drawing of formation mechanism of three different types of spatters. When laser melts the powder bed, loosely stacked particles that are gas-solid two-phase powder particles, high temperature causes some of the liquid metal to violently evaporate. Alongside, the increase of the gas phase of the powder particles will result in formation of recoil pressure. Recoil pressure is a high vapour pressure on the melt pool surface that is caused by the evaporation of the material. Metallic jet (type 1 spatter) is formed as a result of the recoil pressure linked with an extreme increase of the gas phase. Owing to Marangoni effect the liquid metal stretches and decomposes into small droplet of spatter (type 2 spatter). Some molten metal at the front of the optical spot is squeezed by the blast wave of the laser and splashes onto the powder particles at the front-end. Concurrently, type 3 spattering is formed due to the non-melted powder particles spattering at the front of the melt pool.

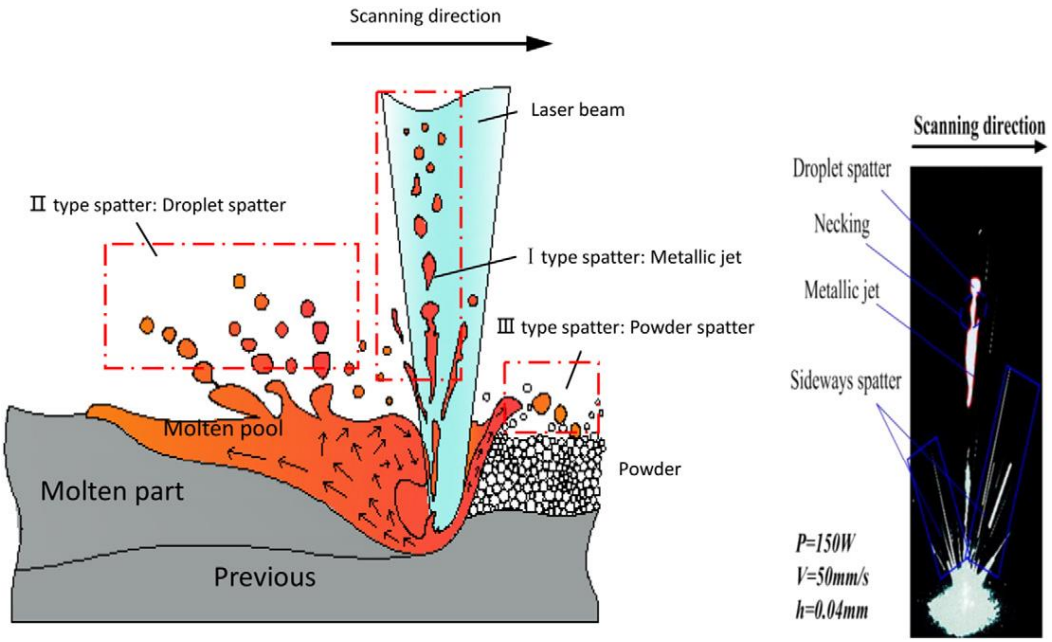

Figure 1-26 Formation mechanisms of spatter a) schematic drawing of three different types of spatters and b) Typical spatter behaviour during SLM [53]

Study of Taheri Andani et al. [51] on splatter formation in SLM using multi-laser technology have similar results to Wang et al.'s [53] research. Their investigation revealed that a higher number of working laser beams induce greater recoil pressure above the melt pools which results in a higher number and bigger sizes of spatters compared to single laser beam. The larger size and quantity of spatters in multi laser beam sample led to lower strength and ductility which is reasonable as shown in Figure 1-27.

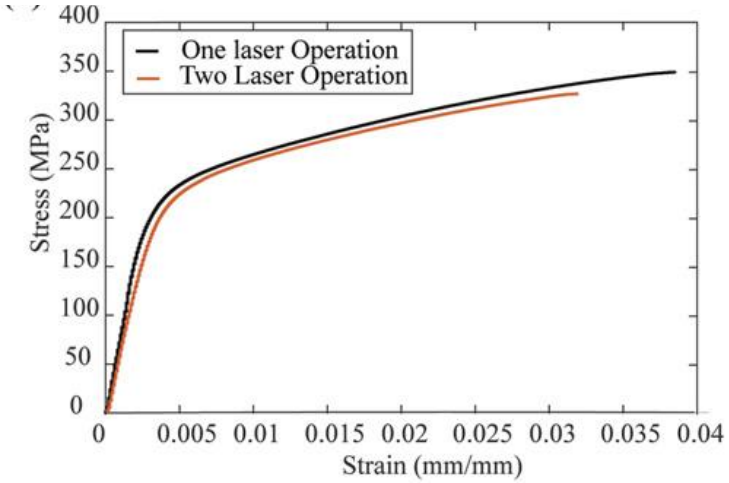

Figure 1-27 Representative engineering stress-strain curve of uniaxial tension samples made by one laser beam and two laser beams. The curves show the differences in strength and elongation values [51]

In summary, spattering was identified in SLM processing, however, there had not been a deep analysis on the effect of spattering on LOF formation and the crucial detrimental impact of it on the quality of products until the publication of our article on the effect of spattering on LOF generation. After our publication, there has been various studies on the correlation between LOF and spattering and the effect of SLM parameters on spattering which have been summarised above.

1.5 Fundamentals of Solidification Relevant to SLM

Similar to laser welding and cladding, melt pool in SLM can be considered as a small casting. Usually a continuous casting is formed under particular criteria that includes melt pool stirring or Marangoni convection, high temperature gradients, rapid solidification, constant close contact at the interface of the molten alloy and the underlying layer which includes partial melting of the layer below. Since SLM uses heat source similar to traditional welding processes, it often has similar structure to those in multipass welding. However, because of the rapid melting and solidification and the layer by layer processing of the powder the structure differs from that of traditional welding [57, 58].

Nucleation and growth are two processes that grain formation in alloys is usually presented with. Nevertheless, it is not uncommon to not observe the nucleation step in weld zone solidification. However, the nucleation by the solid crystals which is situated at the solid-liquid interface (*s/l*) leads to formation of crystals. This form of growth that crystal of one substance grows on the crystal of another substance, in a way that the crystalline substrates of both of the substances have the same structural orientation is known as epitaxial growth. Therefore, each crystal in the molten pool originated from a continuation of one of the grains that lie along the solid-liquid interface.

The primary grain structure continuous to grow in a columnar way as the fusion line progresses through the melt. Figure 1-28 illustrates the epitaxial and columnar grain

growth in a solidified melt pool which demonstrates the relationship between the grains in the underlying layer and the primary weld zone grains that grows from fusion line [57, 59, 60].

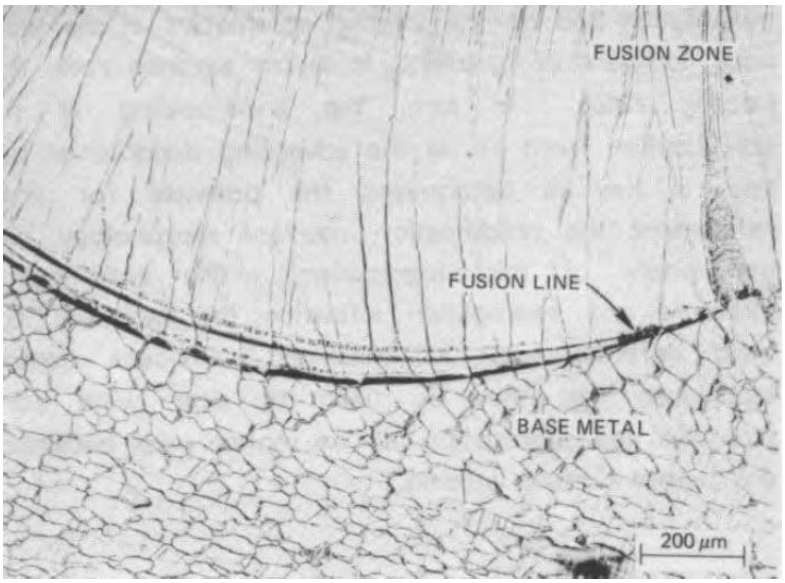

Figure 1-28 Epitaxial and columnar growth near the fusion line in an iridium alloy [57]

The type of obtained microstructure in the melt pool is influenced by the conditions of heat transfer. Solidification at the interface of solid-liquid can progress as either a stable planar front or an unstable front which leads to formation of columnar dendritic or cellular grains. During directional solidification, the mode of solidification and solidification's morphology depends on the degree of constitutional supercooling. Supercooling is obtained by cooling a liquid below its freezing point, without it becoming solid. As Figure 1-29 shows if the liquid is chilled considerably below the equilibrium temperature, it will make the solidification front to become unstable. Therefore, two key parameters that control the final microstructure in a directional solidification are the temperature gradient, *G*, in the direction of solidification and the rate of liquid-solid interface growth, *R*. *G* and *R* values are both linked to the cooling rate that is influenced by heat extraction from the melt pool.

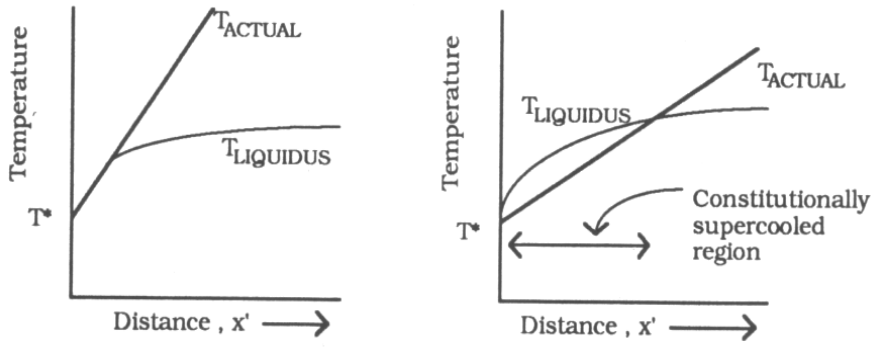

Figure 1-29 Supercooling in alloy solidification (a) stable interface and (b) unstable interface [61]

During solidification the presence of extra concentration of solute as a result of solute rejection to the liquid in the solidification front decreases the melting point of the liquid. At solid-liquid interface, $T = T_s$ and the freezing point of liquid ahead increases to the enrichment of solute. If the actual temperature distribution ahead of the solid-liquid interface is such that the actual temperature is lower than the freezing point (due to solute enrichment), the liquid is locally supercooled. This is called Constitutional Supercooling. This is illustrated in Figure 1-30, where the shaped area illustrates the value of constitutional supercooling as a function of distance from the solid-liquid interface.

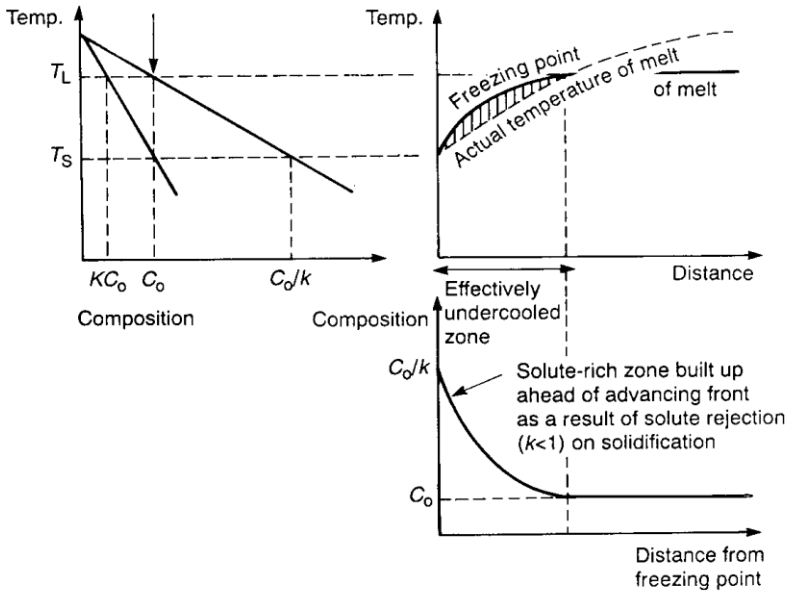

Figure 1-30 The relationship between the constitutional phase diagram for a binary alloy and constitutional undercooling on freezing [61]

We now consider the interface instability and the growth morphology, which are determined by constitutional supercooling (Figure 1-31). Figure 1-31a shows a condition where there is no constitutional supercooling. The liquid next to the interface (x=0) is exactly at the equilibrium liquidus temperature (of *Co/K*) and the temperature of every point in the liquid (*T* in Figure 1-31a) in front of the interface is at a temperature above the liquidus (T_L in Figure 1-31a). If an instability leads to a protuberance to form on the flat interface, the instability will find itself in a superheated situation and will melt back. Hence, the plane growth is stable (Figure 1-31a).

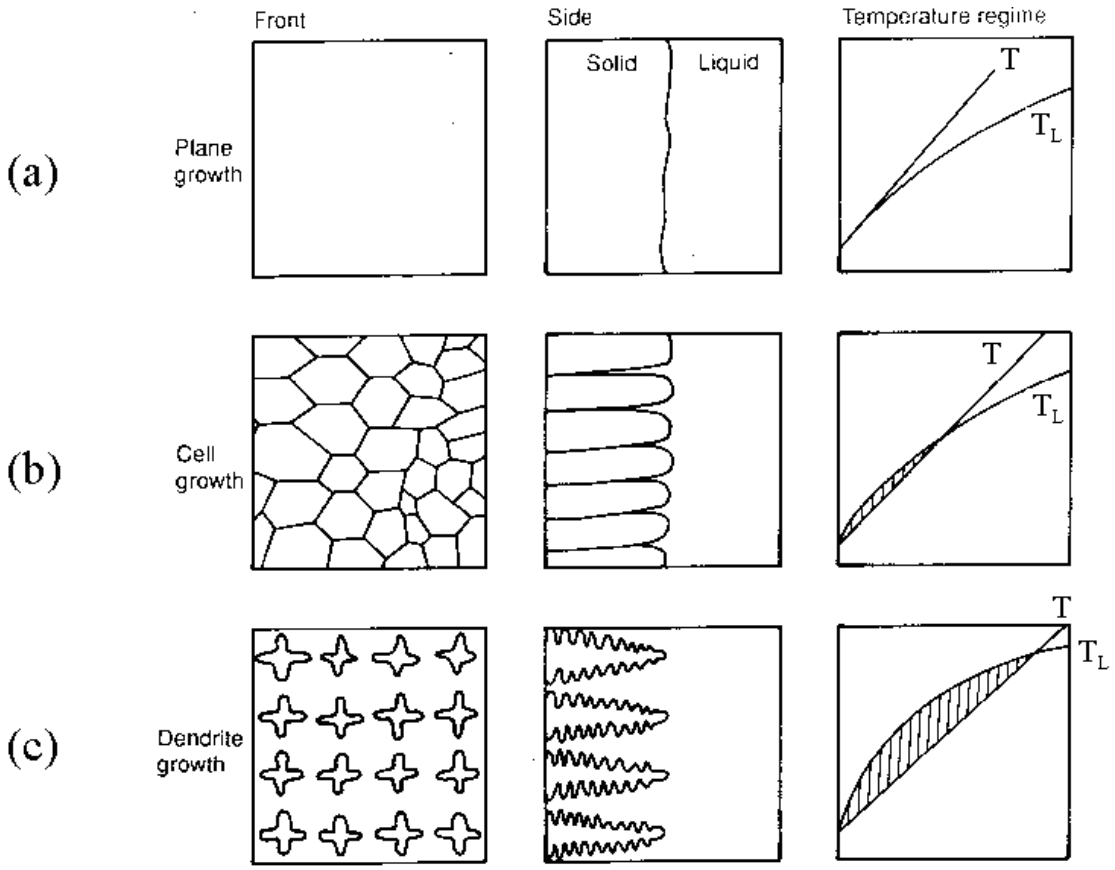

Figure 1-31 The transition of growth morphology from planar, to cellular, to dendritic, as compositionally induced undercooling increases, equivalent to *G/R* being reduced [61]

In contrast, Figure 1-31b is a representative for an unstable case with constitutional supercooling. In this case, liquid immediately in front of the liquid-solid interface is at an actual temperature (*T* in Figure 1-31b) that is below its equilibrium liquidus temperature.

Hence, any protuberance that forms on the interface would happen in the supercooled liquid and because of this it will not vanish. Hence, cellular growth is stable (Figure 1-31b). When the constitutional supercooling increases further, dendritic growth (growth of side branches) will take place (Figure 1-31c).

The requirement of solute conservation at the interface results in the gradient of composition in the liquid at the interface:

$$-D_L \cdot \left(\frac{dC_L}{dx}\right)_{x=0} = R \cdot C_L^*(1-k)$$

Or

$$\left(\frac{dC_L}{dx}\right)_{x=0} = -\frac{R}{D_L} \cdot C_L^*(1-k) \qquad \text{Equation 1-2}$$

The slope of the liquid line m_L in the phase diagram is:

$$m_L = \frac{dT_L}{dC_L}$$

Or

$$\left(\frac{dT_L}{dx}\right)_{x=0} = m_L \left(\frac{dC_L}{dx}\right)_{x=0} \qquad \text{Equation 1-3}$$

As discussed, constitutional supercooling is absent when (Figure 1-31a):

$$G_L = \left(\frac{dT}{dx}\right)_{x=0} \geq \left(\frac{dT_L}{dx}\right)_{x=0} \qquad \text{Equation 1-4}$$

Combining the Equation 1-2, 1-3 and 1-4 gives the general constitutional supercooling criterion; this is, a plane front is stable when:

$$\frac{G_L}{R} \geq -\frac{m_L C_S^*(1-K)}{KD_L} \qquad \text{Equation 1-5}$$

It can be shown that at steady-state, with no convection in liquid, $C_S^* = C_o$ and Equation 1-5 becomes:

$$\frac{G_L}{R} \geq -\frac{m_L C_0 (1-K)}{K D_L} \qquad \text{Equation 1-6}$$

Where *R* is the rate of movement of the (*s/l*) interface (solidification growth rate), D_L is the diffusion coefficient in liquid, *k* is partition ratio, and G_L *(G)* is the thermal gradient across the *s/l* interface. A general statement can be made that *G/R* determine the form of solidification microstructure (planar, cellular, columnar and equiaxed dendritic).

Heat extraction can affect on the energy of the solid and liquid phases in two ways:

1. Owing to the cooling, there is a reduction in the enthalpy of the liquid or solid that can be explained using: $\Delta H = \int c\, dT$ where *c* is the specific heat.

2. Because of the transformation from liquid to solid there is a reduction in enthalpy, which is equivalent to the latent heat of fusion per mole, ΔH_f.

Heat extraction can be obtained by conducting a right means of cooling to the melt to make an external heat flux, q_e. If the metal is isothermal and the specific heats of the liquid and the solid are the same, the obtained cooling rate $^{dT}/_{dt}$, can be deduced from a simple heat balance. Using the latent heat of fusion per unit volume $\Delta hf = {}^{\Delta Hf}/_{v_m}$, and also the specific heat per unit volume, c, in order to follow with the dimensions of other factors, then:

$$q_e \left(\frac{A'}{v}\right) = -c \left(\frac{dT}{dt}\right) + \Delta hf \left(\frac{df_s}{dt}\right) \qquad \text{Equation 1-7}$$

So that:

$$\frac{dT}{dt} = -q_e \left(\frac{A'}{vc}\right) + \left(\frac{df_s}{dt}\right) \cdot \left(\frac{\Delta h_f}{c}\right) \qquad \text{Equation 1-8}$$

The first term on the right-hand side of Equation 1-8 is supposed to show the influence of melt geometry (ratio of surface area, *A'*, to its volume *v*) upon the extraction of sensible heat, whereas the second term takes account of the continuing evolution of latent heat of fusion during solidification. For an alloy which the solidification proceeds over a range of temperatures, the variation of solid as a function of time ($\frac{df_s}{dt}$) must be calculated from the equation:

$$\frac{df_s}{dt} = \left(\frac{dT}{dt}\right)\left(\frac{df_s}{dT}\right) \qquad \text{Equation 1-9}$$

Since f_s is a function of temperature, the cooling rates turn into:

$$\frac{dT}{dt} = \frac{-q_e\left(\frac{A'}{vc}\right)}{1-\left(\frac{\Delta hf}{c}\right)\cdot\left(\frac{df_S}{dT}\right)} \qquad \text{Equation 1-10}$$

It can be understood from the derived Equation that solidification reduces the cooling rate because $\frac{df_s}{dT}$ is negative. With a moving heat source and directional solidification, the cooling rate can be calculated at a given location and time by:

$$\left(\frac{dT}{dt}\right) = \left(\frac{dT}{dx} \times \frac{dx}{dt}\right) = G \cdot R \qquad \text{Equation 1-11}$$

As has been explained, the solidification mode is governed by the ratio *G/R* while the $G \cdot R$ determines the scale of the solidification microstructure. Figure 1-32 shows the effect of G/R and $G \cdot R$ on the solidification microstructure. Depending on the *G/R* value the solidification microstructure can be planar, cellular, columnar dendritic or equiaxed dendritic. The dimension of the microstructure decreases with increasing the $G \cdot R$ value. Hence, in laser welding that has a high solidification rates (>10^4 K/s), the microstructure inclines to become more dendritic as the ratio *G/R* value reduces, although the dendrite spacing has a tendency to increase as supercooling (stated as $1/\sqrt{GR}$) gets higher. Therefore, increase in $G \cdot R$ value will result in a finer microstructure. Ultimately, when

the supercooling increases (high $1/\sqrt{GR}$) the dendrites nucleate at a point and the equiaxed structure is formed [57-60, 62].

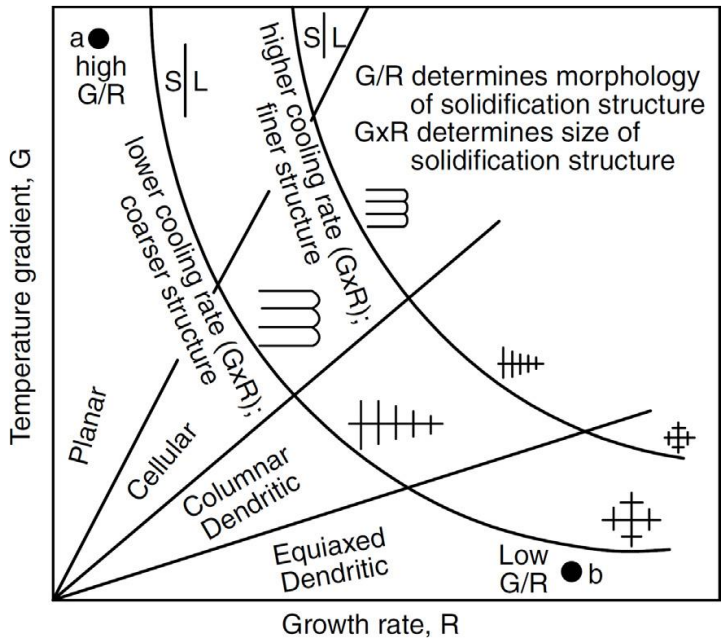

Figure 1-32 Effect of temperature gradient *G* and growth rate *R* on the morphology and size of solidification microstructure [62]

Solidification maps for alloys can be used to determine what structures will form during sonification of melt pool. Despite the complexities of SLM process, the solidification microstructure, like laser welding, is primarily governed by a few key parameters which are the temperature gradient and solidification rate. Efforts to link the processing parameters with these main solidification parameters can efficiently help with the understanding of the relationship between process and structure. Thus, as a part of my PhD study, the microstructure development in SLM using CoCrMo alloy will be studied.

1.6 Modes of Solidification and Direction of Grain Growth

With the strong activities of research and industrial applications of metal AM, Co–Cr alloys processed by SLM have been evaluated by various researchers in recent times. Research on SLM of Co–Cr dental alloys up to late 2013 was reviewed by Koutsiukis et al. [14]. Although the focus of the review was on dental applications of AM, manufacturing defects and mechanical properties were sufficiently discussed. Clearly, the

early work reviewed by Koutsiukis et al. has shown SLM to be a promising manufacturing technique for Co–Cr dental restoration alloys. However, due to the then insufficient study on solidification of Co–Cr alloys during SLM, there is little discussion on solidification and solidification microstructures in the referred review.

Figure 1-33 shows the microstructures of the SLM fabricated CoCrMo samples in Takaichi's [22] experiment. The optical microscopy image (Figure 1-33a) taken from the x-z plane shows circular arch-shaped boundaries and various fine particles. Further SEM observation (Figure 1-33d) on this plane showed cells with a diameter of approximately 2.7 µm. Melt pool boundaries on the x-z plane are shown in Figure 1-33b of transverse cross section parallel to the SLM building direction.

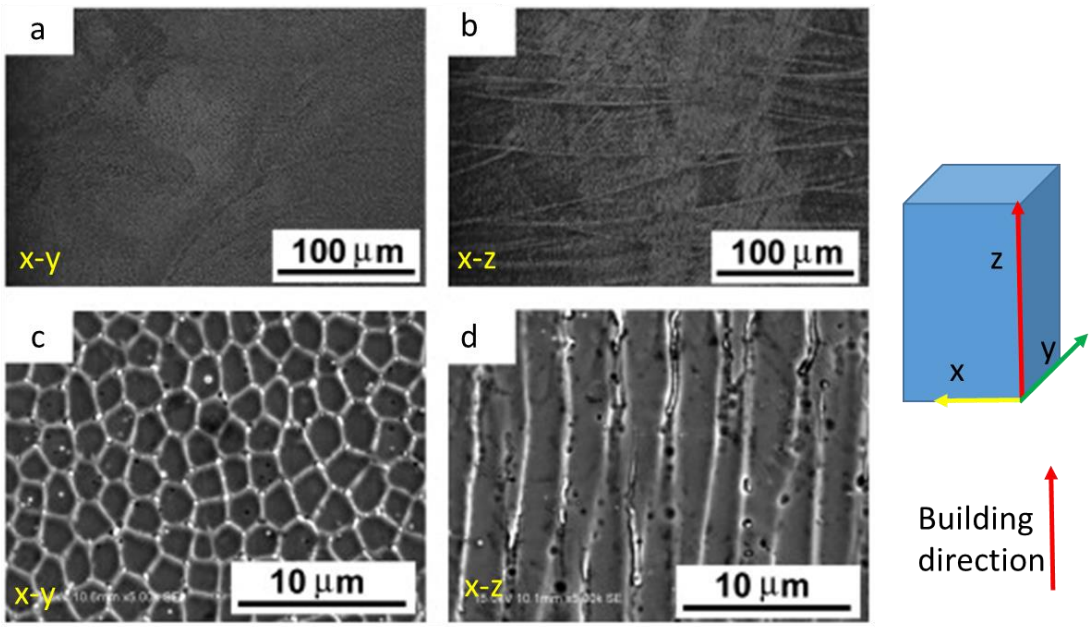

Figure 1-33 Microstructure of the SLM builds: (a) OM image taken from x-y plane; (b) OM image taken from the x-z plane. SE image of (c) and (d) are magnified views of (a) and (b) [22]

EBSD orientation map in Figure 1-34 showed epitaxial and columnar grain growth along the build direction. However, it is also clear in their SEM image that a large portion of cellular growth directions are very different to the build direction. Columnar grains with a cellular structure of submicron spacing within each grain and the cellular growth

direction may or may not be along the build direction. However, epitaxial growth in melt boundaries has not been discussed sufficiently in this study.

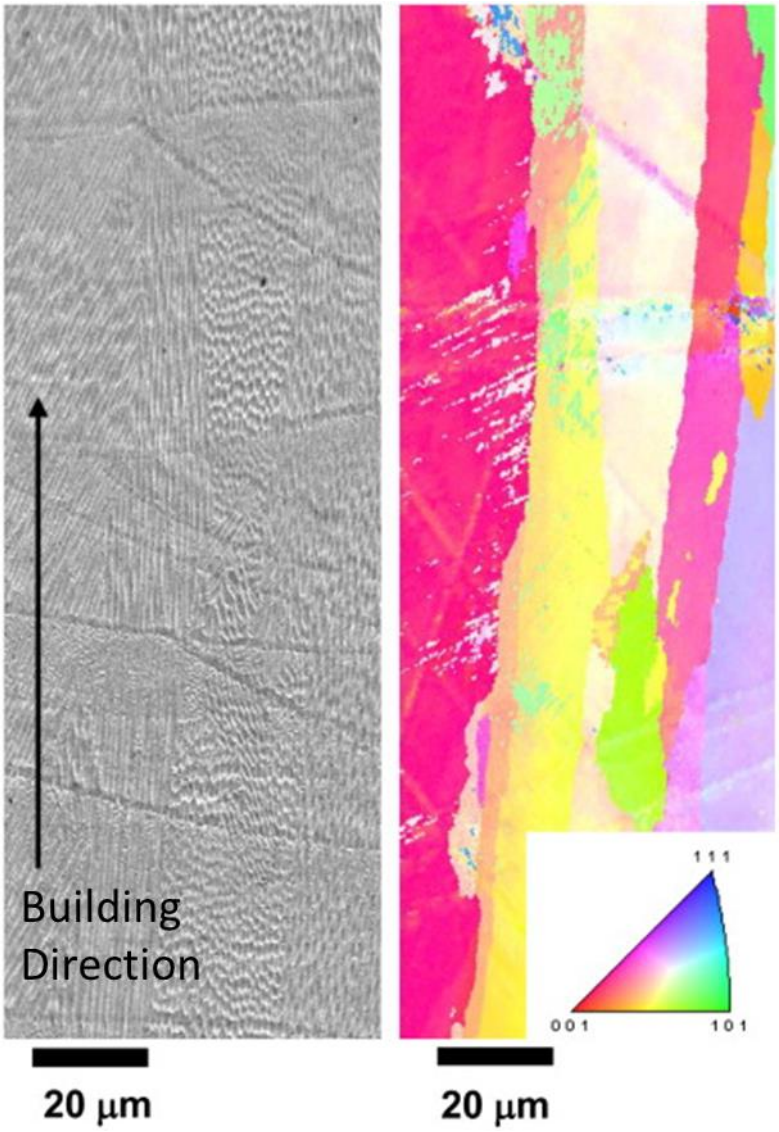

Figure 1-34 BSE image of the SLM build and corresponding crystal orientation map. The arrow indicates the building direction and the analysed direction by EBSD in Takaichi et al.'s work on Co-Cr-Mo [22]

Epitaxial growth and that grains consisting of multiple cells can grow over many layers during SLM of metals are generally recognized [63, 64]. However, in the comprehensive review by Collins et al. [32], they suggest that new nucleation instead of epitaxial growth could be possible when thermal gradients alternate between layers. For epitaxial growth, crystal growth direction altering abruptly at melt boundaries to more closely align with

heat flux direction has recently been recognized during SLM of IN738LC Ni [65] alloy and 316L stainless steel [66]. This change in grain growth direction in track boundaries is not consistent with the commonly observed grain growth along the build direction crossing many layers.

Furthermore, in Wang's study [66], change in growth direction as illustrated in Figure 1-35b in the upper region of a melt pool affected by heat flux was also suggested. However, this suggestion needs structure analysis (by EBSD) to verify. More recently, Popovich et al. [67] showed that grains are primarily of ''chaotic'' orientation identified using EBSD in SLM Inconel 718 Ni alloy samples built using normal SLM parameters. Columnar grain growth across many layers is the dominant mode only when a very high (and uncommon) laser power is used.

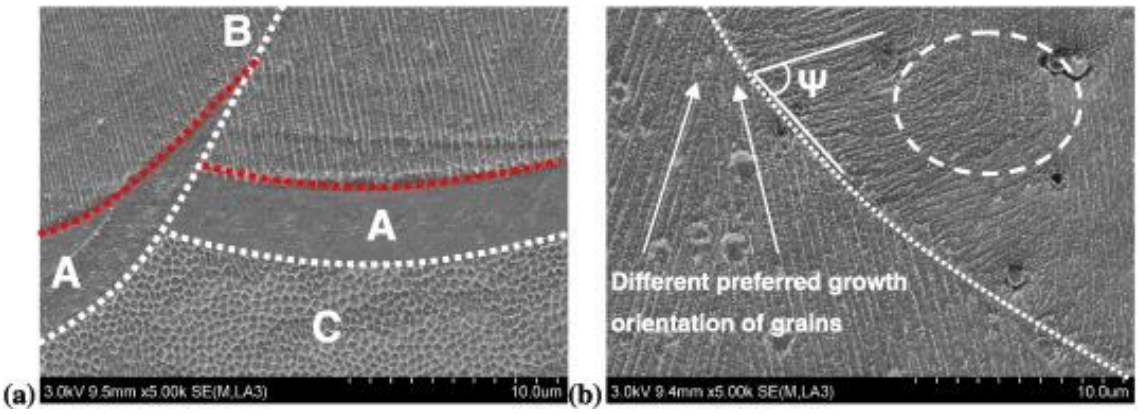

Figure 1-35 FE-SEM images showing characteristic microstructures of SLMed Inconel 718 Ni alloy parts (ω = 125.00 J/mm3) locating in (a) "layer-layer" melt pool boundary showing cellular dendrite in zones B & C and claimed planar zone in zone A (b) "track-track" melt pool boundary [66]

Also in Wang et al.'s study of SLM 316L stainless steel [66], featureless regions of uniform and non-uniform thickness up to a few microns in a SEM micrograph have been suggested to be planar growth. However, in the same study, cells having grown in melt boundary directly from cells of previous track are also clearly shown, meaning nonplanar growth. During fusion welding of metallic alloys, planar growth adjacent to melt

boundaries is commonly observed [68]. This is due to the ratio of temperature gradient over growth rate along the melt boundary being very high. The planar growth layer is normally quite uniform before transiting to cellular/dendritic growth.

In an extensive review together with experimental work on key factors affecting the solidification of fusion welds continuum from weld interface (fusion line) to centreline, Rajamaki [69] suggested that the planar zone is not always observed and also concluded that a slow welding speed favours planar growth. As scan speed during SLM is normally high, the absence of planar growth clearly shown in micrographs from recent SLM studies of 316L stainless steel [70], 18-Ni 300 Maraging steel [71], high-Si steel [72] and Ni superalloy [65, 73, 74] is consistent with Rajamaki's conclusion.

Differing from SLM of other alloys, during SLM of Ti–6Al–4 V alloy, there is a major phase transformation. The solidified β (bcc) phase transforms to acicular martensite (hcp structure). Due to the transformation, the original track boundaries may not be revealed in micrographs. In the early study on SLM of Ti–6Al–4 V, Thijs et al. [8] showed clearly the transformed microstructures in their micrographs demonstrated in Figure 1-36, although tracks were distinguishable with the appearance of darker bands indicating track boundaries. Clearly, no planar growth layer could be identified in their micrographs. However, Kruth et al. suggested solidification with a stable planar front during SLM of Ti–6Al–4 V [63], citing Thijs et al's study [8].

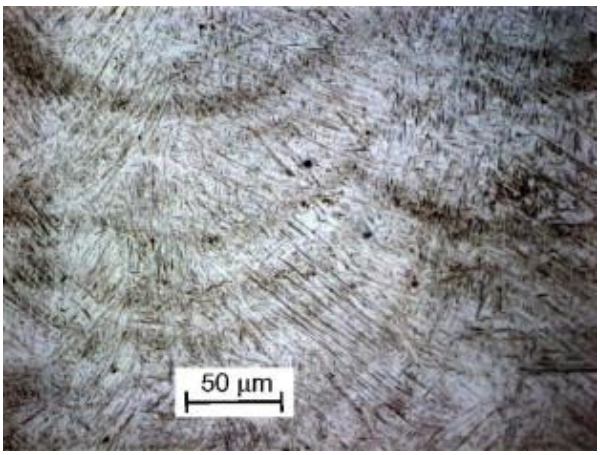

Figure 1-36 Micrograph of cross section of Ti64 sample [8]

In the recent study on SLM HY100 steel [75], dark bands are also present due to locally different thermal histories and different tempering. No evidence has suggested the mode of solidification. Micrographs of later studies of SLM Ti–6Al–4 V by Thijs and Kruth et al. [76-79] clearly show transformed microstructure without the original cells or dendrites, although the solidification mode is again stated as planar [77]. In Yadroitsev et al.'s study of Ti–6Al–4V SLM [80] using different scanning strategies, track boundaries are identifiable and shown in Figure 1-37, and the transformed microstructure is of also acicular martensite. Again, there is no evidence to suggest a planar growth layer.

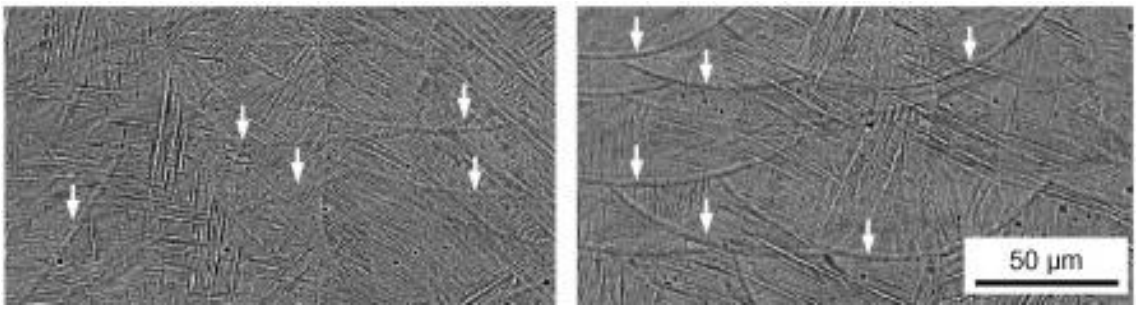

Figure 1-37 SEM images of the microstructures of Ti–6Al–4V specimens built with different scanning strategies, white arrows indicate melt pool boundaries [80]

With regard to grains grown inside the tracks, in the recent study by Cloots et al. [81] on a gas turbine CoCr-based alloy (Mar-M509), fine grain bands ≈100 µm in width and thicker (>200 µm) bands of coarser and more elongated grains alternating are shown in

orientation maps (Figure 1-38). They suggest that this is due to recrystallization, not solidification, having occurred due to SLM thermal cycling. However, how thermal cycling during SLM with 30–35 μm layer increment relates to the much thicker bands of alternating grain morphology may need further study.

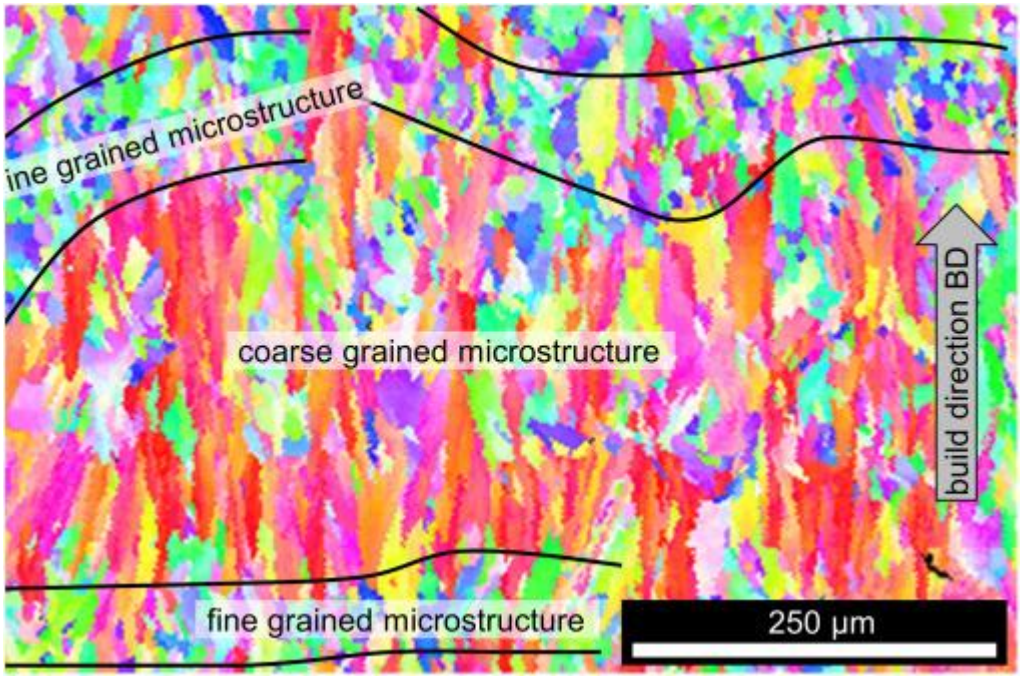

Figure 1-38 Regions of fine and coarse grains in the Mar-M509 microstructure leads to formation of sandwich structure [81]

Local equiaxed solidification during SLM of a Co–Cr–Mo alloy using a zigzag scanning strategy has been stated by Zhou et al [82]. They suggest that the narrow bands of less elongated grains viewed from top to be the result of central line equiaxed solidification. It should be noted that grinding of samples for metallography means grounding off the top and central region of tracks, which should be the final solidification region in a track cross section. Figure 1-39 shows their side view cross section of a whole track, equiaxed grains are not observed. A further note is that, in both studies (Cloots et al.'s and Zhou et al.'s), orientation maps without high-magnification micrographs cannot reveal clearly the details of epitaxial growth and cellular (or columnar dendritic) structure.

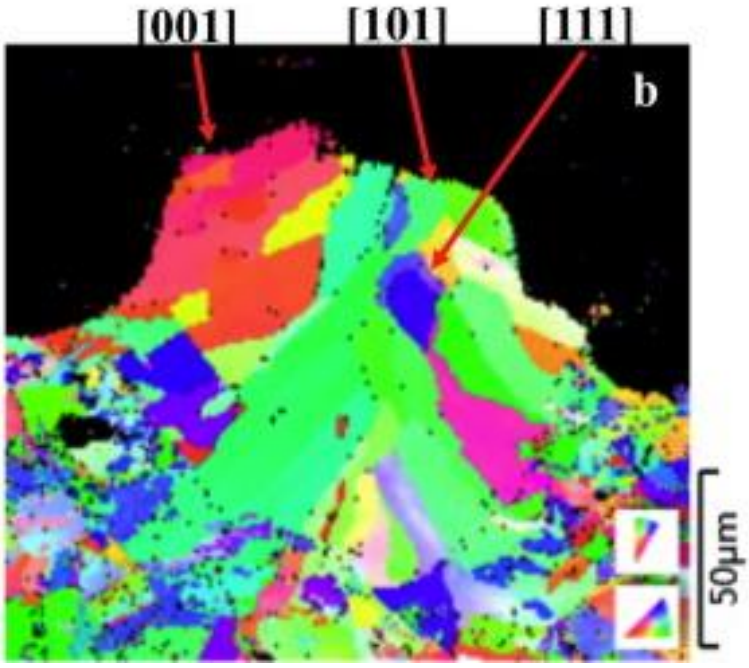

Figure 1-39 Cross section EBSD data of a single laser track using Co-Cr-Mo alloy [82]

Clearly, SLM allows parts with highly complex shapes to be made and thus allows part design with a high degree of freedom. However, as emphasized by researches [32] in their comprehensive review on microstructural control of MAM materials, microstructures which depend on composition and processing conditions govern the properties and performance of the materials. Furthermore, as explained by Zhang et al. [83], topology optimization for SLM parts during design needs to take anisotropy into consideration. But how *P* affects growth direction is still not clear.

Also, the literature review above has suggested that solidification modes and microstructure formation during SLM of metallic alloys and of Co–Cr alloys in particular have not been sufficiently revealed and studied. The understanding of microstructure development during AM including SLM is clearly important, as expressed in the recent review by Collins et al. [32]. As is also clear in this review, thermal fields and gradients together with solid–liquid interface velocities in the small regions of solidification are highly complex. Thus, currently, predicting microstructure formation is very difficult. Clearly, the understanding of microstructures formed is required for SLM Co–Cr to be

applied more widely in biomedical fields, as corrosion and mechanical properties should relate closely to the microstructures of the SLM processed alloys.

1.7 Effect of SLM Parameters on Modes of Solidification

In this section a brief review on the effect of SLM parameters on modes of solidification is given. The effect of layer thickness on the solidification mode of Ti-6Al-4V was studies by Panwisawas et al. [84]using modelling and experimental investigation. SEM of cross-sections of two samples built with 20 µm and 100 µm layer thickness and their corresponding modelling results are presented in Figure 1-40. It is claimed that the bottom region of the tracks has a random and equiaxed grains from the modelling, but the experimental SEM shows a more epitaxial growth. Although SEM image of track built with a different condition is shown, however, there is no discussion on the effect of SLM condition on mode of solidification.

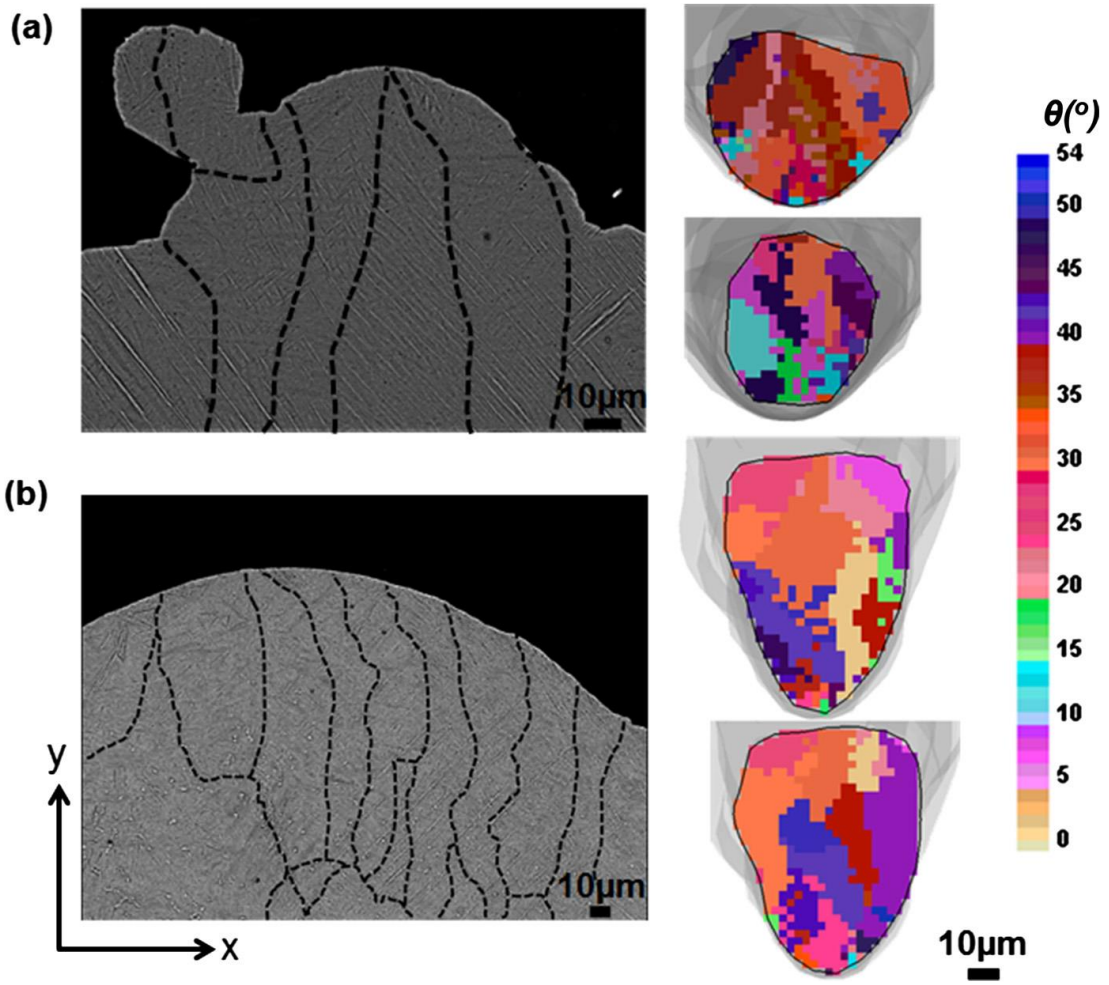

Figure 1-40 SEM micrographs from Ti-6Al-4V observation show the grain morphology (left) and misorientation mapping within the single track (right) of: (a) 20 μm powder layer thickness and (b) 100 μm powder layer thickness [84]

A number of studies have investigated the effect on SLM parameters on the microstructure using experimental or modelling methods. Ivekovića et al. [85] examined the effect of energy density on microstructure of Tungsten and Tungsten alloys. In their study, they argued the presence of equiaxed solidification mode in the centre of the track, however, the effect of energy density on solidification mode was not studied. Zinoviev et al [86] and Lopez-Botello et al. [87] investigated the effect of SLM parameters on microstructure. But both studies are only limited to modelling without any experimental investigation. Also, there is no in-depth analysis on how laser parameters change the solidification mode in SLM process. Similar results are also observed in Yadroitsev et al.'s study on the microstructure of 316L stainless steel [88]. Mode of solidification

investigation is limited to introduction of thermal gradient and solidification rate and how these two can influence the microstructure.

Also, considering the current literature, the influence of SLM parameters on the solidification mode of SLM products has only been briefly studied. Thus, as a part of this study, the effect of laser power as a SLM parameter on solidification mode will be investigated to show if there is a significant change in the solidification and how it is affected by the laser power.

1.8 Effect of SLM Parameters on Size of Solidification Microstructure

A distinctive feature of solidification during SLM is cellular growth in many alloys and cellular-dendritic growth in some alloys. Growth texture and cell size (λ_1) and how they are affected by SLM parameters and can possibly be controlled are thus fundamental to be understood. The theoretical base regarding the solidification mode relevant to laser surface treatment and welding has been explained by Kurz and Trivedi [59].

The values of λ_1 measured in various studies of SLM for which P, v, h and s values are provided are listed in Table 1-2. Figure 1-41. shows an example of measured λ_1 in austenitic stainless steel 316L fabricated by SLM [70]. Micrographs from the cited references show that solidification microstructure is largely in cellular form for stainless steel, Co-29Cr-6Mo alloy and AlSi10Mg alloy. For Ni-superalloys, SLM microstructures can be either cellular or cellular-dendritic.

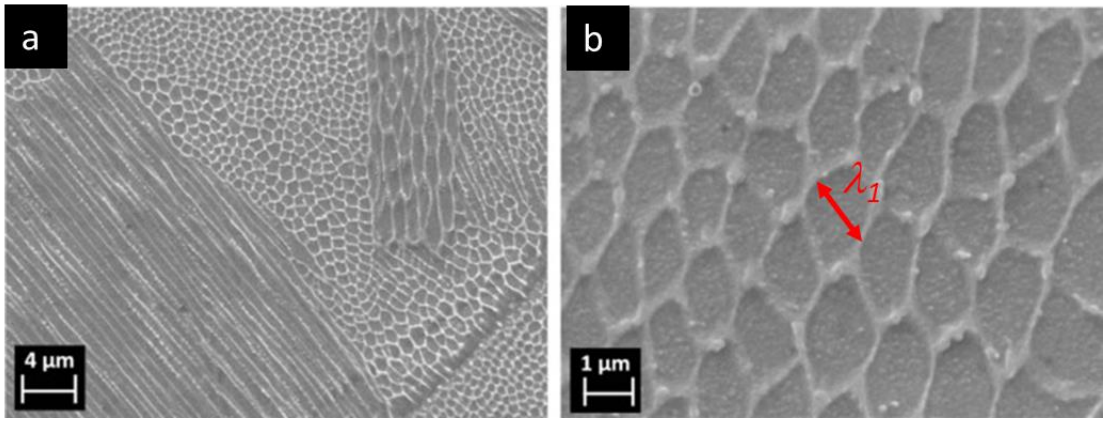

Figure 1-41 SEM micrographs of AISI 316L built parts fabricated by SLM [70]

Table 1-2 Intercellular or primary arm spacing values measured or stated in various published work of SLM and values of SLM parameters used in each study.

Material	**P (W)**	***v* (mm/s)**	***h* (mm)**	***w* (mm)**	***E* (J/mm^3)**	**λ_1, µm**	**Ref., year**
Inconel 625 Ni alloy	160	500	0.02	0.06	267	0.2-1	Li et al. [89]
Inconel 625 Ni alloy	179 - 195	725 - 875	0.02	0.09-0.11	194 - 88	0.4–0.8	Arisoy et al. [90]
Inconel 625 Ni alloy	195	800	0.02	0.1	122	1	Keller et al. [91]
Inconel 718 Ni alloy	90	320	0.025	0.08	56	0.5–1	Choi et al. [92]
Inconel 718 Ni alloy	285	960	0.04	0.116	64	1–1.8	Lee & Zhang [93]
Inconel 718 Ni alloy	950	800	0.1	0.5	59	2–3	Popovich et al. [67]
CM247LC Ni alloy	150	1500	0.015	0.02	33	0.7	Wang et al. [94]
316L stainless steel	300	700 - 1200	0.03	0.08	178 - 104	0.7–0.3	Wang et al. [66]

316L stainless steel	380	625 - 3000	0.05	0.025 – 0.12	100	0.5–1.5	Sun et al. [41]
316L stainless steel	200	750	0.05	0.11	49	1	Casati et al. [70]
Co-29Cr-6Mo	200	50	0.05	0.1	800	2.7	Takaichi et al. [22]
Co-29Cr-6Mo	195	535 & 800	0.05 & 0.02	0.14 & 0.1	65 - 180	1	Hedberg et al. [95]
Co-29Cr-6Mo	90-126	700 - 1200	0.05 – 0.07	0.02	54 - 180	0.5–1	Liverani et al. [96]
V-6Cr-6Ti	190	700	0.04	0.1	69	0.8	Jialin [97]
AlSi10Mg	200	1400	0.035	0.105	39	0.4–0.7	Thijs et al. [98]
AlSi10Mg	370	1300	0.03	0.19	50	0.2-0.7	Tang et al. [99]

As shown in Table 1-2, values of λ_1 range from 0.2 μm to 3 μm, differing slightly over an order of magnitude. A closer examination of data in Table 1-2 shows that the high λ_1 values (2-3 μm) are from two sources, one from Popovich et al. [67] who used a very high P value at 950 W and the other from Takaichi et al. [22] who used a very low v value at 50 mm/s.

Study on Ni-based superalloy SLM has been intensive. In Arisoy et al.'s [90] series of Inconel 625 SLM experiments, they determine how λ_1 is affected by scan strategy and process parameters. It should be noted, as listed in Table 1-2, the range of values for each individual parameter is quite small in their study. For example, Δv = (875-725) mm/s = 150 mm/s, which is small. They conclude that as E increases (from 88 J/mm^3 to 194

J/mm^3) λ_1 reduces. However, the reduction in the average λ_1 is very small and is about 0.1-0.15 μm over the *E* range. This reduction may not be seen statistically significant, as their λ_1 range of 0.4-0.8 (0.39-0.76) μm listed in Table 1-2 largely reflects the scattering of the data in their λ_1 - *E* plot. Observing the data from Li et al. [89] and Keller et al. [91] may suggest a possible trend of a reduction in λ_1 when *E* increases. However, *E* values of Choi et al. [92], of Popovich et al. [67] and of Lee and Zhang [93] for SLM of Inconel 718 are close but λ_1 values differ significantly. As has been pointed out, the high λ_1 (2-3 μm) in Popovich et al.'s study is from the use of very high *P* at 950 W. In their study, they also used *P* = 250 W, but to keep *E* the same (59.5 J/mm^3), *v* (700 mm/s), *h* (0.05 mm) and *s* (0.12 mm) were changed. Although they have not measured, their micrograph of the 250 W zone clearly shows a significantly finer cell structure and λ_1 can be estimated to be ~ 1 μm. This suggests that λ_1 does not relate well to *E*.

For 316L stainless steel, as listed in Table 1-2, Wang et al. [66] demonstrated (Figure 1-42) that λ_1 increased from 0.3 μm to 0.7 μm when *v* reduced from 1200 mm/s to 700 mm/s while keeping *P, h* and *s* unchanged. The reduction of *v* corresponds to *E* having reduced from 178 to 104 J/mm^3. In Sun et al.'s study [41], *v* and *s* were adjusted to result in *E* at ~ 100 J/mm^3, close to the lowest *E* in Wang et al's study. However, Sun et al.'s λ_1 values are generally higher than those of Wang et al.'s. In Casati et al.'s study [70], in comparison to Wang et al.'s study, *E* is considerably lower but λ_1 is higher. Thus, for 316L stainless steel, λ_1 may not simply relate to *E*.

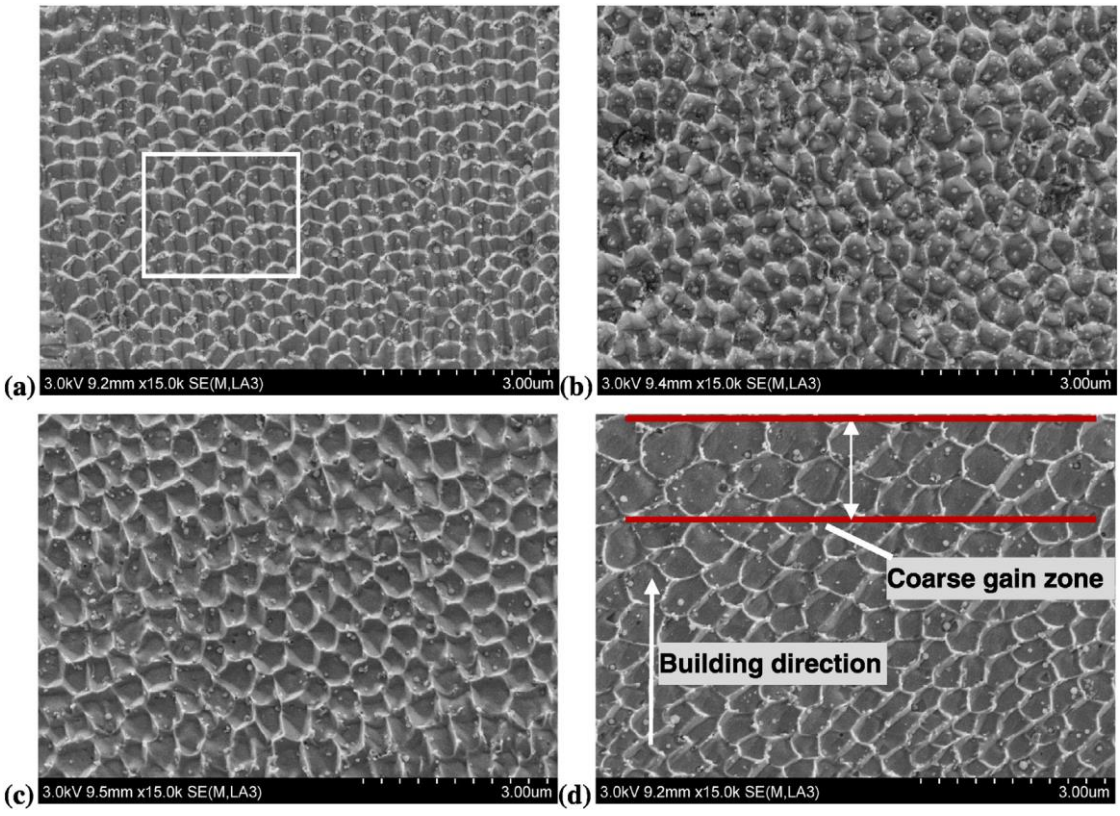

Figure 1-42 High-magnification FE-SEM micrographs showing the cellular dendrites of SLM processed parts at different parameters: (a) 104.17 J/mm3, 1200 mm/s; (b) 125.00 J/mm3, 1000 mm/s; (c) 156.25 J/mm3, 800 mm/s; (d) 178.57 J/mm3, 700 mm/s. [66]

For Co-29Cr-6Mo alloy, as has also been pointed out, the use of a very low v and thus very high E (=800 J/mm^3) by Takaichi et al. [22] results in high λ_1 (=2.7 μm). Although they have not measured, their micrograph of a sample made using E at 200 J/mm^3 by the use of a high v value suggests $\lambda_1 \approx 1$ μm. Other studies on high temperature alloys (Co alloys and a V alloy), as listed in Table 1-2, have shown λ_1 to be 0.5-1 μm for E values in low to medium levels. For SLM of AlSi10Mg, as suggested by the two sources cited in Table 1-2, λ_1 can vary significantly within a study that only a single E value is used.

In summary, there is not a certainty that λ_1 relates to E well. Considering an individual parameter, λ_1 has been demonstrated to inversely relate to v. However, the effect of P on λ_1 has not been systematically studied. P is an important SLM parameter and how P affects the size of microstructure during SLM needs to be understood. Thus, in this PhD

study, microstructure of the SLM samples built with a range of laser powers while layer thickness, hatching space and scanning speed were kept unchanged were examined to allow the effects of P on λ_1 to be understood.

As mentioned in many studies mechanical properties of an alloy are dependent on the microstructure. Controlling the cooling rate during the solidification process is a useful method to change the microstructure in manufacturing processes [100]. In SLM, laser power and scanning speed are the primary factors to control the microstructure. Changing these parameters results in change in thermal condition of the melt pools including size and shape the melt pool, and consequently the size of the grains in SLM [65]. Several studies have been conducted to illuminate the understanding of the thermal condition and cell size in the SLM process.

It has been proposed by Li & Gu [38], but not directly experimented that temperature gradient increases from 1.53×10^4 to 9.84×10^4 °C/mm when the laser power increases from 100 to 200 W in SLM processing of pure titanium. In their study a transient 3D finite element model based on solutions of heat transfer equations was established to predict the thermal behaviour of titanium powder bed during SLM. However, the simulated thermal gradient is for the whole cycle of solidification of one track and does not define the thermal gradient of cells in one melt pool.

Yin & Felicelli [101] using finite element modelling suggested that when laser speed increases from 2 to 20 mm/s, the dwell time of the heat source at each point of the track decreases, consequently cooling rate increases from 1050 to 9000 K/s with constant pool size. They also correlated cooling rate and cell morphology using simulation as shown in Figure 1-43 that by increasing speed the dendrite arm spacing decreases. However, there is no experimental observation from the microstructure to prove the correlation between the cooling rate and arm spacing. Also, in their simulation the melt pool size is kept

constant without considering the effect of geometry of track boundary on solidification and intercellular spacing. Thus this simulation is not a verified empirical method for predicting thermal condition in SLM.

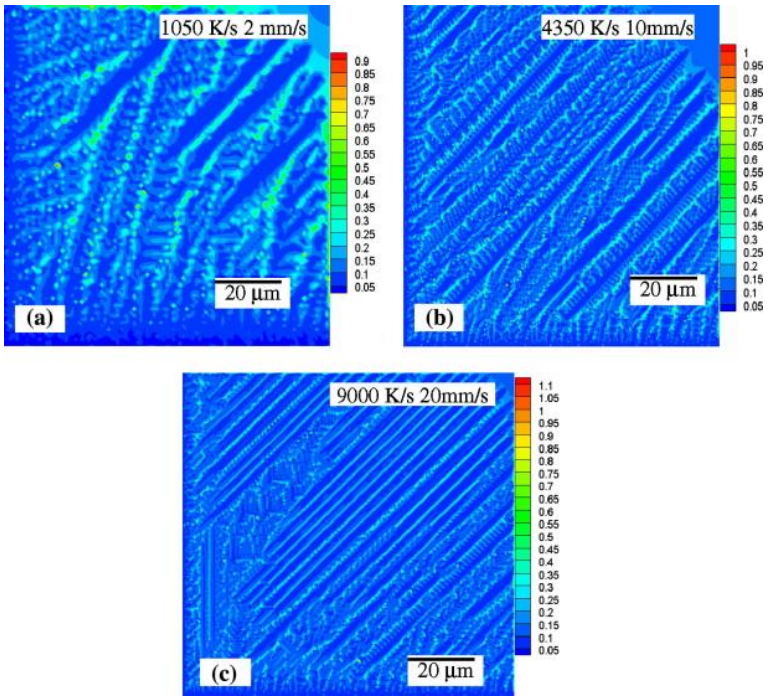

Figure 1-43 Solidification microstructure when laser moving speed is (a) 2 mm/s, (b) 10 mm/s and (c) 20 mm/s. Cooling rate (K/s) is also shown. Colour bar denotes solute concentration of C (wt.%). [101]

Since temperature gradient and cooling rate have not been verified in SLM using real data, in this study we attempt to link cooling rate and cell size using theoretical explanation. Kurz and Fisher [61] theoretically explain that primary spacing of dendrites or cells should inversely relate to *G* and *R* as discussed below:

The primary arm spacing in the columnar growth can be described by an ellipse as shown in Figure 1-44, The smaller radius of curvature of the ellipse is given by:

$$R_{curv} = \frac{b_{cell}^2}{a_{cell}} \qquad \text{Equation 1-12}$$

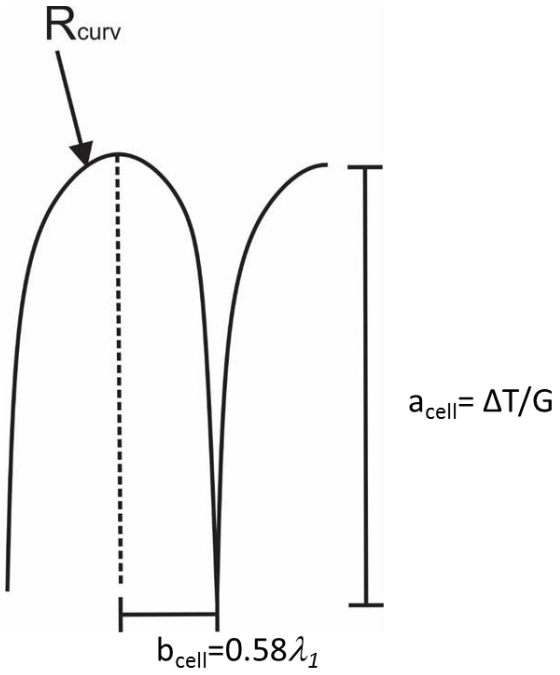

Figure 1-44 Primary arm spacing

The semi-axis, b_{cell}, is proportional to λ_1, where the proportionally constant depend upon the geometrical arrangement of the dendrite. It is assumed that $b=0.58\lambda_1$. The semi-axis length, a_{cell}, is given by the difference between the tip temperature and the root temperature, divided by mean temperature gradient.

$$a_{cell} = \Delta T/G \qquad \text{Equation 1-13}$$

From equation, $\lambda_1 \propto \sqrt{R a_{cell}}$, and:

$$\lambda_1 = \left(\frac{3\Delta T R_{curv}}{G}\right)^{1/2} \qquad \text{Equation 1-14}$$

Also, the dendrite growth according to the hemispherical approximation:

$$R^2 V = \frac{4\pi^2 D_L \Gamma}{\Delta T_0 k} \qquad \text{Equation 1-15}$$

Knowing equation 1-15, for the most important range of cellular and dendritic growth, at moderate growth rates, the following equation can be derived from Equation 1-14:

$$\lambda_1 = 4.3\left(\frac{\Delta T_o \cdot D_L \cdot \Gamma}{k}\right)^{0.25} \cdot R^{-0.25} \cdot G^{-0.5} \qquad \text{Equation 1-16}$$

Where ΔT_o is the equilibrium liquidus-solidus interval, D_L is the diffusion coefficient in liquid, Γ is the Gibbs-Thomson coefficient and k is partition ratio. As v is a selected process parameter, R can be estimated. Direct measurement of G may not be possible, but λ_1 can be measured and thus G can then be experimentally estimated following the theoretical model as expressed in Equation 1-16. This however has not been done in literature.

For understanding the effect of power on thermal condition in processing of CoCrMo alloy in SLM an attempt is made, based on the measured λ_1 and known v, to estimate G and $\dot{T}=dT/dt$ so as to advance the understanding on thermal condition during SLM.

1.9 The Scope of This Research

From our preliminary work, LOF is an important micro-defect that may severely and adversely affect the mechanical properties of SLM parts. It is clear from the above literature review that in SLM of Co-29Cr-6Mo alloy, how laser power up to 400 W affects the geometry of melt pool and subsequently the amount and size distribution of LOF has not been well understood. The crucial and negative effect of SLM spatters on causing large size of LOF had not been observed and explained in literature (before this thesis work). It was also clear from reviewing the literature that solidification mode and grain growth during SLM have not been sufficiently studied. It is commonly understood that mechanical properties of SLM parts depend strongly on solidification microstructure formed during SLM. Furthermore, there has basically been no study to understand the effect of P on grain growth and on cell size, although P is perhaps the most important parameter in SLM. Thus, this Ph.D thesis research on SLM of F75 Co-29Cr-6Mo alloy intends to answer the following questions:

1. How does *P* affect the geometrical features of the melt pool and subsequently the amount of LOF?

2. What causes the formation of large size LOF (although this is a question following our observation on large size LOFs)?

3. What is the dominant growth direction upon epitaxial growth from track boundary and how this direction is selected?

4. Can the planer growth commonly observed to be absent during SLM be confirmed over a wide range of *P* values and theoretically what is the reason for this?

5. How does *P* affect the size of microstructure formed and theoretically does this size of microstructure relate to the thermal condition in the solidification front during SLM?

In the next chapter, experimental procedures and details of analytical facilities are described and explained. In chapter 3 and chapter 4, detailed results of experiments and analysis are presented and discussed. Questions 1 and 2 above will be answered in Chapter 3 and questions 3-5 will be answered in Chapter 4.

2 Experimental Design and Procedures

In this chapter, SLM and the material are first outlined. Then, SLM conditions are given in detail followed by the in-depth explanation of metallurgical preparation and method of image analysis using ImageJ. This is followed by describing the SEM, EBSD and synchrotron examination and analysis for evaluating LOF and the effect of SLM parameters on it. Finally, the growth direction identification relating to solidification of SLM melt pool is being described.

2.1 SLM Machine

A Renishaw AM250 SLM machine as shown in Figure 2-1 (Pmax = 400 W and default laser spot size is 140 µm in diameter) was used for all the SLM experiments. The Renishaw AM250 is an industrial 3D printer made by Renishaw, a manufacturer based in UK. This machine employs a high-powered fibre laser to fabricate 20 µm to 100 µm thick layers parts directly from 3D CAD design. It utilizes a point exposure scan pattern where a single point is radiated by the laser beam, the laser turns off, repositions to the next point and melts it. The scanning speed of laser beam is derived from the distance between the points divided by the exposure time. The spot exposure strategy allows fabrication of finer detail products as a static melt pool is more stable than a dynamic melt pool formed by a continuous movement of laser beam. Currently the Renishaw system is the only commercial machine to use the point exposure scan strategy [102].

Figure 2-1 Renishaw AM250 SLM machine [102]

One of the strongest features of the AM250 is the capability to alter between a various array of materials very fast. By using the AM250's removable hopper, the powder can be switched between 316L and 17-4PH SS, H13 tool steel, aluminium AL-Si-12, titanium CP, Ti-6AI-4V and 7Nb, cobalt-chrome (ASTM75) and Inconel 718 and 625. The valve interlock system makes the addition of extra powder during prints possible. Also, with the presence of a gas knife and a heated build plate the hazards of sooty emissions and using reactive metals like titanium and aluminium are minimized.

The build area of machine is 250 mm (X-axis) x 250 mm (Y-axis) x 300-360 mm (Z-axis), and it has a fully-welded vacuum chamber that is suitable for low-pressure evacuation. This chamber helps to keep the oxygen concentrations under 50 ppm using low gas consumption to allow safe use of reactive materials, which also allows for fabricating parts with overall better mechanical performance and material integrity [102].

2.2 F75 Co-29Cr-6Mo Powder

The cobalt chromium powders were supplied by Renishaw. Composition of the powders, according to the supplier, met CoCrMo SF75 specification (27-30wt%Cr, 5-7wt%Mo, <0.25wt%Ni, <0.2wt%Fe, <0.22wt%C, <0.006wt%B plus other minor elements, balanced Co). The size range of the powders was 15-45 µm, as specified by the supplier. Figure 2-2 shows the morphology of the cobalt chromium powder particles illustrated by SEM and their size distribution. SEM observation shows a small portion of particles are less than 15µm in size.

a)

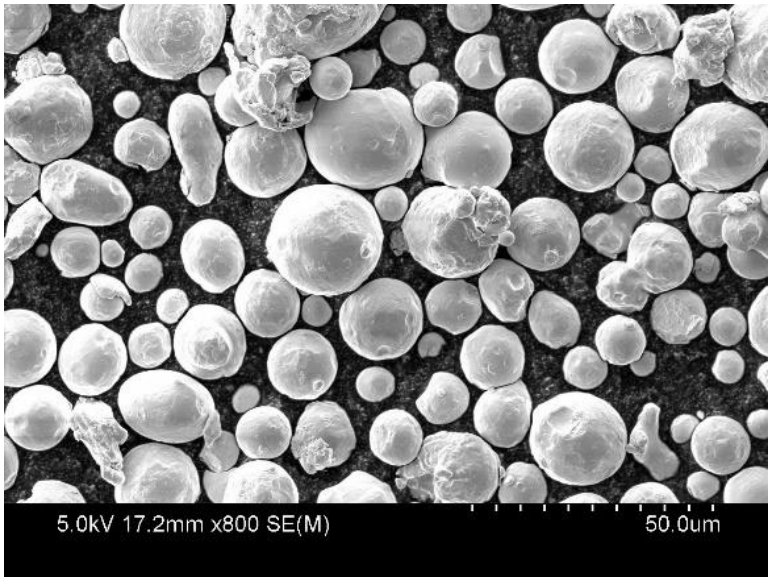

b)

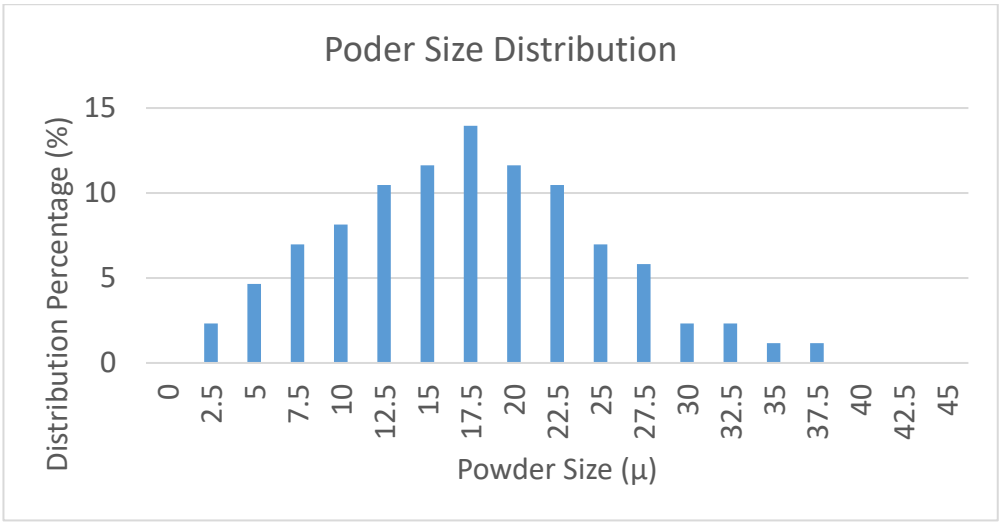

Figure 2-2 a) SEM of CoCrMo powder b) Size distribution of the powder

2.3 SLM Parameters

Two base samples were made using parameters recommended by Renishaw: P = 180 W, v = 700 mm/s, w = 125 μm, h = 30 μm (thus E = 69 J/mm^3) and cross hatching strategy. Nine (9) other pairs of samples, as shown in Figure 2-3, were made using P values ranged from 200 to 360 W with an increment of 20 W, while other parameters were kept the same. The corresponding E values were thus 77 and 159 J/mm^3.

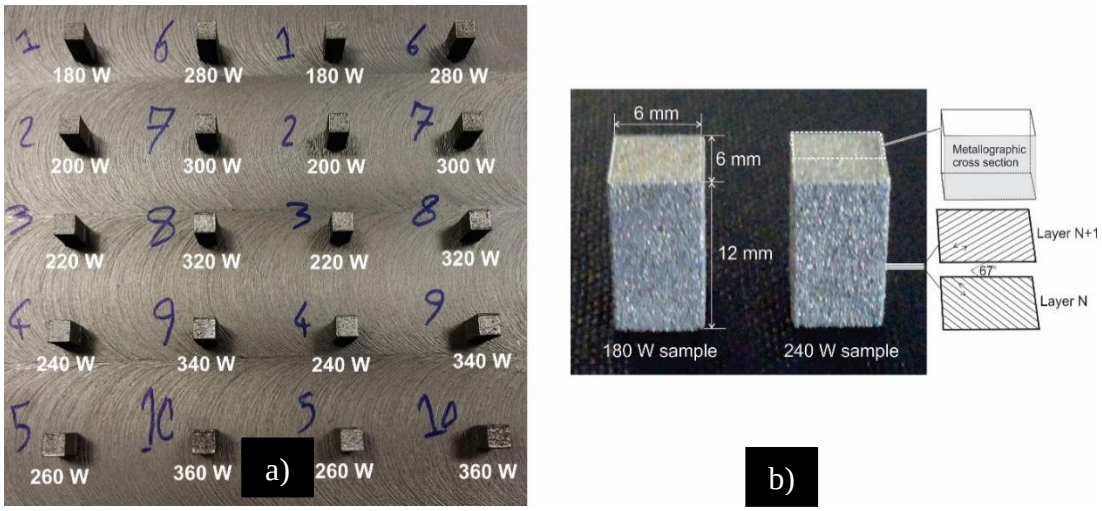

Figure 2-3 Selective laser melting samples, (a) as-built samples on the base plate with the P value marked underneath each sample, and (b) dimensions of a sample together with scan angle 67° between each layer and sampling for analysis illustrated. In (b) the final scan direction is also indicated.

The built sequence of each layer started with the two 180 W samples (samples marked 1 in Figure 2-3a). After the layer was laid for 180 W samples, P was increased automatically (following the program setting of the SLM run) to 200 W to lay the layer for the two 200 W samples (marked 2 in Figure 2-3). This layer laying with 20 W increment continued to the two 10th samples which are 360 W samples. Then the same sequence repeated in the next layer and this sequence was the same till the final layer for the two series of samples. The built area of a sample was 6 mm by 6 mm and the built height was 12 mm, as shown in Figure 2-3b. A 12 mm height means a sample built with 400 layers. Each layer is built following the common edge contouring and then hatching. The cross-hatching strategy,

as is also shown in Figure 2-3b, means the laser track direction rotates 67° after each layer.

2.4 Sampling for Metallography

One batch of samples was sectioned using a CNC wire cutting machine parallel to the building direction, and an example is given in Figure 2-4. For examining the cross-section of the samples, the metallography samples were mounted using resin powder. The mounting powder consisted of a thin layer of conductive powder (ConduFast) on the bottom and the rest is hot mounting SEM resin (PolyFast). After mounting the samples, wet coarse and fine grinding using rotating disks with 180, 500, 800, 1200 grit silicon carbide papers were conducted. Then, all the samples were fine polished using a TegraPol-25 (made by Struers) automatic polishing machine on cloths of 6µm, 3µm and finally 1µm successively. The samples were polished to a level to produce mirror like finish.

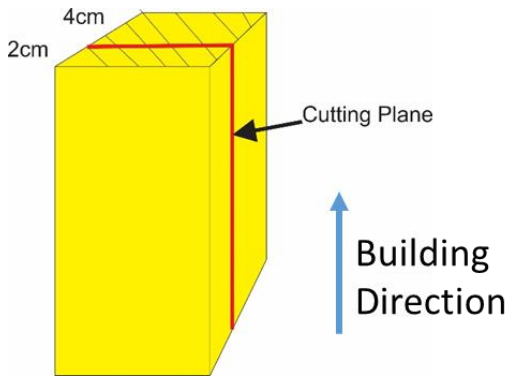

Figure 2-4 Schematic of cutting section of the sample

The final step of preparation is electrolytic treatment using LectroPol–5 automatic polisher in a solution of 10% H_2SO_4 and CH_3OH at 6 V for 25 seconds at room temperature. This final step is specially needed for electron backscatter diffraction analysis as the electron diffracted and detected by the EBSD camera originated generally from the top 50-100 nm of the sample, a surface without any type of distortion, oxide or reaction products layers is crucial. Therefore, polished specimens were immersed face

down in etching solutions right after the polishing steps to remove the surface reaction layers right before conducting SEM and EBSD. The detailed description on SEM and EBSD analysis will be given in section 2.7.

2.5 Track and LOF Measurement

Observation on the geometry of track & LOF area of the samples were carried out using a Nikon optical microscope (FX-35A). Quantification of the LOF area was implemented from image analysis by using ImageJ software which is capable of automatic quantification of the area occupied by the LOF in the optical image. Five and four images were taken along the width and length of sample's cross section, respectively. In total twenty images were analysed for each sample. For identification the LOF in optical micrographs, using Photoshop the colour of LOF is changed into a different colour, in this study white (Figure 2-5a), as LOF has the same colour, black, as the track boundary which causes mistake in LOF area quantification. Then, using the Threshold tool in ImageJ, the area of LOF can be selected. This area of the image becomes red as shown in Figure 2-5b. As shown in Fig 2-5a, with adjusting the threshold, all the LOF spots will turn red. Then using the Analyse toolbar, this area fraction of LOF will be measured. For better accuracy this analysis was conducted three times for each image. Although the analysis from 2D optical images does not deliver precise information on the real 3D morphology of the LOF and the real density of the specimen, it definitely can offer an indication on the quality of the parts.

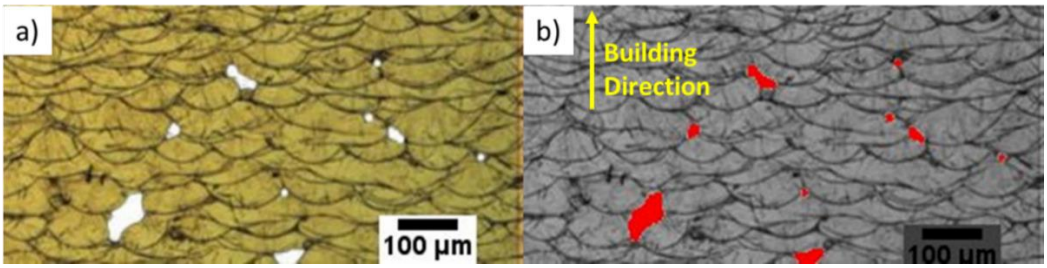

Figure 2-5 a) Optical micrograph of LOF painted with white using Photoshop, b) after adjusting the threshold on the image LOF turned red

2.6 LOF Detection Using Synchrotron X-ray Imaging

3D characterisation of the LOFs was performed by synchrotron computed tomography (SCT) at the Imaging and Medical Beamline (IMBL) of Australian Synchrotron. Figure 2-6 shows the small cubic specimens and their dimensions that were extracted from the cubic samples. Samples built with 180 W, 200 W, 220 W, 240 W, 280 W, 320 W and 360 W laser power were examined by this technique.

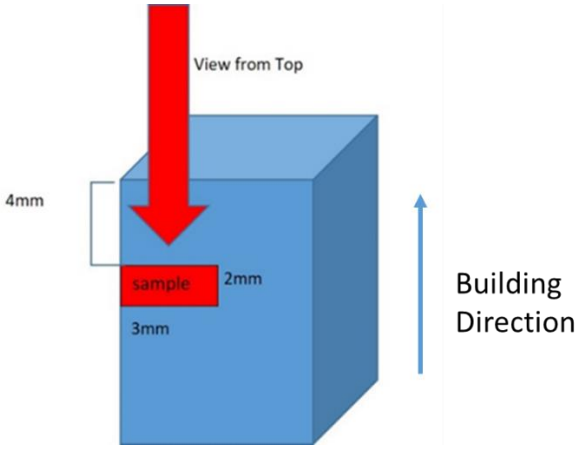

Figure 2-6 Dimension of the synchrotron specimen

Computed tomography measurements are performed in one of two beamline operating modes, designated Mode 2 and Mode 3 (Figure 2-7).

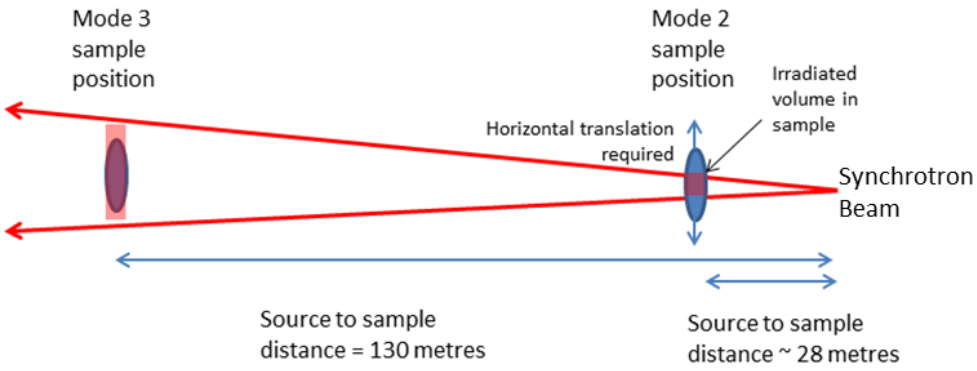

Figure 2-7 Schematic of mode 2 and mode 3 for tomographic data collection at IMBL

Samples in this study were measured using mode 2, where the vertical beam height was ~5 mm. Seven individual samples were analysed and loaded into a 1 mL syringe for batch

measurement using serial scanning. Serial scanning of successive samples was achieved by translating the sample stage vertically after each tomography scan completed.

For purposes of reconstruction all projections taken at a given angle were stitched together such that a single tomographic reconstruction was done for all samples present in the sample holder simultaneously.

A monochromatic beam energy of 70 keV was required to penetrate the highly absorbing alloy samples. Transmission projections were collected using the Ruby II detector. Exposure settings are summarized below in Table 2-1.

Table 2-1 Synchrotron scanning parameters

Energy (KeV)	70
Pixel Size (µm)	5.7
Base Exposure (s)	0.035
Exposure/ Step	0.5
Acquisition time (s)/Projection	0.07
Rotation Range (deg)	200
Total Projections	2000
Angle step/ Projection	0.1

Reconstructed tomographic slices are first output as 32-bit files and have also been converted to 8-bit after applying a threshold to the pixel intensities. Figure 2-8 shows a image of the same reconstructed slice from sample 180 W that have different intensity thresholds applied, altering the visibility of the voids. The concentric ring structure that can be seen clearly in Figure 2-8a are ring artefacts that are due to defects on the detector array or scintillator that are not completely removed by background correction. The LOF

area in the sliced micrographs was measured using ImageJ the same way that was used for optical images by changing the intensity thresholds.

Voids in the size range 25 - 50 μm are easily visible in the slice shown in Figure 2-8. LOF fraction area measurements were done using ImageJ with the same method that was used for measuring the LOF area for optical images. A video showing a fly through of the reconstructed slices has been produced for each sample. The videos provide a useful quick overview of the general void structure in the samples.

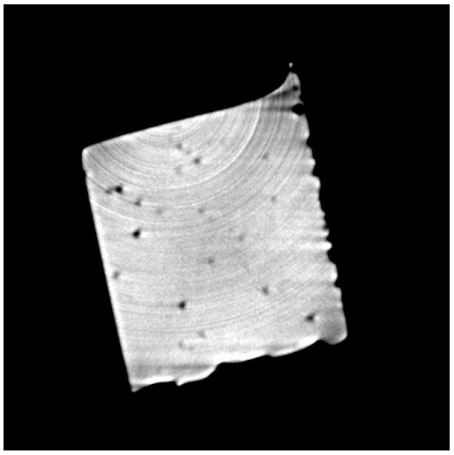

Figure 2-8 Reconstructed slice from sample 180WB1

2.7 SEM and EBSD Analysis

A Hitachi SU-70 field emission scanning electron microscope (SEM), operating in high vacuum atmosphere, has been used for the observation of microstructural details and track measurement in this study. A 20 kV accelerated voltage was used for taking the images.

Electron backscatter diffraction (EBDS) is one of the most powerful methods which can be employed to study the microstructure of a sample and the grain growth direction based on crystallographic analysis. Thus, EBSD can be particularly beneficial to the investigation of the microstructure and the grain growth direction in SLM samples. The used EBSD system in this study is Thermo-Scientific system.

EBSD is constructed on the interaction at the surface of a polished crystalline material between the high-energy electron beam and the crystal grains. Because of the interaction between the e-beam and the crystal grain a coherent or incoherent and elastic or inelastic electron scattering is created. When all the electrons in the scattered wave are in phase, coherent scattering forms. Alternatively, when the electrons are scattered away from the material in multiple directions and are out of phase incoherent scattering forms. If during the interaction and consequent change in direction the electrons do not lose their energy, elastic scattering takes place. In contrast, inelastic scattering indicates a loss in energy [103]. Figure 2-9 shows a schematic illustration of the formation of the EBSD signal (or EBSD patterns) that is employed to acquire the orientation information of the material in evaluation.

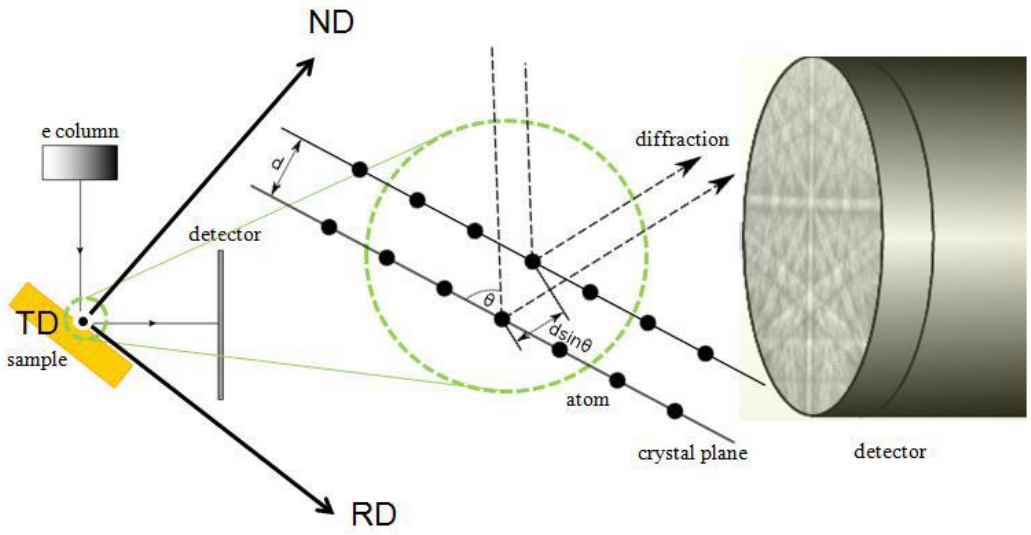

Figure 2-9 Schematic of the generation of the EBSD signal. The sample coordinate system is also shown in the Figure (ND, RD, TD) [103]

EBSD patterns are created when the incident electrons of the e-beam collide and backscatter elastically from the atomic planes of the crystal grain that satisfy the Bragg's law [104]:

$$n \cdot \gamma = 2d_{hkl}sin\ddot{\theta} \qquad \text{Equation 2-1}$$

Where n is an integer number, γ is the wavelength of the incident electrons, $\ddot{\theta}$ is the diffraction angle for a particular plane [hkl] and d_{hkl} is the interplanar spacing for that plane. The backscattering of the electrons in the Bragg condition leads to formation of Kossel cones with an angle between them. When a sensitive phosphor screen is places near the surface of the sample, a portion of the Kossel cones can be captured. Theses captured Kossel cones have a band pattern on the phosphor screen, where each band, known as Kikuchi band, has a luminance that is dependent on the intensity of the diffraction. To be more precise, the pattern of Kikuchi bands captured on the phosphor screen is known as an EBSD [103]. An example of diffraction pattern is illustrated in Figure 2-10.

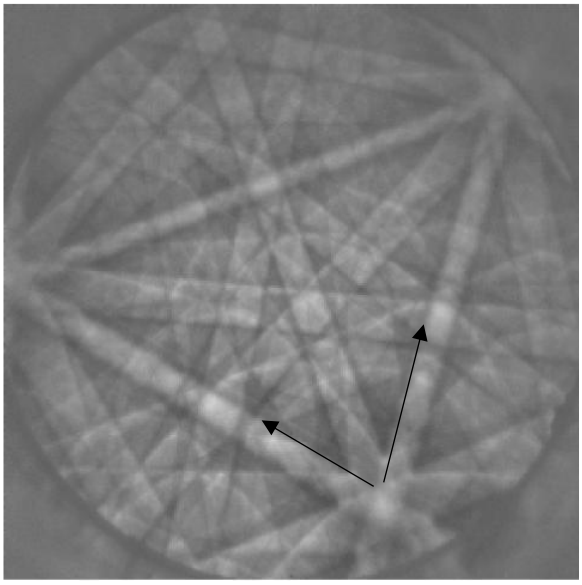

Figure 2-10 Example of EBSD pattern showing zone axis (pointed by the arrows) [103]

"EBSD patterns carry two types of information. The crystal symmetry of the grain in analysis determines the intersection of the Kikuchi bands in the pattern (zone axes). Thus, from the analysis of the Kikuchi bands intersections, the crystal structure of the grain can be deduced. Also, it has been shown that there is an inverse correlation between the width of the Kikuchi bands and the interplanar spacing of the grain crystal structure. The EBSD pattern contains therefore all of the angular information that are necessary to calculate the

orientation of the grain in analysis relative to a fixed coordinate reference system. Interpreting the EBSD patterns generated by the grains allows the identification of the phases existing in the material and the orientation of each individual investigated grain" [103].

"The interpretation of the EBSD patterns (also known as indexing) can be performed manually or automatically. The automated indexing of the patters relies on a mathematical algorithm known as Hough transform that allows the detection of the location of the Kikuchi bands in the EBSD pattern. Finally, once the crystal structure (or material phase) is deduced from the analysis of zone axes in the patterns, the interplanar spacing and angles that derive from the width of the measured bands are compared to theoretical values to identify most probable crystal orientation" [103].

"An intuitive way to represent the grain orientation is offered by discrete pole figure. Discrete pole figure are stereograms that represent the orientation of individual grains relative to an external sample frame of reference. In practise the plot is built considering the projection of a specific crystal cell plane normal (pole) onto a unit sphere based on the sample coordinate system (Figure 2-11). The projected points are then connected to the southern hemisphere of the unit sphere. The intersections with the equatorial plane consist thus of distinct univocal points for a specific crystal cell orientation. Discrete pole figures provide a comparison between orientations of the crystal grains, and are very useful to study orientation relationship between adjacent grains and different phases" [103].

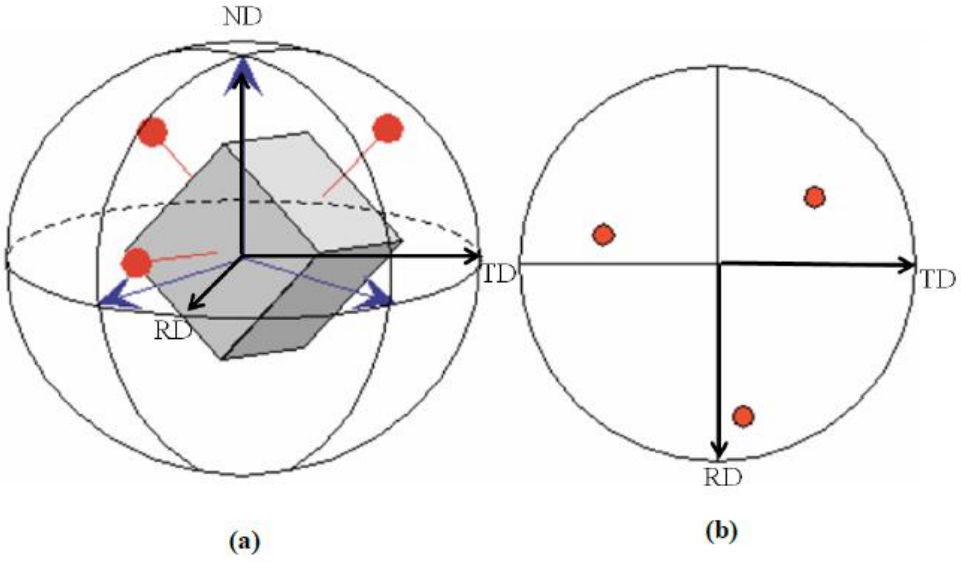

Figure 2-11 a) Spherical projection of the poles of the crystal cell b) equivalent discrete pole figure representation. [103]

In this study, an acceleration voltage of 20 KV, accompanied with a working distance of 26 mm and a sample tilt angle of 68° were chosen in order to maximize backscattered electron diffraction. The reason for this long working distance is because the sample is tilted at angle of 68° which makes the top edge of the mounted sample closer to the camera. This reduction in the distance between the sample and camera might lead to collision which will substantially damage the camera. For prevention of this type of incident a safe distance of 26 mm is used to capture images in EBSD. The EBSD process was conducted on a FE Hitachi SU-70 using the fully automated data acquisition programs 'NSSTM' that acquire EBSD patters from the scan of the sample.

Figure 2-12 shows an SEM image and corresponding EBSD orientation map and obtained data from sample that was built with 180W laser power. In Figure 2-12b shows that different areas of the EBSD image have different colours which suggests different grains. Figure 2-12c shows a result of point and shoot analysis from the green grain close to the track boundary that is illustrated with a blue cube. The orientation of the cube is aligned with the cells growth which will be discussed in detail in chapter 4. Figure 2-12d shows

the given orientation data from the EBSD point analysis which indicates the orientation of the cube.

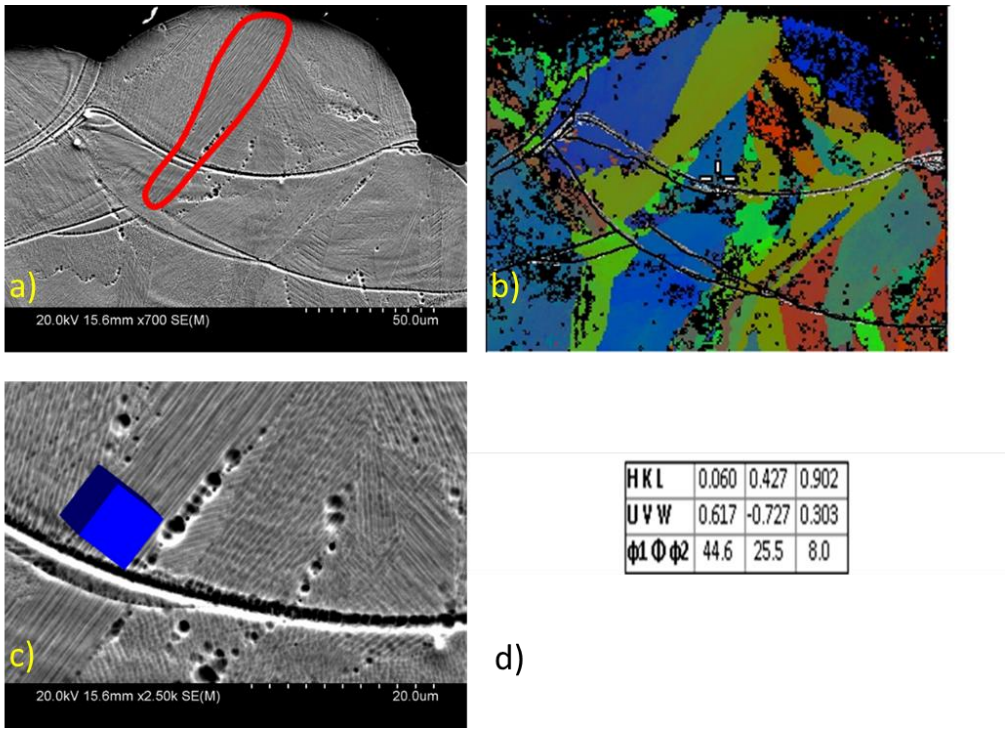

Figure 2-12 a) SEM image b) corresponding EBSD c) magnified SEM image of (a) from track boundary with a point EBSD analysis d) Euler angles for the corresponded cube shown in c.

2.8 Growth Direction Identification

Grown direction of cells can be readily identified through EBSD analysis. Since cellular growth during SLM melting of metallic alloys is commonly observed in the literature, to evaluate cellular growth through observation using micrographs, it is helpful to understand the geometrical features of cells appearing in a micrograph reference plane. The reference growth direction is the angle (ω) between the direction along the elongated cell and the direction normal to the micrograph plane. As illustrated in Figure 2-13a, for group 1, the cell growth direction is normal to the track cross section that is the micrograph plane. In Figure 2-13b, cells intercepted in the track cross section show different degrees of elongation, depending on ω. In the figure, w_{c1} represents the largest

width and w_{c2} the smallest width of a cell in the cross section. Thus, $\omega = 0°$ and the aspect ratio (AR) = cell width 1 (w_{c1})/cell width 2 (w_{c2}) = (w_{c1}/cos30°)/w_{c1} = 1.15.

For $\omega = 45°$, AR = 1.63 but visually w_{c1} may only be viewed slightly larger than w_{c2}. For $\omega = 70°$, AR = 3.38, w_{c1} can be seen clearly larger than w_{c2}, and thus, projected growth direction can readily be identified. Figure 2-13c shows the relationship between ω and AR. Considering that image detail and sharpness of microfeatures in a micrograph should normally be much inferior in comparison with simple drawing as in Fig. 2-13a, it may be suggested that the projected growth direction would be increasingly difficult to identify for ω <50° (AR<1.8).

a)

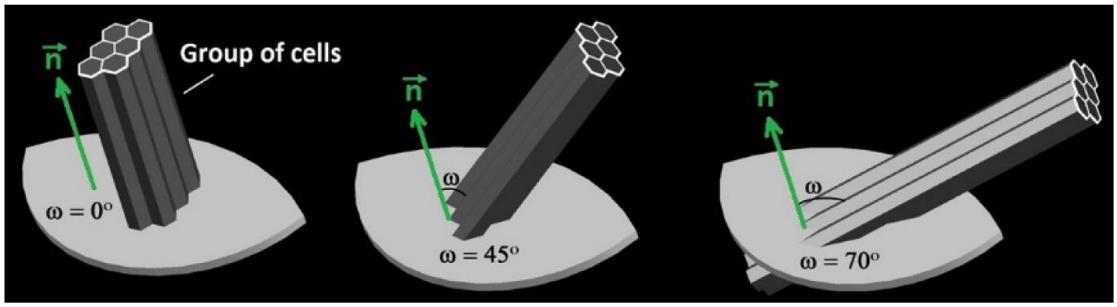

b)

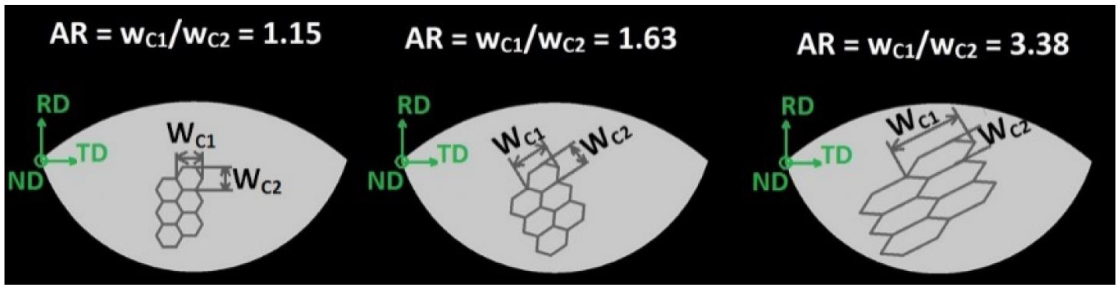

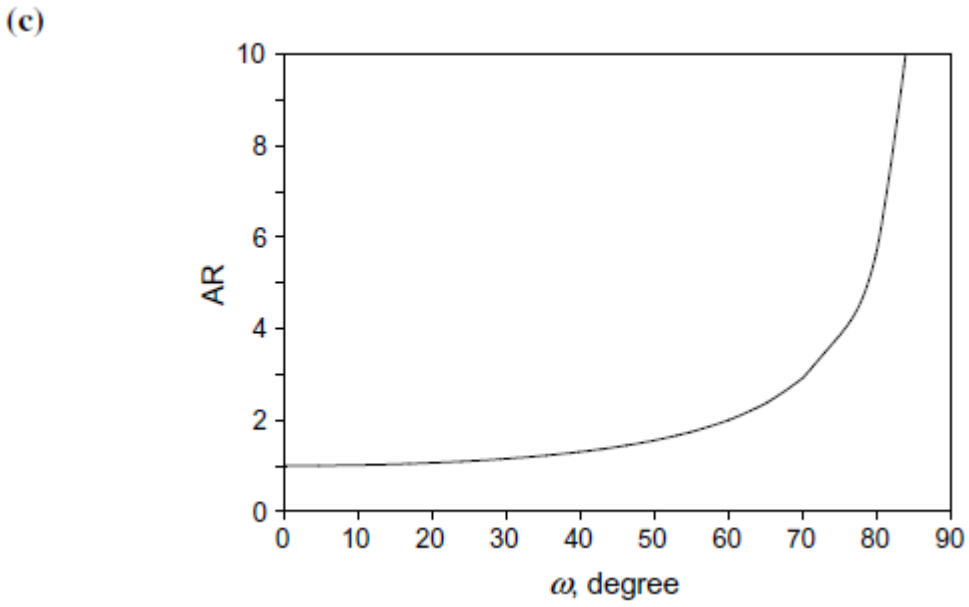

Figure 2-13 Illustrations of a) 3D view of three identical track cross sections each intersecting a group of elongated cells at an angle x = 0°, 45° and 70°, respectively, b) view of the three track cross sections together with the intersected traces of cells having reorientated to be normal to the viewing direction of observer, with values of AR defined as the ratio of the largest cell width, w_{c1}, over the smallest cell width, w_{c2}, also indicated, and c) AR plotted as a function of ω.

In Figure 2-14, two identical unit cells from EBSD spot analysis are shown. They are identical resulting from epitaxial growth crossing (track boundary) TB. However, the appearance of cells before and after TB are different and their <100> grown direction are suggested by the arrows. In Figure 2-14, measurement of λ_1 is illustrated. Depending on the orientation of the grain (a group of cells), the cells may appear long or short in micrograph meaning large or low aspect ratio, respectively. For grains with a low aspect ratio appearance, cell orientation from EBSD analysis was used so that the crossing line for λ_1 measurement is normal to the cell grown direction. Measurements were conducted in locations 5-10 μm away from TB.

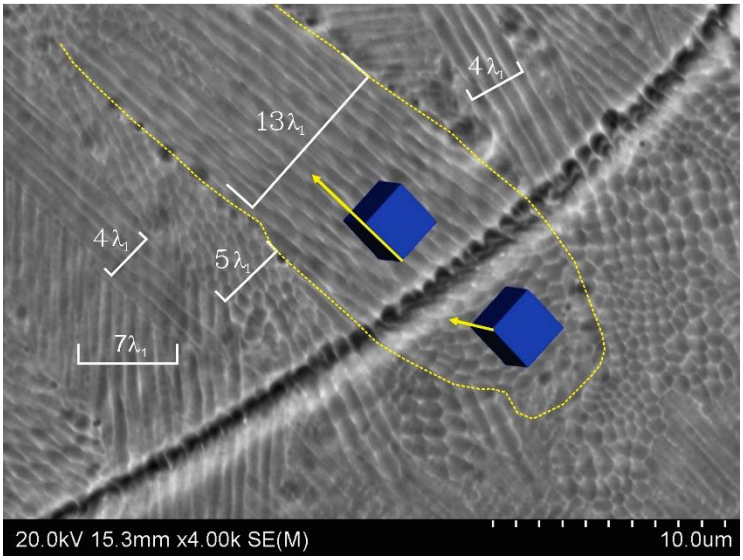

Figure 2-14 SEM micrograph showing solidified cellular structure in a sample made with P = 220 W and also: unit cell each with grown direction indicated for the grain before and after TB, respectively, and examples illustrating $\lambda 1$ measurement.

To aid the illustrattion of cellular growth direction, a moving melt pool is schematically illustrated in Figure 2-15. The melt pool represented by the green outline has moved to one as presented by the red outline along the scan direction (SD) for a distance d_v after a time period (t1 to t2). Cross section A-A' is normal to the scan direction (SD). After SLM, samples were however sectioned along B-B' which has been explained and indicated in Figure 2-3, and thus B-B' is 20° to A-A'. Both A-A' and B-B' are parrellel to build direction (BD). Transverse direction (TD) is normal to both SD and BD. As B-B' is the sample metallography plane, unit cell orientations after EBSD analysis have been provided by the software based on this plane and the sample coordinate (x_{sp}-y_{sp}-BD). As an example, cellular solidification starting at a TB location O in Figure 2-14 is illustaretd. The growth direction is indicated by the green arrow along OP. EBSD analysis has provided direction information ϕ, between OP and OR where OR is normal to TB in location O in y_{sp}-BD (metallography) plane of the x_{sp}-y_{sp}-BD coordinate. The growth direction with ϕ in this x_{sp}-y_{sp}-BD coordinate needs to be expressed as θ in the SD-TD-BD (or the equivalent SD_o-TD_o-BD). This is simply done by using auto-CAD and rotating

x_{sp}-y_{sp}-BD to SD-TD-BD by 20° about BD carrying the crystal unit cell, followed by measuring θ directly.

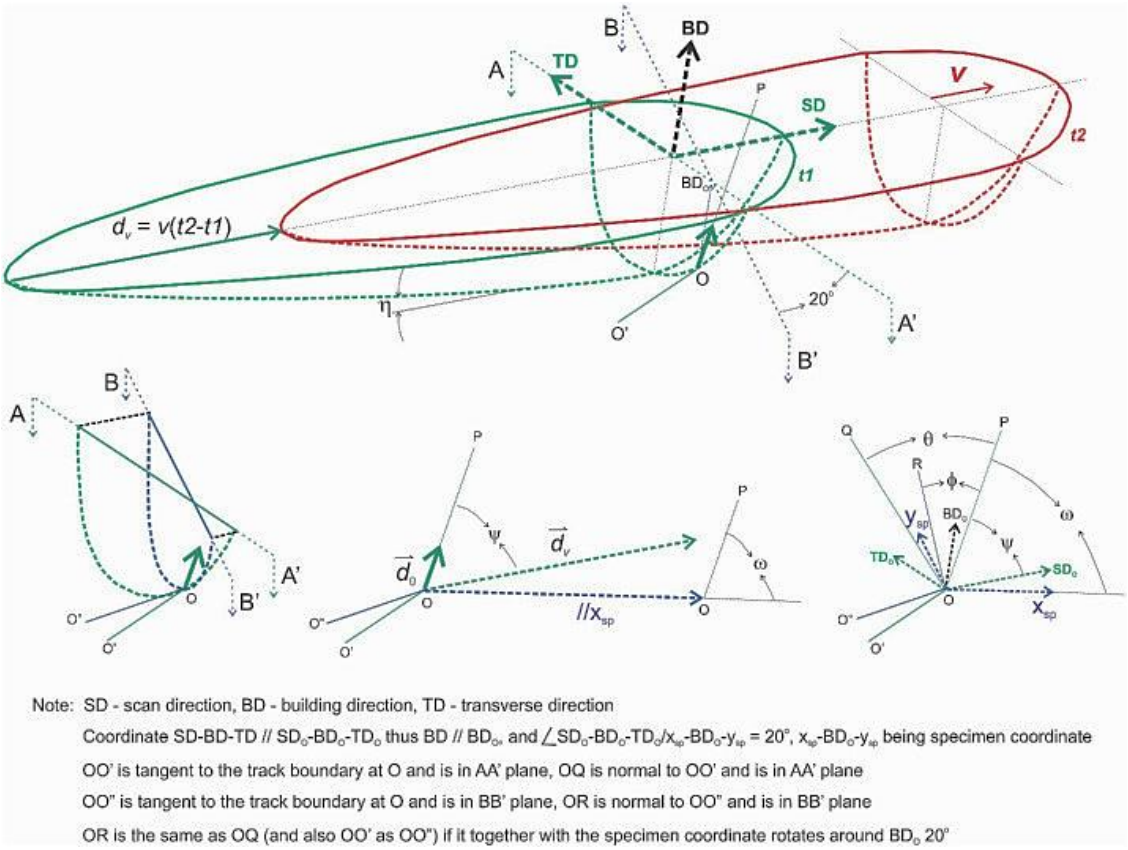

Note: SD - scan direction, BD - building direction, TD - transverse direction
Coordinate SD-BD-TD // SD_o-BD_o-TD_o thus BD // BD_o, and ∠SD_o-BD_o-TD_o/x_{sp}-BD_o-y_{sp} = 20°, x_{sp}-BD_o-y_{sp} being specimen coordinate
OO' is tangent to the track boundary at O and is in AA' plane, OQ is normal to OO' and is in AA' plane
OO" is tangent to the track boundary at O and is in BB' plane, OR is normal to OO" and is in BB' plane
OR is the same as OQ (and also OO' as OO") if it together with the specimen coordinate rotates around BD_o 20°

Figure 2-15 Illustration of a moving melt pool and cellular growth direction as indicated by the solid green arrow. The orientation relationships between the growth direction and the plane (A-A′) normal to SD and the micrograph plane (B-B′), respectively, are illustrated. The two coordinates, SD-TD-BD associated with A-A′ and coordinate associated with B-B′, are also illustrated. (For interpretation of the references to colour in this figure legend, the reader is referred to the web version of this article. [105])

3 Geometrical Features of Tracks and Lack of Fusion

In this chapter, observation and measurements on LOF in samples built with different P values are presented. First, geometry and shape of the track are studied which leads to the discussion on how track geometry is linked to the formation of LOF in samples. The results of image analysis on the area fraction of LOF using optical microscopy and synchrotron tomography data are given to illuminate the relationship between *P* and area fraction of LOF (f_{LOF}). Furthermore, the results of the effect of spattering on formation of abnormal LOF is presented. Finally, an observation on the size of melt pools accompanied by discussion and analysis on the mode of melting is given.

3.1 Morphological Features of Tracks and LOF Using Basic SLM Condition

Top surface features of a 180 W sample are shown in Figure 3-1. A single SLM track is seen similar to a normal fusion weld with the appearance of elongated ripples resulting from solidification of tear drop shaped melt pool typical of high speed welding, although a SLM track is small in size. Many tracks, one following/lapping another, are thus seen in the image. Spatters, typically seen in welding, are clearly distributed on the sample surface. In this 180 W sample surface (Figure 3-1), track edges are quite wavy, meaning that the track width (w_{Tk}) is inconsistent. This then must be the result of non-stable melt width during SLM using 180 W. As is also clear in Figure 3-1, there are many local gaps/valleys present intermittently along the wavy track edges.

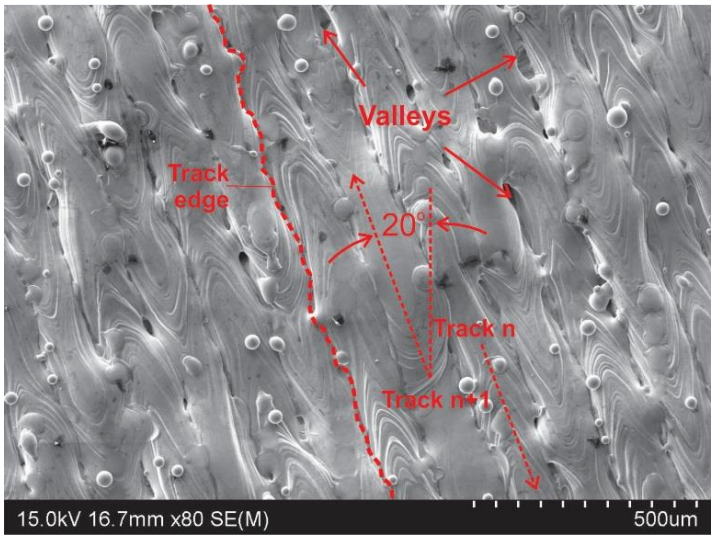

Figure 3-1 SEM image of top surface of 180 W sample with SLM scanning directions for two neighbouring tracks, an irregular track edge and valleys between tracks indicated.

Optical micrograph of a 180 W sample is shown in Figure 3-2. The common AM features of the tracks laying one by one to form a layer and layers built one after another are clear. Due to the scan strategy of rotating 67° after each layer, the size (cross sectional area) of a track in a layer differs from the one below. In the top layer of the sample, the direction normal to the track cross section in Figure 3-2 is ~ 20° to the scan direction and this has been indicated in Figure 3-1. Inconsistency in size and some tracks not connecting to their neighbours seen in Figure 3-2a agree with the wavy track edges and local valleys seen in Figure 3-1. LOFs are clearly seen distributed throughout. LOFs are normally present in between tracks, particularly in the triple junctions. However, occasionally there are large size LOFs and Figure 3-2b shows one in this 180 W sample. Clearly, this LOF is neighbouring more than three tracks, differing in nature to other LOFs seen in the figure. Details of this type of abnormal LOFs will be examined more closely in section (3.4).

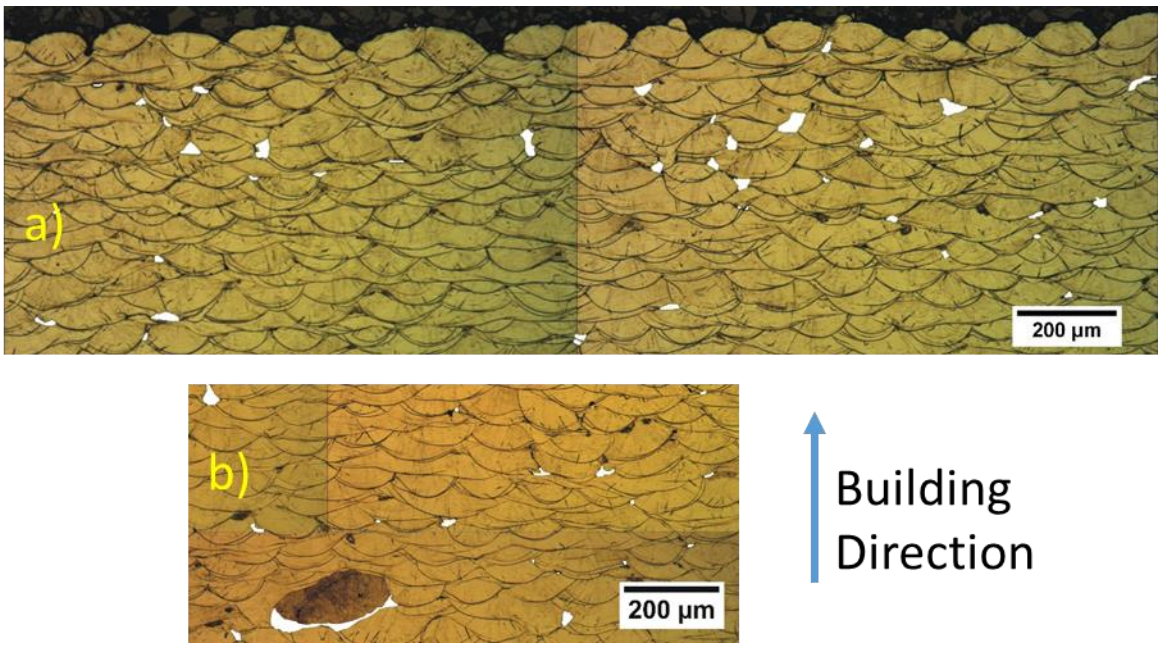

Figure 3-2 Optical micrographs of 180 W sample with LOF voids are assigned white using Image J, (a) tracks of the top layer included and (b) an abnormal LOF found in the same cross section.

For normal LOFs, in order to aid the discussion of a track profile, variables for a track cross section following what are commonly used for describing weld tracks are schematically illustrated in Figure 3-3. The reinforcement portion can only be examined in top (final) layers in cross sections, as any other layers below have been remelted significantly. All samples have been sectioned with the metallography plane parallel to build direction, as is illustrated in Figure 2-3. For any cross section of a track in a metallography sample, the direction normal to the cross section is at an angle ($\dot{\theta}$) to the track scan direction. This means $W_{Tk-\dot{\theta}} = {W_{TK}}/{cos\dot{\theta}}$. For a connecting/lapping track, W_{Tk} cannot be measured directly. As illustrated in Figure 3-3c, to approximately estimate W_{Tk}, the overlapping side of a track is traced and this trace is then used for the other side that has been overlapped to form a "complete" track for W_{Tk} measurement.

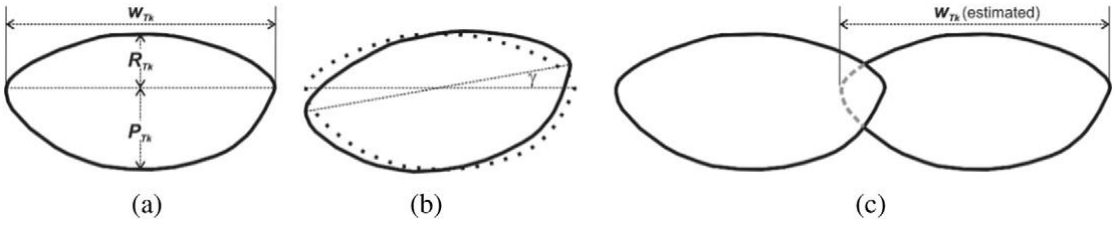

Figure 3-3 Schematic illustrations of track cross sections: (a) with track width (W_{Tk}), reinforcement (R_{Tk}) and penetration (P_{Tk}) shown, (b) angle γ introduced and (c) showing how W_{Tk} is estimated for lapped tracks..

As has already been shown, for the 180 W sample (Figure 3-2), insufficient overlapping is clear in many locations where two tracks do not connect. Some of these locations should be prone to form LOF during next layer building. We simplify first by drawing a schematic of SLM scanning with the scale realistic to help the discussion on how LOF may form. This is shown in Figure 3-4. Measured values of $R_{Tk} + P_{Tk}$ and W_{Tk}, as can also be estimated in Figure 3-2, are on average ~ 60 μm and ~ 133 μm, respectively. In drawing the illustration shown in Figure 3-4, $W_{Tk-\dot{\theta}}$ (where $\dot{\theta}$ = 20°) for the top layer is 133 μm, taking γ = 0. The second layer has been drawn based on the tracks having rotated (clockwise) of 67°, then, W_{Tk} - (67-20)° = 183.9 μm. This process has repeated 4 times and thus total 5 layers have been drawn. Powder particles drawn in the figure are less than 45 μm in size, as specified in powder specification data and seen in Figure 2-2.

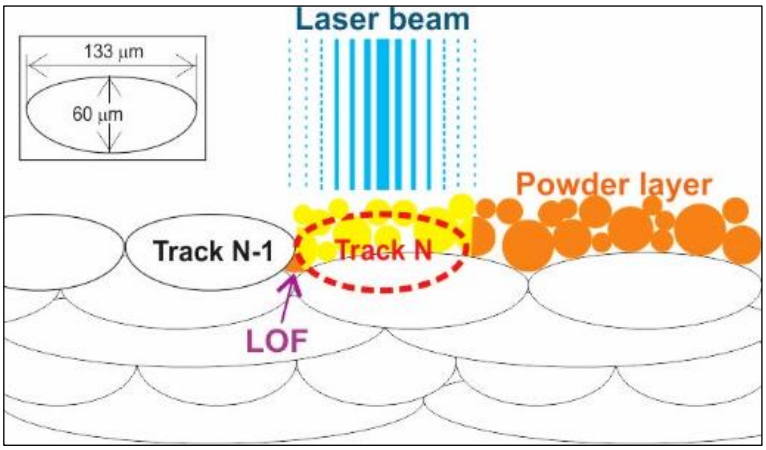

Figure 3-4 Schematic illustration of laser beam, powder layer with the portion (yellow) under the laser beam to melt and to form track N and to form LOF.

As Figure 3-4 shows, after track N-1 has formed, laser beam returns and melts the powder (colored yellow) and a portion of the track in the layer below to form a melt (outlined red) which then solidifies as track N. Two neighboring tracks just touch (connect) without overlapping, as $W_{Tk}/\cos 20° = 133\mu m/\cos 20° = 125\mu m = w$. Clearly, LOF forms underneath the connecting point, as shown in Figure 3-4, if the melt does not infiltrate in that small space or if there are un-melted powder particles in that space. In Figure 3-4, the connecting point of tracks (N-1 and N) has been drawn to vertically coincide with the connecting point of the two tracks in the layer below. For any two layers, considering 67° change in scan direction after each layer, it can be shown that there are 33/mm^2 locations where the connecting points of two tracks in both layers are vertically aligned. The (vertical) distance between the two connecting points is h. In the next layer building, tracks laid with the average size should not significantly affect these LOFs already formed.

As has been pointed out, there is clearly an inconsistency in track size of the 180 W sample. This means in tracks where $W_{Tk\,(left)} \cdot \cos\gamma_{(left)} + W_{Tk\,(right)} \cdot \cos\gamma_{(right)} > 2w = 250\ \mu m$, the two tracks connect with one slightly overlaid by the other. In locations of under sizes, the two tracks do not connect, leaving a location prone to form a LOF. For the 180 W sample, the average values R_{Tk} and P_{Tk} were measured to be 22.0 μm and 38.9 μm, respectively. A value of $R_{Tk}/P_{Tk} = 22.0/38.9 = 57\%$ is a high value meaning that, as can be observed in the top layer in Figure 3-2, the portion of reinforcement is high and penetrating capability is not high. This suggests that the shape of the melt track surface is strongly influenced by surface tension in the tail portion of the teardrop shaped melt behind the laser spot during SLM. In general, the insufficient size of tracks for lapping and low penetrating capability have resulted in a high number of LOF.

3.2 Effect of Increasing Laser Power on the Track Size and Amount of LOF

Two top surface images of samples made using higher *P* values are shown in Figure 3-5. Comparing to 180 W SLM (Figure 3-1), increasing *P* to 240 W has smoothed the track edges slightly but the number of local gaps/valleys are seen to reduce quite significantly. This may mean the average w_{Tk} value for the 240 W sample is significantly larger than that of 180 W sample. Thus, overlapping of tracks has improved and the number of valleys has reduced significantly. For the sample made using the highest *P* value, as shown in Figure 3-5, the track edges are seen largely straight and there are basically no gaps/valleys. This means a high melt shape stability and a sufficiently high average w_{Tk} value so that no lack of track overlapping has occurred.

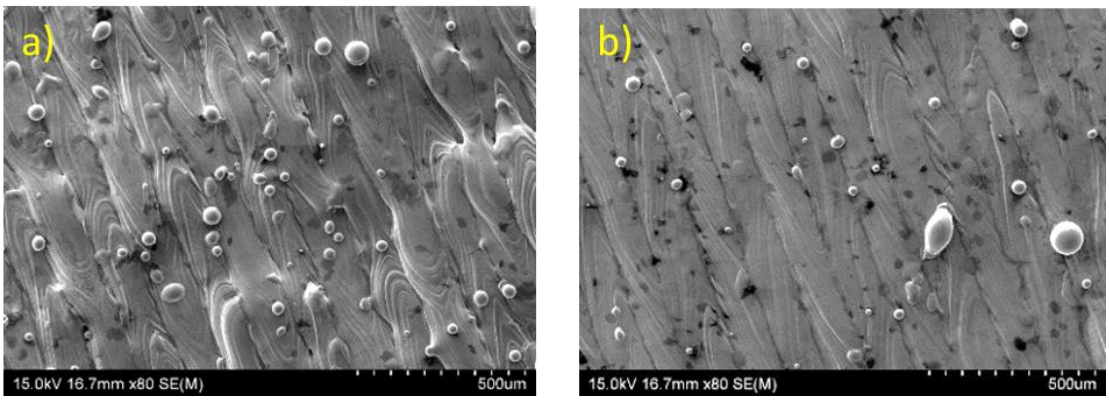

Figure 3-5 SEM images of top surfaces of SLM samples, (a) 240 W and (b) 360 W.

Metallographic features observed on cross sections of tracks that are presented in Figure 3-6 are consistent with the features observed on sample surfaces as just have been explained. Track connectivity in the top layer of 240 W sample is significantly better than that in the top layer of 180 W sample, comparing Figure 3-6a to Figure 3-2. This is consistent with the much less intertrack gaps/valleys for the 240W sample observed on surface. There are 42 tracks in the top layer (L1) and $W_{Tk\text{-}L1}$ and h_{TK} (=P_{Tk}+R_{Tk}) of each were measured. For 180 W sample, $W_{Tk\text{-}L1}$ = 133.5±14.2 μm (mean and one standard deviation) and h_{Tk} = 60.0±9.1 μm, respectively. Note again that $\dot{\theta}$ = 20° for the top layer and, thus, *w* value projected on the cross section in the top layer (W_{L1}) is 125 μm / cos20°

= 133.0 μm, which is very close to the average $w_{Tk\text{-}L1}$ (133.5 μm). Increasing P from 180 W to 240 W increases the size to $w_{Tk\text{-}L1}$ = 150.7±10.7 μm and h_{TK} = 75.7±7.7 μm, based on the measurement of 42 tracks.

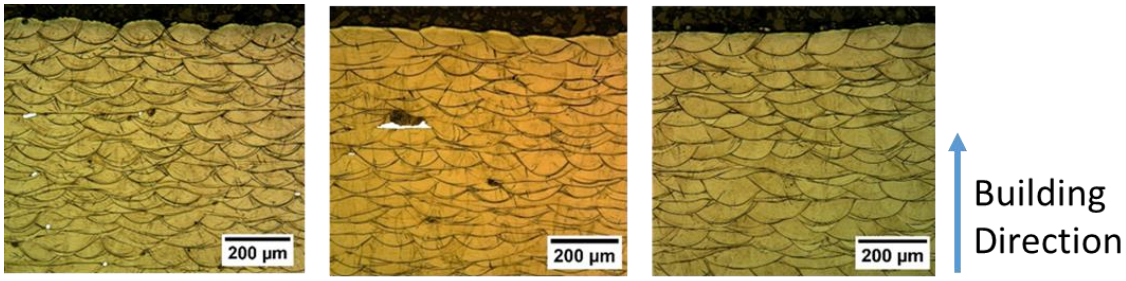

Figure 3-6 Optical micrographs of SLM samples made using (a) 240 W, (b) 280 W and (b) 360 W.

The measured values of tracks are now used to consider further geometrically how insufficient lapping relates to LOF. Tracks of the average sizes are laid track by track and layer by layer for the two (180 W and 240 W) SLM conditions. The track cross section in each layer has been made based on the tracks having rotated 67°. Then, for 180 W sample, on average $w_{Tk\text{-}L2}$ = 183.9 μm and w_{L2} = 183.3 μm. For 240 W sample, on average $w_{Tk\text{-}L2}$ = 207.4 μm and w_{L2} being the same value. This process has repeated 5 times and thus total 6 layers have been drawn in Figure 3-7. In drawing the figure, the shape of the track has followed the average trace of a number of tracks, taking $\gamma = 0°$. Also in drawing the schematics in Figure 3-7, the beginning of each layer starts with the edge of a track. This vertical location at the beginning is not realistic but the rest of the drawing should provide useful geometrical information on how track profile relates to complete fusion and track overlapping.

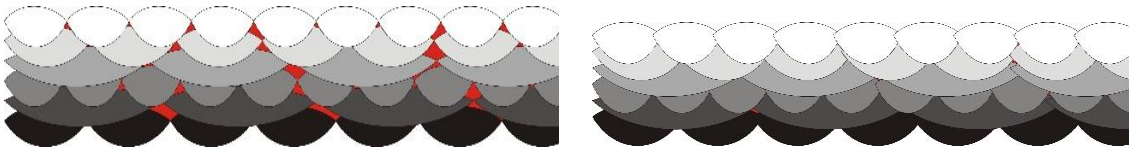

Figure 3-7 Schematic of laying/lapping track by track and layer by layer with a rotation of 67°after each layer using medium measured values of track width and depth and an approximate shape of tracks for (a) 180 W and (b) 240 W. LOF localities are in red.

Cleary, as illustrated in Fig. 3-7a, 180 W tracks are not sufficient in size and thus overlapping coverage is not complete, resulting in a large number of LOFs. Fig. 3-7a seems to show more LOF than in Figure 3-2a, thus is an overestimation on LOF. This may be reasonable, as in reality, a melt pool under laser may at least slightly infiltrate the empty spaces in its surrounding, thus, reducing LOF. As is illustrated in Figure 3-7, increasing *P* from 180 W to 240 W increases the average track size considerably. Due to this increase in track size, overlapping track by track and layer by layer is close to completion, leaving little LOF space, as seen in Figure 3-7b. Thus, based on Figure 3-2, Figure 3-6 and Figure 3-7, it can be expected that the *P* affected geometrical features of tracks should be the major factor relating to the amount of LOF.

Sizes of tracks made in the whole 180-360 W range are now examined. Measured values of R_{Tk}, P_{Tk}, R_{Tk}+P_{Tk} and W_{Tk} together with A_{Tk} are plotted in Figure 3-8. It should be pointed out that, as explained and illustrated in Figure 3-3c, W_{Tk} can only be approximately estimated as in most tracks one side is overlapped by next track. When W_{Tk} increases the portion of overlapping increases resulting in the estimation of W_{Tk} less certain. At *P* = 260 W, average value of measured W_{Tk} is 161.7 μm. Thus, the percentage of the average lapped distance (W_L) in a track is:

$$\frac{\bar{W}_l}{\overline{W_{tk}}} = \frac{\overline{W_{tk}} - W}{\frac{W}{2}} = \frac{\frac{161.7 - 125}{125}}{2} = 14.7\%$$

Using the method explained in Figure 3-3c introduces the uncertainty of measuring w_{Tk}, due to the uncertainty of measuring w_L. This may be viewed as a systematic error. It may be reasonable to assume that this uncertainty (Δw_L) should at most be 20% w_L. Then, on average:

$$\frac{\overline{\Delta W_l}}{\overline{wW_{tk}}} = \frac{20\%\overline{wW_l}}{\overline{W_{tk}}} = 20\% \times 14.7\% = 2.9\%$$

At P=360 W, average value of measured W_{Tk} is 192.0 μm, thus $\frac{\overline{\Delta W_l}}{\overline{W_{tk}}} = 5.4\%$. As has already been stated, the measured value of W_{Tk} is based on 42 tracks in each sample. The standard (random) error values are generally small. Increased overlapping causes more uncertainty of tracing the lapped portion of the track and thus of measuring A_{Tk}. Thus, for estimating A_{Tk} of a track, only half of the track on the lapping side was measured ($A_{Tk\text{-}m.}$) and A_{Tk} has been taken as $2A_{Tk\text{-}m.}$. In measuring $A_{Tk\text{-}m.}$ of a track, the half to be measured was manually traced and colored for Image J to measure the value.

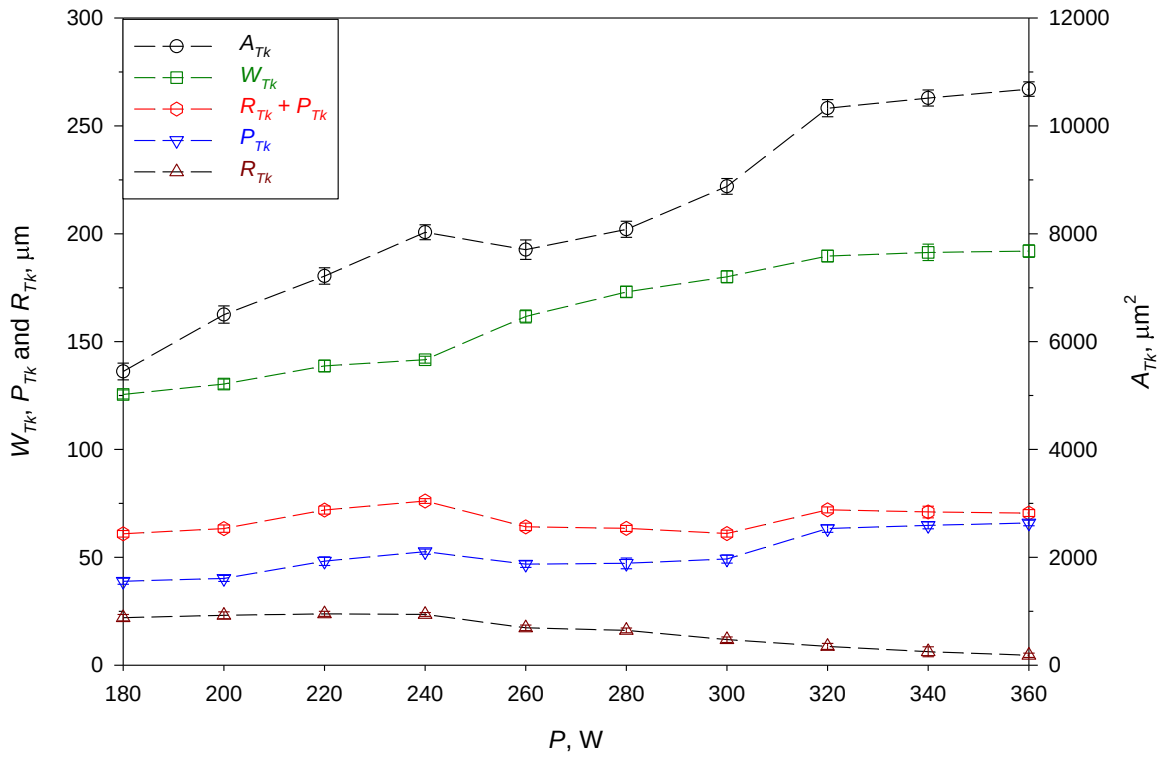

Figure 3-8 Track size data plotted verse laser power. Error bars are one standard errors.

Figure 3-8 shows that track size generally but not always increases as P increases. Data of R_{Tk} and P_{Tk} (and thus R_{Tk}+P_{Tk}) suggest that track shape varies as P increases. From 180 to 240 W, P_{Tk} and w_{Tk} increase as P increases but R_{Tk} varies little. This feature is consistent with the observation on the track cross sections in Figure 3-2 and Figure 3-6a where track sizes of the higher P sample can be seen larger than those of the lower P sample and for the penetration portions of the two different P value samples their shapes are similar. On the other hand, visually observing the two samples may suggest a similar height of reinforcement (consistent with the R_{Tk} values that vary little in the range of 180-240 W in Figure 3-8).

Data shown in Figure 3-8 show that, above 240 W, as P increases R_{Tk} clearly decreases. P_{Tk} reduces from 240 W to 260 W and remains lower until P > 300 W. P_{Tk} increases significantly when P increases from 300 W to 320 W but thereafter increases only slightly as P increases. These features of variations in track shape can be observed in Figure 3-6. Clearly, R_{Tk} of the 280 sample (Figure 3-6b) is significantly lower than that of the 240 W (Figure 3-6a) sample. Comparison of the same two top layers may also confirm the lower P_{Tk} value in the 280 sample than that in the 240 W sample. Observing Figure 3-6c suggests that little reinforcement (very low R_{Tk}) and strong penetration (high P_{Tk}) for the highest P (360 W) sample, as data in Figure 3-8 have also shown. A graphical representation of how increasing P affects the size and shape of track is shown in Figure 3-9. Each track profile represents approximately the track cross section of the respective P sample based on tracing the track edges of a number of tracks of the sample.

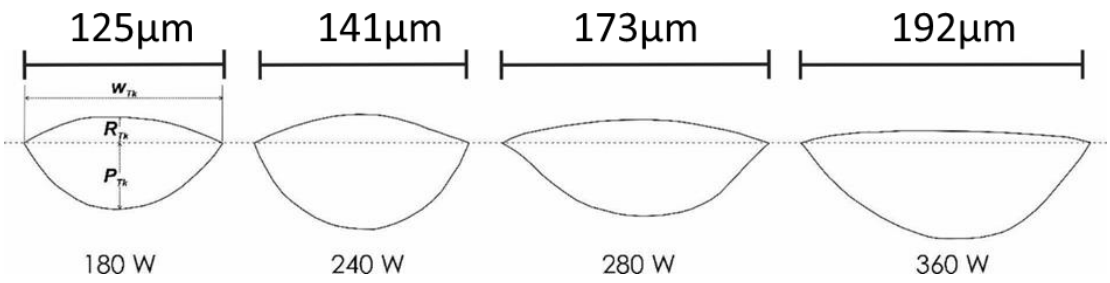

Figure 3-9 Representative outlines of track cross sections of top layers for 4 samples made using *P* values as indicated.

Geometrical features can be further explained from Figure 3-2, Figure 3-6, Figure 3-8 and Figure 3-9. First, as *P* increases from 180 W to 240 W, the penetration portion (w_{Tk} and P_{Tk}) increases in a proportional manner and there is little increase in R_{Tk}. This means that by increasing *P* and thus increasing heat input, the melt pool becomes larger, which is reasonable. Second, when *P* increases from 240 W to 260 W, there is a distinctive change in that W_{Tk} increases significantly but P_{Tk} decreases and R_{Tk} also starts to decrease. This second feature means that the track melt has significantly spread.

The higher degree of spreading and low penetration, as expressed by higher w_{Tk} and lowered P_{Tk}, continue to 300 W. The reduced P_{Tk} value from 240 W to 260 W correlates to the reduction in A_{Tk}. Third, a clear increase in P_{Tk} from 300 W to 320 W again also relates to the increase in A_{Tk}. From 320 W, the rate of increasing W_{Tk}, meaning dW_{Tk}/dP, becomes very low. The reason for this may relate to the laser spot size being 140 µm and thus W_{Tk} cannot keep increasing. From 320 W to 360 W, as *P* increases, dP_{Tk}/dP is positive but low. Also, dA_{Tk}/dP and W_{Tk}/dP values are low.

In other words, it is possible since the spot size is 140 µm when the laser melts the powder, the width of molten pool can become wider compared to a melt pool formed by a smaller laser spot for instance 70µm. However, in SLM using small spot size the laser is focused on small area and consequently the depth of penetration can become deeper than the depth of melt pool of 140 µm laser spot. This needs further investigation to clarify the effect of

laser spot on the melt pool shape and size. However, in this study the effect of spot size on the melt pool was not examined.

Furthermore, the geometry of melt pool is significantly affected by Marangoni or thermo-capillary convection which is driven by surface tension gradient. In an ideal situation, the thermo-capillary flow will be directed from a region with low surface tension (high temperature) to a region with high surface tension (low temperature). A melt pool with a higher maximum temperature rise, ΔT_{max}, will generally have a stronger temperature gradient thus consequently a stronger temperature Marangoni flow. [106]

Researchers have previously studied the surface tension of the Al-alloys, and it was experimentally and theoretically shown that increase in the operating temperature of the irradiated region lowers the surface tension [107, 108]. Mostly, the centre region exposed by the laser beam has the highest operating temperature while the edge of the melt pool has the minimum temperature. Consequently, in an ideal situation, because of the higher surface tension in the edge of the melt pool it is expected for melt flow to be dragged in the outward convection pattern. However, the shape of the melt pool of 180-240 W samples implies that the thermo-capillary flow inside these samples follows the inward convection pattern. The inward convection pattern could be the result of oxidation in the building chamber which has negatively affected the flow and melt pool spreading. It has been shown in the recent studies that oxide formation in the edge of the melt pool is significantly influenced by the presence of the oxygen in the building chamber of SLM machine [109, 110].

In order to have a better understanding of the effect of laser power on shape of melt pool, the change at thermo-capillary flow inside the melt pool at different laser powers is demonstrated in Figure 3-10. The operating temperature of the melt pool in the sample built using 180 W laser power is too low to destroy the oxidation film that exists in the edge of the melt pool, leading to the formation of inward convection pattern (Figure 3-

10a). The achieved heat from increasing the laser power to 240 W is still not high enough to eliminate the oxidation film, still the accumulated heat results in the increase of reinforcement and penetration depth (Figure 3-10b). When the heat is noticeably accrued in the melt pool by increasing the power to 280 W, the operating temperature has the capability to destroy the oxidation film in the edge of the melt pool, consequently gives rise to the formation of the outward convection power (Figure 3-10c). Further increasing the laser power to 360 W induces wider and deeper melt pool, and since the negative effect of oxide layer is no longer exist on the melt pool the reinforcement decreases significantly, inducing a good spreading and wettability (Figure 3-10d).

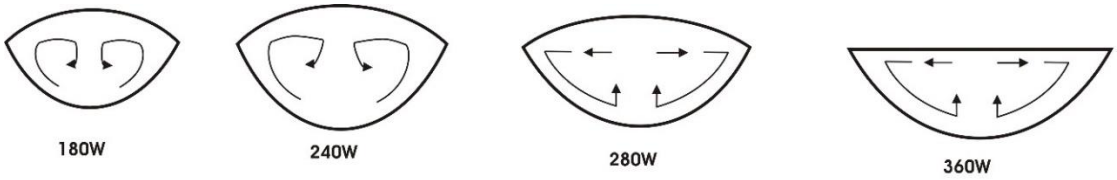

Figure 3-10 schematic of thermos-capillary convection flow using (a) 180 W, (b) 240 W, (c) 280 W and (d) 360 W laser powers.

The trend of how *P* affects the amount of LOF in the whole 180-360 W is now considered more closely. Measured (using Image J) values of LOF area fraction (f_{LOF}) are plotted against *P* in Figure 3-11 and each value is based on a measurement over 40 frames in an area of ~ 5.8 mm × 5.6 mm. The trend curve in Figure 3-11 clearly shows a rapid decrease in f_{LOF} when *P* value increases from 180 W to 220 W. In a practical sense, the use of 180 W is not very far but also not sufficiently close to the value for low f_{LOF} SLM parts. At or above 220 W, profiles (size and shape) of tracks are geometrically favorable so that melt track laying/lapping is sufficient to result in little gaps/space and thus a low amount of LOF ($f_{LOF} \approx 0.1\%$ or less). This is consistent with the observation that at 180 W (Figure 3-2 and Figure 3-7a) LOF is distributed all over the sample and at 240 W (Figure 3-6a and Figure 3-7b) there is little LOF.

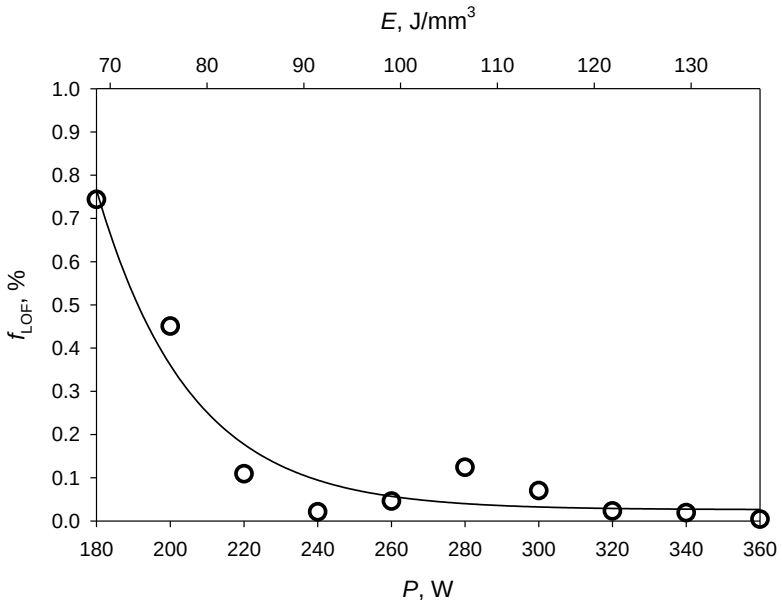

Figure 3-11 Area fraction of LOF determined using Image J plotted as a function of P and with a trend curve drawn. A second axis $E = P / (v \cdot w \cdot h) = P / (700\ \text{mm/s} \times 0.125\ \text{mm} \times 0.03\ \text{mm}) = P / 2.625\ \text{mm}^3/\text{s}$ is also added.

It should be noted that f_{LOF} = 0.1% represents a low value. This can be understood by briefly examining the recent studies by other researchers who had conducted extensive metallography measurements on SLM samples of various alloys. In Wei et al.'s [33] work on AZ91D Mg alloy, minimum porosity appears to be ~ 0.3%. As has been introduced (in Introduction), In Kamath et al's work [40] on 316L stainless steel, the minimum porosity was 0.19%. Kamath et al. did not present micrographs of their samples, but in a SLM study of 316L by Miranda et al. [111], it is clear from the many micrographs presented that intertrack LOF is the major cause for lowing density. As has also been introduced, the lowest porosity value at 0.1% was recently achieved in Sun et al.'s [41] study of the same stainless steel. In Qiu et al.'s [48] work on Invar (Fe-36Ni) alloy, porosity can be less than 0.1% but not zero towards the low end of scan speed range they used. Thus, a SLM sample with f_{LOF} = 0.1% can be regarded highly but not fully dense. The reason for why f_{LOF} values are not significantly lower than 0.1% when P > 220 W for some P values is explored below.

3.3 Further Examination on LOF

The 2D cross-sections from samples built with different laser powers and extracted along the building direction of the in-situ microtomography reconstructions are shown in Figure 3-12(a–d) from the tomography scan. These 2D cross-section images show evidence of LOF at multiple planes along the building direction.

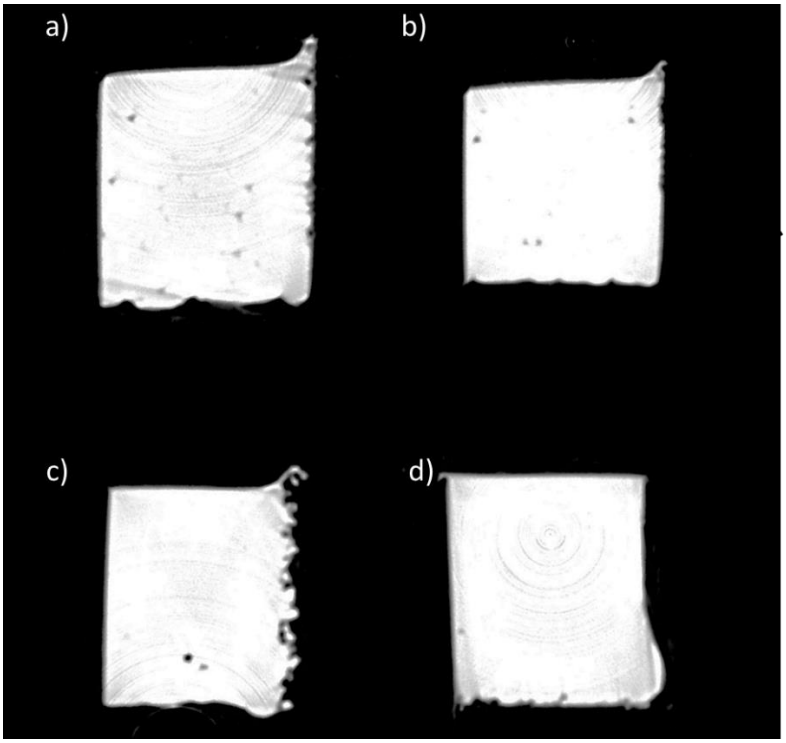

Figure 3-12 tomography scan of a) 180 W, b) 220 Wc) 280 W & d) 360 W samples

In Figure 3-13 the area fraction of LOF obtained from the synchrotron datasets shown in Figure 3-12 are compared to conventional 2D metallographic optical microscopy measurements of the LOF area. LOF area measurements for both techniques was done using ImageJ in which threshold was applied to the images to highlight the LOF area. With conventional optical technique only one cross section was analysed. In comparison with the synchrotron, evaluation is based on an average of batch of 2D slices and is a better representative of the LOF area of the sample.

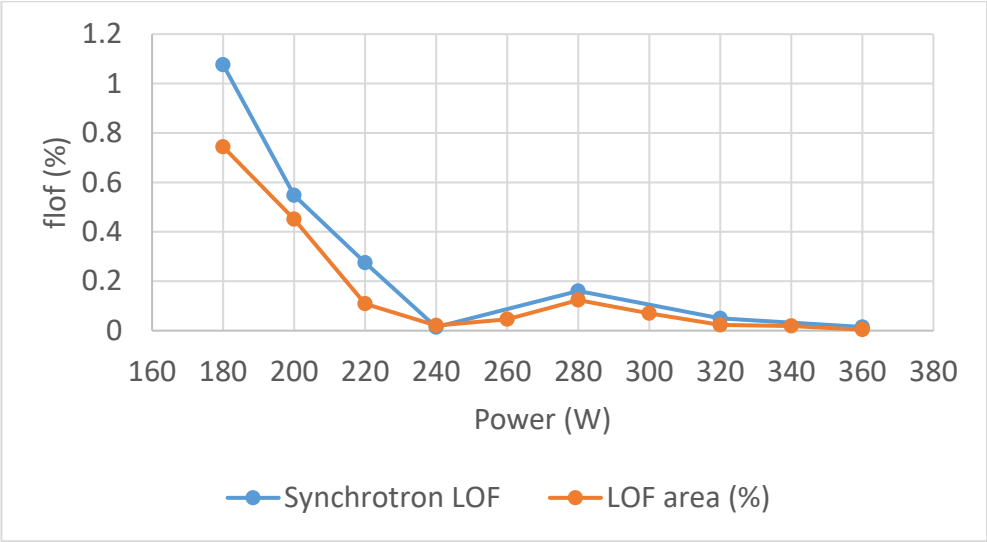

Figure 3-13 LOF fraction obtained from synchrotron and optical microscopy

At large sizes, LOFs were detected by both high-resolution synchrotron and optical microscopy to allow reliable statistical measurement. However, for LOFs smaller than 12 µm there was a reduction in the frequency in the synchrotron micrographs, compared to the optical micrograph measurements and synchrotron could not identify any LOFs below 6 µm in size. Therefore, below the resolution limit of the synchrotron micrographs there are a great number of small micro LOFs that would be missed with this technique. Another reason for the disagreement in the LOF fraction area detected using these two methods is likely to be due to the measurements in different regions of the build.

Overall, while the resolution of synchrotron data cannot detect small LOFs it has identified large LOFs in other layers of the build that will be crucial in terms of fatigue life and tensile elongation which were missed by the optical microscopy technique. The limitations in resolution and measurement region result in difference in LOF fraction area.

3.4 Spatter Particles and Their Effect on Formation of large LOF

The size range of LOF is now examined, focusing more on understanding the nature of the large size LOFs as briefly discussed in Section 3.1. Data of LOF sizes (A_{LOF}) are plotted in Figure 3-14 for samples of 180 W, 220 W and 340 W. They represent three

distinctive conditions shown in Figure 3-11. The first is low *P* and high f_{LOF} (>> 0.1%). The second is *P* having increased but still being low and f_{LOF} having considerably reduced (to close to 0.1%). The third is high *P* and very low LOF (f_{LOF} << 0.1%, but not zero). The sum of all individual values in each graph (Figure 3-14a, b or c) corresponds to the value in Figure 3-11 for 180, 220 or 340 W sample, respectively.

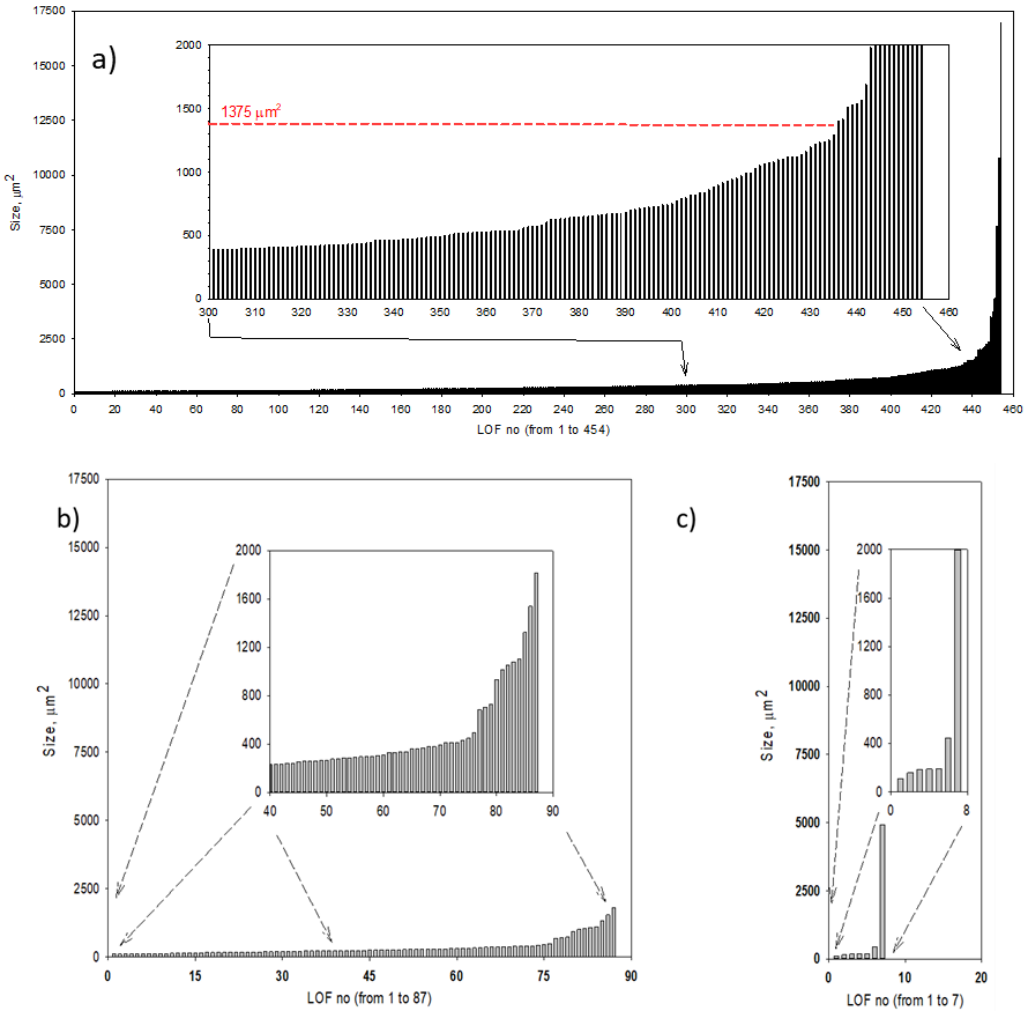

Figure 3-14 Measured size values of LOF in three samples made using, (a) P = 180 W, (b) P = 220 W and (c) P = 340 W.

As has been discussed and suggested, for 180 W, a LOF due to lack of overlapping as the result of insufficient track sizes should not be more than 25% of the average track size. As shown in Figure 3-8, $A_{Tk} \approx 5500$ µm^2 on average for 180 W. From Figure 3-2a, it can be suggested that the maximum LOF size ($A_{LOF\text{-}Max}$) may reach 25% of A_{Tk}. This is not a

precise prediction but is an indicative and reasonable value used for discussion. Then, normally, $A_{LOF\text{-}Max}$ should not be more than 25% × 5500 μm^2 = 1,375 μm^2. Thus, as is evident in Figure 3-14a showing A_{LOF} values of LOFs for the 180 W sample, most LOFs range from very small size (~ 100 μm^2) to a size comparable to $A_{Nor\text{-}LOF\text{-}Max}$ (1,375 μm^2). But there are also a number LOFs considerably larger, up to 12 times, in size than 1,375 μm^2. These large LOFs are regarded as abnormal LOFs. The possible cause of forming abnormal LOFs is considered below.

In Figure 3-4, melting of the powder layer has based on the sizes < 45 μm. However, as is clear in Figure 3-1 and Figure 3-5, "weld" spatters" are seen from very small to up to larger than 100 μm in diameter. Taking spatters into consideration, the illustration in Figure 3-4 has been redrawn and is given in Figure 3-15. It can be expected that spatters are a part of the powder layer after next layer powder spreading. As h = 30 μm, small spatters do not affect layer thickness, but a large size spatter should mean that locally thickness can be larger. Spatters can also land on top of the powders that are waiting to be melted and the net increase in local layer thickness is even larger. A large spatter stands high and energy from the laser beam would be insufficient to completely melt the spatter leaving LOF below the newly formed track. This is illustrated in Figure 3-15.

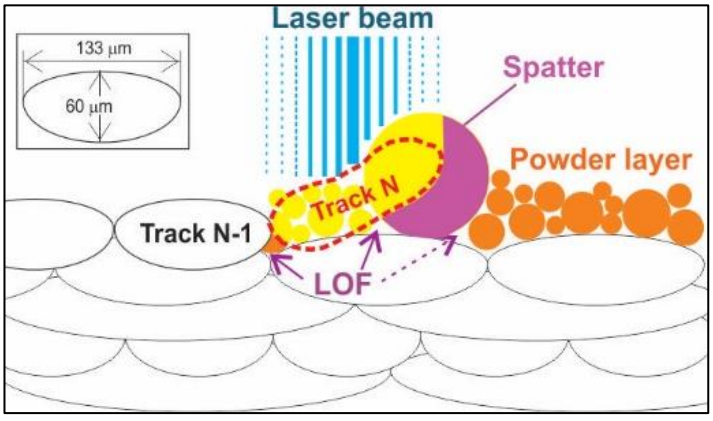

Figure 3-15 Schematic illustration of laser beam, powder layer with the portion (yellow) under the beam to melt and form track N and to form LOF, considering the presence of a spatter.

Two large spatter examples are shown in Figure 3-16, one ~100 μm and the other ~250 μm in size, considerably larger than the original particles (Fig.2-2a). For the large spatter shown in Figure 3-16b, it must have landed mainly on track n but also slightly on top of the powders of track n+1 before the laser beam spot reached that location of track n+1. Then, when the laser spot arrived at that location during track n+1 scanning, the beam melted the portion of the spatter on track n+1. The beam however must not be able to melt and penetrate to the original powders below the spatter and an abnormally large LOF should be expected below. In general, as explained in Figure 3-15, large spatters are potentially the spots for abnormal large LOFs. This is consistent with the example shown in Fig. 2-2b.

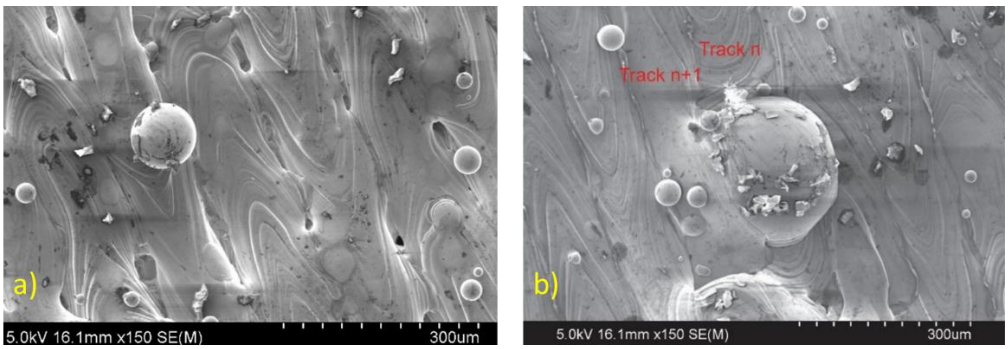

Figure 3-16 Examples of large spatters in (a) 180 W sample and (b) 240 W samples.

The morphology of spatters and powder particle was brought to attention by high magnification SEM images. As clearly showed in Figure 3-17 the initial powder particle and spatter have different morphologies. The morphology of powder particles presented in Figure 2-2a and Figure 3-17a shows spherical but with a very coarse microstructure. It should be noted not all the powder particles are perfectly spherical and some of them are deformed. The spatter in Figure 3-17b exhibited smooth spherical morphology and the solidification trace of liquid metal is evidently distinguishable, as can be seen in Figure 3-17c. Spatter particles is accompanied some small spots on the particle's surface. The spatter goes through a rapid cooling when it is getting away from the laser radiation region. Since there is no movement of melt due to surface tension effect before the spatter

splashing on the powder, it results in smooth surface and near perfect spherical shape. Also, the high cooling rate of solidification process gives rise to formation of fine cellular-dendritic microstructure.

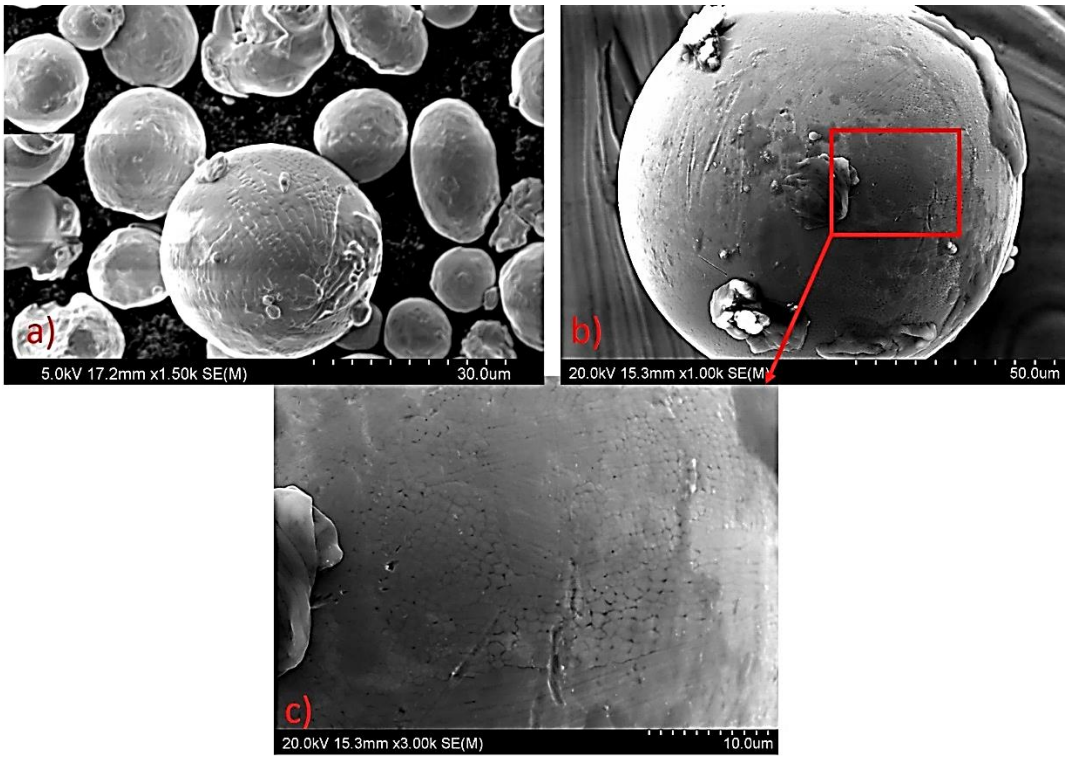

Figure 3-17 SEM images of initial powders and spatter, a) morphology of powder particles, b) morphology of spatter and c) high magnification of the spatter surface from image b.

Compared Figure 3-14b to Figure 3-14a, increasing P from 180 W to 220 W has considerably reduced the total number of LOFs from 454 to 87 and $A_{Nor\text{-}LOF\text{-}Max}$ from ~ 1,370 µm^2 to ~ 400 µm^2 as observed in the graphs, although there are a few larger (than 400 µm^2) LOFs. Thus, f_{LOF} reduced considerably from 0.75% to ~ 0.1. As shown in Figure 3-8 and Figure 3-11, when P increases from 300 W to 320 W and above, P_{Tk} has increased from < 50 µm to > 60 µm and f_{LOF} values have become very low (≤ 0.02). This is reasonable, as a high P_{Tk} capability condition is more effective in melting the spatters. Note that even when P = 340 W, as shown in Figure 3-14c, a large LOF could still be

detected in a cross section, meaning that large spatters may not be completely melted and thus $f_{LOF} \neq 0$.

In 2016, Mukherjee et al. [112] introduced an index called LOF index and it is defined as the ratio of penetration over layer thickness. They explain that LOF index signifies the degree of penetration for bonding properly the previous layer. They plot porosity values of various SLM metals available from literature as a function of LOF index predicted by their simulation and the plot suggests a linear relationship. The minimum level of porosity in the plot is ~ 1%. This value, in comparison to the f_{LOF} values of the present work, is a high value. It should be noted that LOF index should only be physically meaningful for porosity in the form of LOF. Values of f_{LOF} from the presented work have been plotted as a function of P_{Tk}/h and is given Figure 3-18. Clearly, f_{LOF}-P_{Tk}/h is not a linear relationship. As the results in the present work have indicated, geometrically, not only P_{Tk} (or P_{Tk}/h) but also W_{Tk} (or W_{Tk}/w) is important for proper bonding and for minimizing LOFs of the normal form.

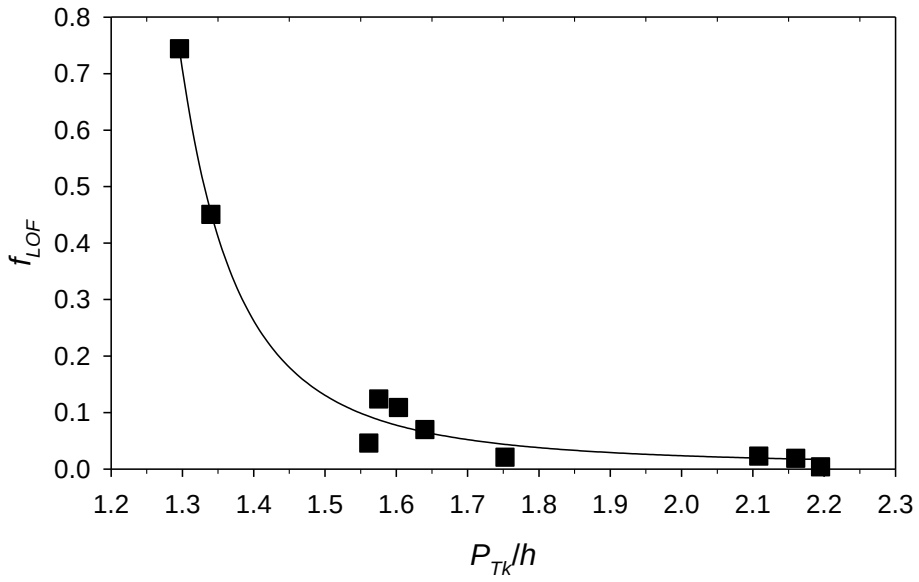

Figure 3-18 Area fraction of LOF plotted as a function of the ratio of penetration over layer thickness.

However, for reducing the effect of spatters on forming the abnormal LOFs, P_{Tk} (or P_{Tk}/h) plays a more dominant role. This has already been explained but plotting f_{LOF} values verse P_{Tk}/h as shown in Figure 3-18 may further illustrate. As have been presented and discussed, f_{LOF} values in the present work is from just under 0.8% to close to zero. In Figure 3-18, the rapid decay of f_{LOF} as P_{Tk}/h increases from 1.3 to 1.4 which is also associated with increasing W_{Tk} is due to the increase in track size to a sufficiently large value to eliminate normal LOFs. Spatters induced LOFs require very high P_{Tk}/h values to be completely eliminated. In Figure 3-18, for $P_{Tk}/h > \sim 1.5$, data and trend curve shows $|\Delta f_{LOF}/\Delta(P_{Tk}/h)|$ is low, meaning that there needs a large increase in P_{Tk}/h for a small decrease in f_{LOF}. This is consistent with the suggestion already made that a large spatter cannot be readily and fully melted even at a very high P value.

3.5 Melt Pool Size and Laser Power

Figure 3-19 shows the SEM micrographs from top surface of 180 W, 220 W 280 W, 320 W & 360 W cubic samples. Valleys between scan tracks that leads to formation of LOF and, spatter on the powder bed have been discussed before. Black marks that are due to the contamination of the surface can be seen on the surface of samples. Also, there are narrow visible tracks, indicated with red arrows, on the micrographs, consisted of small shallow melt pools above the main scan tracks. The presence of these tracks is because of the default build system of the machine that does a final scanning with laser power of 5 W on top of the built sample. This default build condition could not be altered or omitted from the process and, there is no explanation by Renishaw for this final laser scanning.

In all surfaces, tear-drop shaped solidified melt pools can be identified. The tail part of the melt pool, as indicated in Figure 3-19 as l_{pool} can be estimated. The l_{pool} is measured using the visible track boundary of the melt as shown in the SEM micrograph of the 220 W sample in Figure 3-19 and is plotted as a function of laser power in Figure 3-20a. The

length of melt increases with increase of laser power as opposed to the depth of melt pool. The scaling law is between $\frac{l_{pool}}{P}$ and power density $E_v = P/v$ as shown in Figure 3-20b.

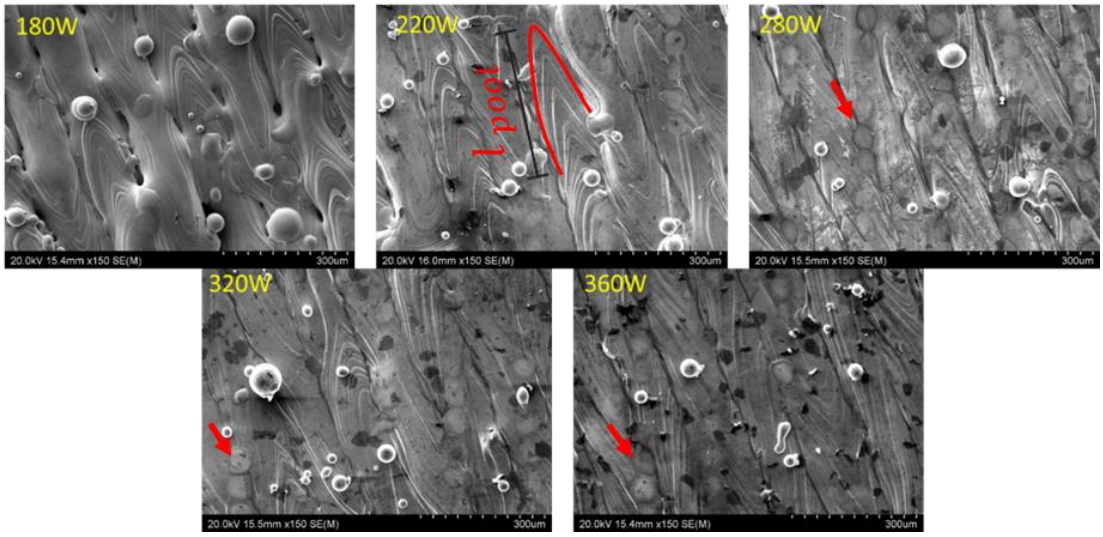

Figure 3-19 SEM micrographs from top surface of 180 W, 220 W 280 W, 320 W & 360W samples

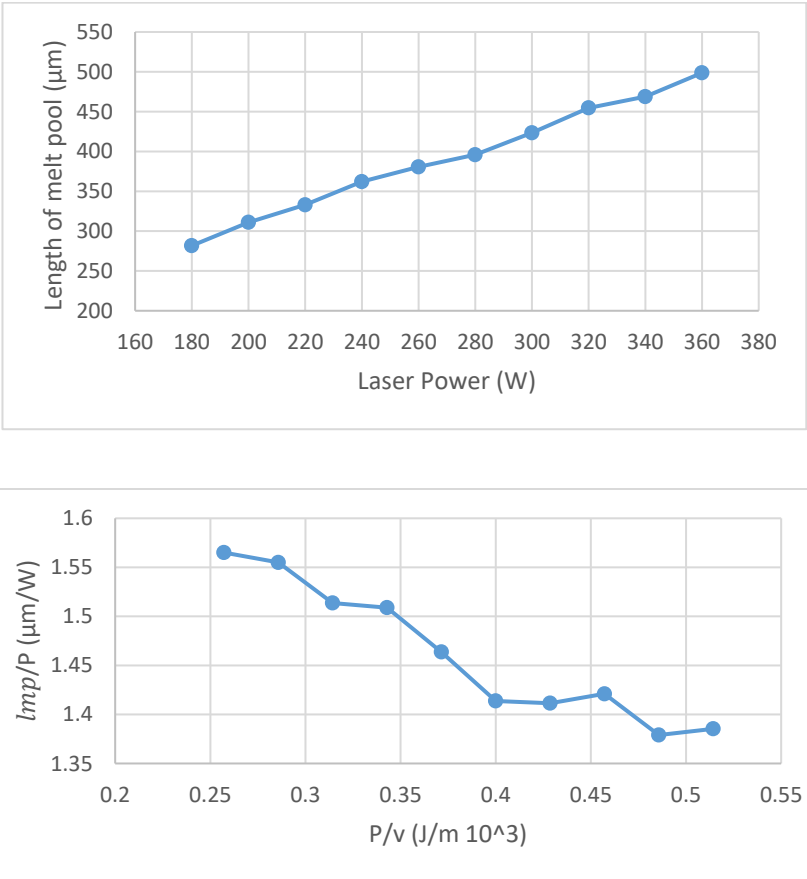

Figure 3-20 Correlation between a) melt pool length as a function laser *P* b) *L/P* Vs *P/v* using CoCrMo alloy and powers from 180 W to 360 W

The relation between melt pool length and laser power was proposed by Lu et al. [113] using the equation as below:

$$l_{mp} \approx \frac{D \cdot P \cdot E_v}{\pi K_{tc}^2 (\Delta T)^2} \qquad \text{Equation 3-1}$$

where, D and K_{tc} are the thermal diffusivity and thermal conductivity, respectively, P is the power of the point source, ΔT is the difference between melting point and preheating temperature, $\Delta T = T_m - T_{pre}$, and power density $E_v = P/v$.

Based on equation 3-1 melt pool length is proportional to the product of power and power density which is consistent with experimentally measured relationship between laser power and length of melt pool in our experiment. However, the length over power value has an inverse proportional relationship with the power density in our experiment which is contradictory with the results of Lu et al.'s simulation and analytical study. It is possible that their simulation and analytical calculations are not a highly reliable measure for identifying the relationship between l_{mp}/P and power density.

As observed in the cross-section images shown in Figure 3-2 and Figure 3-6 the melting mode in our samples built with different laser power is conduction. Two common melting modes in laser melting are conduction and keyhole [114]. In conduction mode sufficient energy is delivered to melt the material and in keyhole mode the energy is sufficient to vaporize the material. The schematic drawing of conduction and keyhole melting modes are given in Figure 3-21. Keyhole melting has been observed in more studies than conduction melting. In SLM, if the energy input is high enough, the maximum temperature in the melt pool (T_{max}) can reach the boiling point of the material. This is followed by the vaporization of some of the material from the melt pool which results into a dense vapor plume above the melt that produces recoil momentum on the molten material to form a cavity [115, 116]. The complex physics of how vaporization and recoil pressure applied by the vapor on the melt pool to result in formation of keyhole melting

has recently been studied by Khairallah et al. [117] If energy input is low the peak temperature will be less than the boiling point, so the material is locally melted without a significant vaporization. Thus, heat transport is mediated via conduction and convention within melt pool, which is represented as conduction mode.

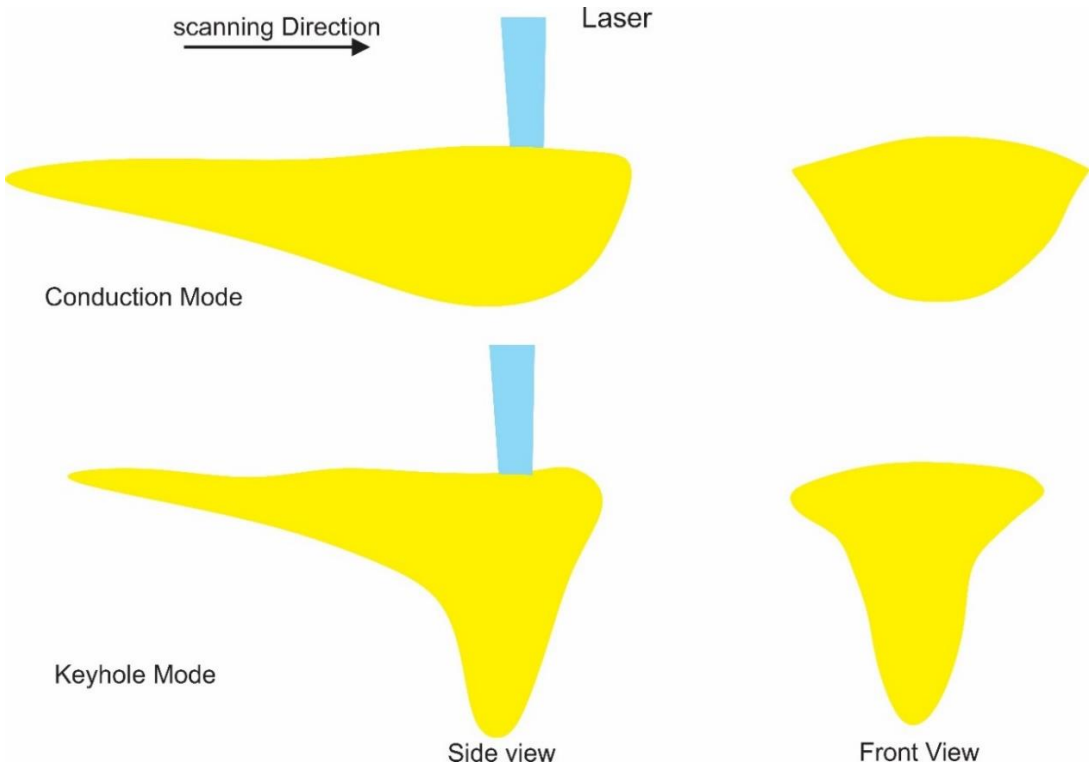

Figure 3-21 schematic drawing of conduction and keyhole melting modes

In the current study, formed melt pools have largely semi-cylindrical shaped where the re-melting depth is usually less than or equal to double the height of layer thickness. Thus, during the SLM process using conduction melting, every layer is re-melted approximately once. In keyhole melting which was observed in Bertoli's study[116], the delivered input energy to the powder bed is high. The melt pool assumes the shape of a keyhole in this condition and the depth/width ratio of melt pool becomes significantly higher than one, with depth of penetration into the previous layers reaching depth that can be as high as ten time the single layer thickness.

In this work, increasing laser power from 180 W to 360 W changed the size of melt pool, however, did not change the mode of melting. Thus, there was no significant change in

the shape of the melt pool. The melt pool depth in all the built samples only re-melted one layer and did not exceed multiple layers. Also, the depth to width ratio in samples was less than one for all the builds. As was discussed before it is possible that this is due to the width of the laser spot. If the laser spot was smaller the width of melt pool would have been smaller, and depth of penetration would have been higher which leads to keyhole mode melting.

Also, the consistent conduction melting could be due to the low used energy input which did not reach the boiling temperature of the material. Although laser power was doubled (from 180 W to 360 W) but clearly it was not sufficient to initiate significant vaporization of the material. Effect of SLM processing parameters on the threshold of keyhole mode can be explained as below:

During SLM, the heat flux of laser beam can practically be treated as continuous and can be shown as gaussian distribution. For a gaussian beam with size of *d*, the maximum temperature (T_{max}) in the centre of the beam and, the average heat flux density (q) can be expressed using the [118]:

$$q = \frac{0.865\ddot{\alpha}P}{\pi d^2} \qquad \text{Equation 3-2}$$

where $\ddot{\alpha}$ is the absorptivity coefficient of material. The interaction time of the laser scan (t) with the speed of v is:

$$t = {}^{d}/_{v} \qquad \text{Equation 3-3}$$

Taking the layer thickness (h) into account, the energy per unit volume (E_v) during the laser radiation on powder particles is:

$$E_v = {}^{qt}/_{h} = \frac{0.865\ddot{\alpha}Pt}{\pi d^2 h} \qquad \text{Equation 3-4}$$

Therefore, the modified specific enthalpy is rewritten as:

$$\Delta H = \frac{0.865\ddot{\alpha}P}{\pi dhv} \qquad \text{Equation 3-5}$$

The modified normalized enthalpy can be obtained based on the calibration [119].

$$\Delta H/h_s = \frac{0.865\ddot{\alpha}PD}{K_{tc}T_m\sqrt{\pi dhv}} \geq \frac{\pi T_b}{T_m} \qquad \text{Equation 3-6}$$

The equation can be rephrased as follows:

$$\frac{P}{dhv} \geq \frac{K_{tc}T_b\sqrt{\pi^3}}{0.865\ddot{\alpha}D} \qquad \text{Equation 3-7}$$

This equation indicates that the modified threshold for keyhole mode mainly depends on laser power, scanning speed, layer thickness and beam size. In order to clarify the cause for the absence of keyhole mode melting, Figure 3-22 using equation 3-6 under various laser powers gives the modified enthalpy. Thermophysical parameters used for the calculation are given in Table 3-1. It is obvious from the figure that the modified equation can well fit with the experimental results, which can be used to predict the melt pool mode in SLM. The energy of the built samples is well below the threshold for formation of keyhole mode, even the increase in laser power is not adequate for formation of keyhole melting. Thus, in this study the shape of the melt pool does not change under the influence of laser power.

Table 3-1 Thermophysical parameters of CoCr alloy for the modified normalized enthalpy calculation [120]

Boiling point, T_b (K)	3000
Melting point, T_m (K)	1600
Absorption coefficient, $\ddot{\alpha}$	0.3
Thermal conductivity, k_{tc} (W m^{-1} K^{-1})	12.1
Thermal diffusivity, D (m^2 s^{-1})	3.4×10^{-6}

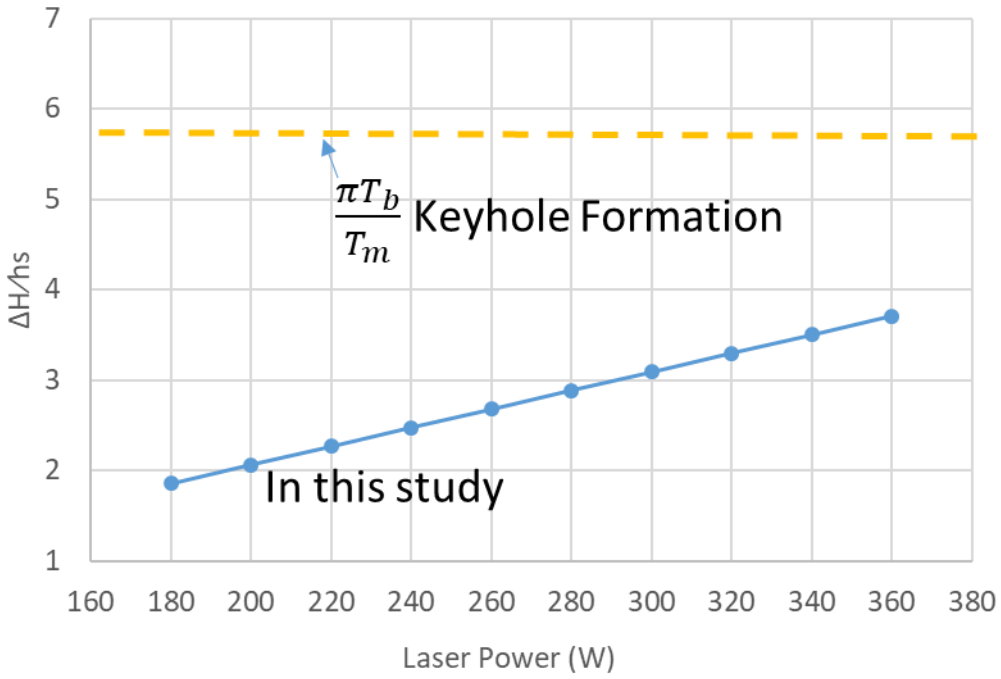

Figure 3-22 Modified normalized enthalpies of CoCrMo using laser powers

3.6 Summary

Selective laser melting (SLM) of CoCrMo (F75) alloy using the recommended SLM parameters of power (= 180 W), scan velocity, scan spacing, and layer thickness has resulted in tracks that were insufficient in size. This in turn has resulted in insufficient overlapping and thus the area fraction of lack of fusion (f_{LOF}) has been found to be considerably higher than 0.1%. Inconsistency in the size and irregular track appearance observed have suggested insufficient stability of the size of the melt pool during SLM. Size inconsistencies and track irregularity have further prevented sufficient overlaying and overlapping. Increasing P from 180 to 220 W, while other parameters remained the same, has decreased rapidly f_{LOF} to 0.1% due to the increase in the average size of the tracks for sufficient track overlapping. The increase in P has improved melt/track stability and track overlapping consistency during SLM but the further reduction of f_{LOF} was not proportional to the increase in P value. It was found that, above 240 W, reinforcement (R_{Tk}) decreased almost linearly and width of track (w_{Tk}) increased with a decreasing rate as P increased. However, over the range of 260 W to 300 W, penetration (P_{Tk}) values were lower than those of 240 W and of > 320 W. Measurements and observations presented in this work indicate that a high P_{Tk} value is the determining factor for overcoming the effect of large size spatters on forming large size LOFs and for f_{LOF} to be $\ll$ 0.1%. The difference between the morphology of the powder particle and spatter on powder bed is the formation of fine cellular- dendritic microstructure in spatter but the powder particle has a very coarse microstructure with deformation. Also, the results of LOF fraction area from synchrotron data confirmed the results obtained from optical micrograph measurement. The laser melting mode did not change by increasing the laser power and was conduction mode in all samples. The reason for this consistent melting mode behaviour could be due to the large spot size (140 µm) or low laser energy density which led to low depth of penetration of the melt pool.

4 Grain Growth, Intercellular Spacing and the Related Thermal Condition

The results and observations from the extensive study on solidification microstructure of samples built using different powers are presented in this chapter. SEM observation on the solidification microstructure and grain growth is presented first. Followed by discussion and analysis on the mode of solidification and grain growth. Results of the relationship between the growth angle and cell size and, the laser power and cell size are presented. Furthermore, the thermal condition in the melt pool and effect of it on the cell size are given. Finally, a comparison between the thermal condition in the SLM process and conventional solidification processes is presented.

4.1 Solidification Microstructures and Crystallographic Directions of Cells

A low-magnification SEM micrograph of 180W sample is shown in Figure 4-1. Typical features of SLM tracks laying one by one to form a layer and layers built one after another are clear. To present the observed solidification microstructures in detail, high-magnification SEM images in various locations of a complete track are taken, and these locations are shown in Figure 4-1. The various locations include track boundary (a–e), midtrack (mid) area and top region of track (T1 to T3). Complete tracks are only those top layer tracks of a SLM sample, as tracks in any other layers have been partially remelted.

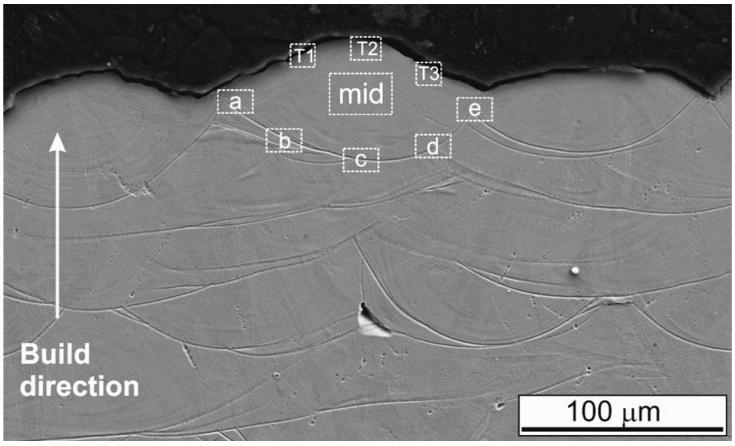

Figure 4-1 SEM micrograph of a sample cross section showing typical SLM tracks with locations indicated for a top layer track to be examined at high magnifications.

High-magnification SEM micrographs taken along a track boundary are shown in Figure 4-2. They suggest that the solidification mode during SLM was cellular, resulting in fully cellular structure. However, directions of cells (along the length of cells) are clearly not consistent and may or may not change crossing the track boundary. Cell sizes (widths) range from <0.5 μm to up to 1 μm. In the micrographs, red arrows indicate grain growth directions projected on the micrograph plane. As has been explained and indicated in Figure 2-12, for low ω values, the projected growth directions are difficult to identify. Thus, red circles are used to indicate low ω value cells. Each arrow points to the growth direction of an individual grain (projected on the 2D micrograph plane) and a grain contains many cells with the same growth direction. A grain boundary is where one group of cells and therefore one grain meets another.

Along the track boundary, as shown in Figure 4-2(a–e), it is clear that cells have grown directly from melt/track boundary, and there is no evidence of planar growth. In those grains marked with the arrow starting from the previous track crossing the boundary to the top layer track, cellular growth has continued in the same direction. In two locations, one on the left of Figure 4-2a and the other being the lower left of Figure 4-2e, growth directions have clearly changed by 90°. In other locations, as shown in Figure 4-2c and d, growth directions have changed, although the angles cannot be certain. Cells with width (ω_c)>0.5 μm are normally displayed clearly and finer cells with ω_c<0.5 μm are less clear but identifiable. As is clear in Figure 4-2b, cell sizes have changed considerably crossing the track boundary. This change is also recognized in Figure 4-2a, but in other locations (Figure 4-2c to Figure 4-2e), the changes are not large. Most grains along the boundary in Figure 4-2 did not grow normal to the melt boundary. The highest projected (on micrograph plane) angle in the micrographs is 40° and is shown in Figure 4-2e.

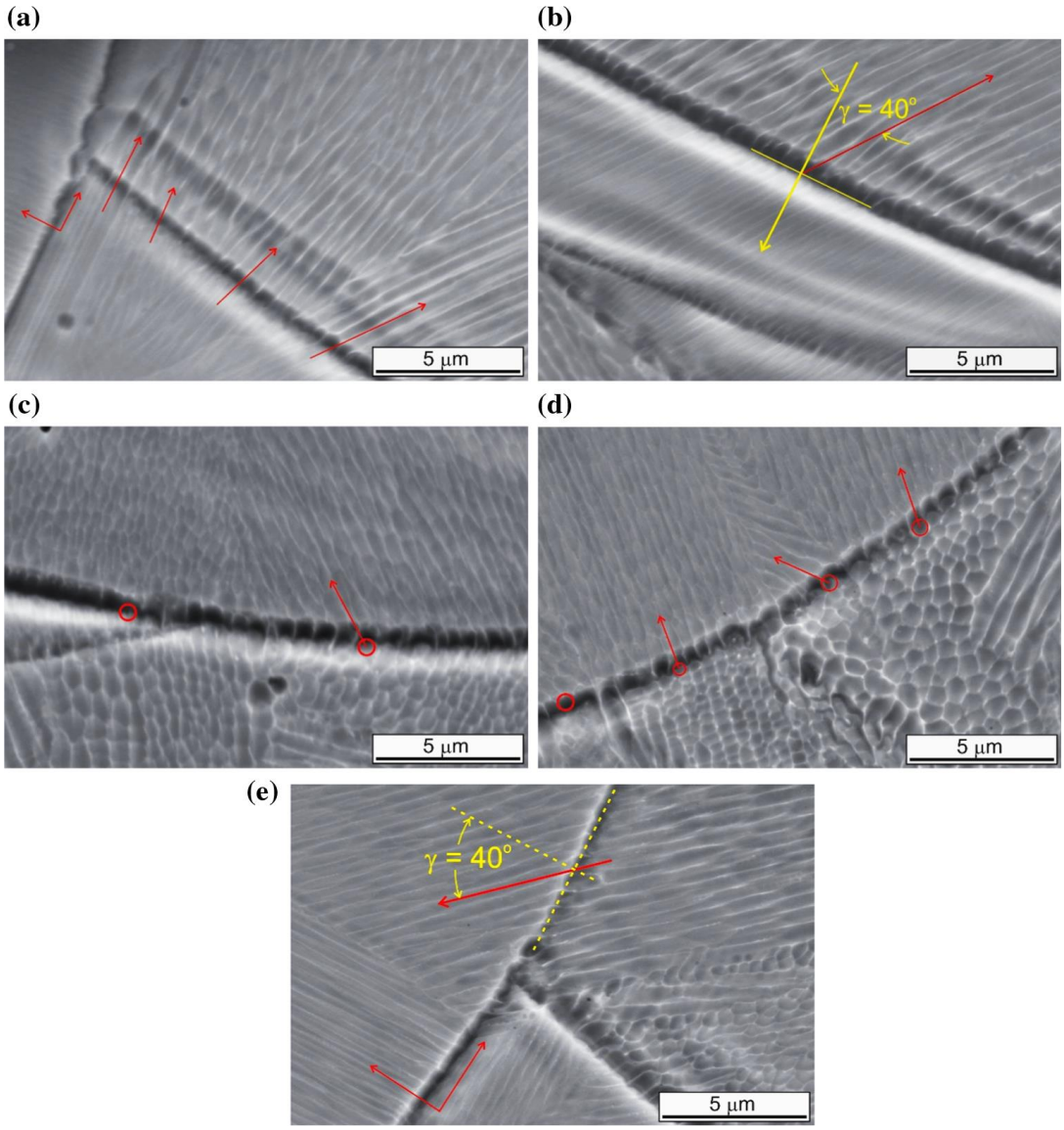

Figure 4-2 High-magnification SEM micrographs taken in various locations along the track boundary, a–e for location a to location e in Figure 4-1, respectively. Cell growth directions projected on the micrograph plane from one side of melt boundary to the other are indicated by arrows.

After the initial (epitaxial) growth starting from the melt boundary, inside the track each grain (group of cells) grows continuing the same growth direction. Growth is, however, competitive. Some grains have stopped growing after impinging on another, depending on the angle between the growth direction of the grain and the temperature gradient direction. A high value angle, indicative as one projected in the metallography plane (γ) in Figure 4-2e, readily stops. Growth termination is shown in Figure 4-3 in the two grains marked with red arrows. The lower left (in Figure 4-3) is grown from the grain shown in

Figure 4-2b, and the upper right (in Figure 4-3) is one from the bottom grain in Figure 4-2e. These two grains stopped growing after impinging on grains that were growing in a more favourable heat conduction direction toward the central top of the track. Micrographs shown in Figure 4-4 reveal that cellular growth continued to the top of track, without forming equiaxed dendrites in the final solidification location.

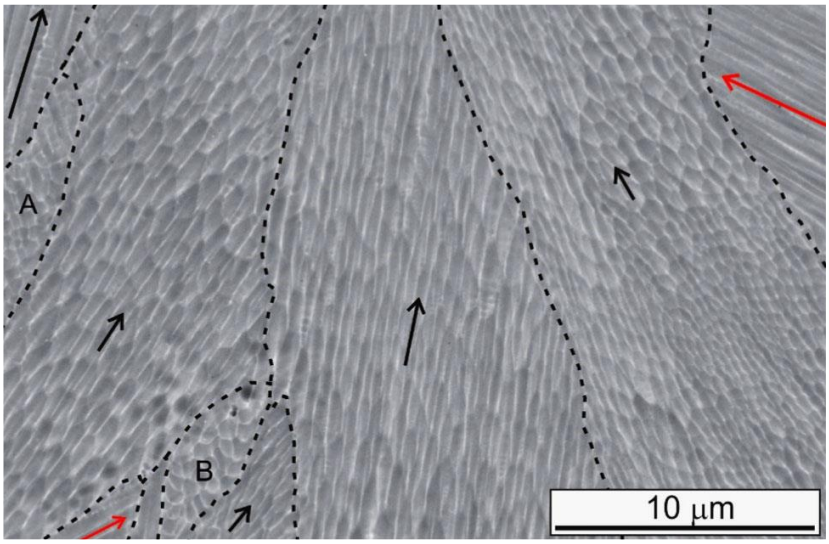

Figure 4-3 High-magnification SEM micrograph taken in area marked "mid" in Figure 4-1. Projected growth directions are indicated by arrows, except for grains A and B. Dotted traces indicate columnar grain boundaries. The lower left grain and the upper right grain with red arrows are the same grain as the upper right grain in Figure 4-2b and lower left grain in Figure 4-2e, respectively.

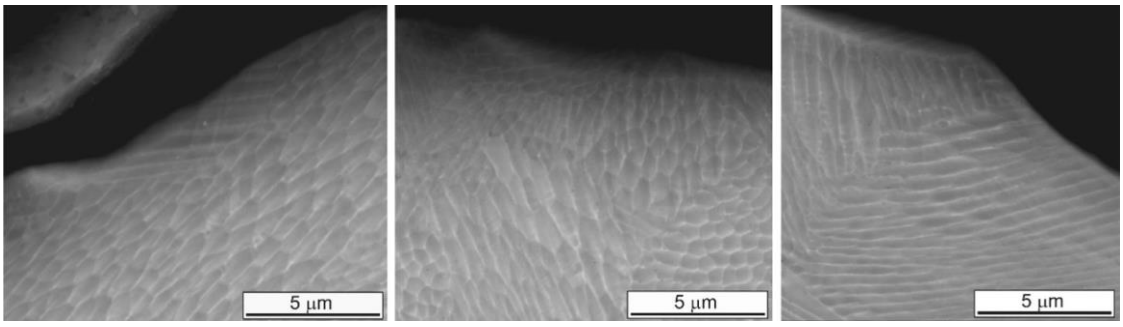

Figure 4-4 High-magnification SEM micrographs, left, mid and right taken in locations marked T1, T2 and T3 in Figure 4-1, respectively.

To better understand cell growth directions that should relate to heat flow direction during solidification, an EBSD orientation map of the 180W sample for the area shown in the

low-magnification SEM micrograph in Figure 4-5a is presented in Figure 4-5b. The macro-features of tracks in Figure 4-5a are largely the same as those shown in Figure 4-1. During SLM of Co–Cr–Mo alloy, Co-rich γ-fcc phase solidifies as the primary phase with σ Mo-richer second (Ɛ) phase solidifying along the cell boundaries. Furthermore, in SLM as-built state, γ-fcc phase largely remains although X-ray diffraction analysis has shown the existence of Ɛ-hcp phase, indicating a small amount of γ-fcc to Ɛ-hcp transformation. Since grain growth during solidification of the primary phase is the focus of the study, Co γ-fcc orientation map in Figure 4-5b is suitable, without the need to identify the small amounts of Ɛ and σ phases. The track boundaries in Figure 4-5a have been traced and superimposed onto the orientation map in Figure 4-5b.

Regions (rectangular) marked a, b and c in Figure 4-5a are also outlined in Figure 4-5b. Two features of crystal growth are clear in Figure 4-5b. First, locally crossing the track boundary, the same grain (with same color) having grown across the boundary into the new track is always the case. This, as has been well known, is epitaxial growth. However, information on whether it is the same <100> growth direction associated with the epitaxial growth is not provided in the map. Second, it appears that grains (i) grow across multiple layers in columnar (elongated) or in an irregular and blocky form or (ii) terminate after growing into the new track. Unit cells for each grain, before and after track boundaries, in locations a to c in Figure 4-5a are shown in Figure 4-6.

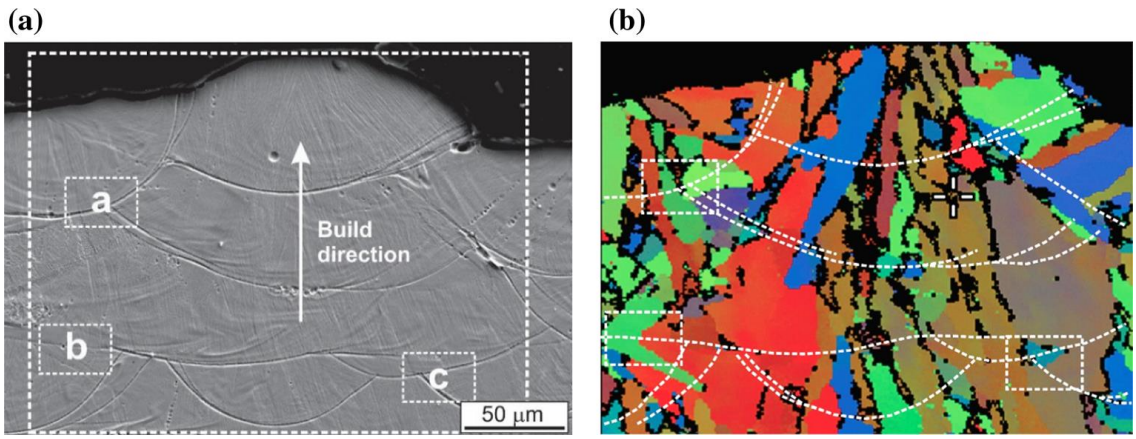

Figure 4-5 a) SEM micrograph of cross section of 180 W sample as illustrated in Figure 2-3 and b) EBSD orientation map with track boundaries outlined.

The angle (Θ) between the growth directions of cells for each grain grown from the track boundary to the normal direction of track boundary is provided for each grain except grain 4. Also, as an example, a group of cells before and after track boundary are indicated for grain 3 in Figure 4-6a, with the cellular structures projected on the micrograph plane appearing consistent with the cells of the grain in the micrograph. For all other grains in Figure 4-6, except grain 4 in Figure 4-6a, crystal unit cells and growth orientations are given. EBSD quality for grain 4 in Figure 4-6a is poor, and thus, no information can be interpreted.

Unit cells determined and shown in Figure 4-6 have further demonstrated that a unit cell orientation is always the same in the grain before and after the track boundary, and the growth is thus epitaxial. Unit cell information and cellular structure in each grain in these micrographs have confirmed that growth directions readily change by 90°, dominant in these micrographs (Figure 4-6), although from the orientation map this information cannot be gained. For example, grains 1, 2 and 3 in Figure 4-6a are grains changing by right angles in SEM images but appear in the orientation map (Figure 4-5b) as columnar grains. Grain 5 in Figure 4-6a is clearly a grain changed by right angles in the SEM image and appears blocky in the orientation map in Figure 4-5b. Grain 2 and grain 4 in Figure 4-6c are the same grain, having changed 90° twice after crossing two track boundaries,

thus appearing in orientation map as a large and irregular grain. Other grains can take various irregular shapes in the orientation map as the result of the combined changes at right angles.

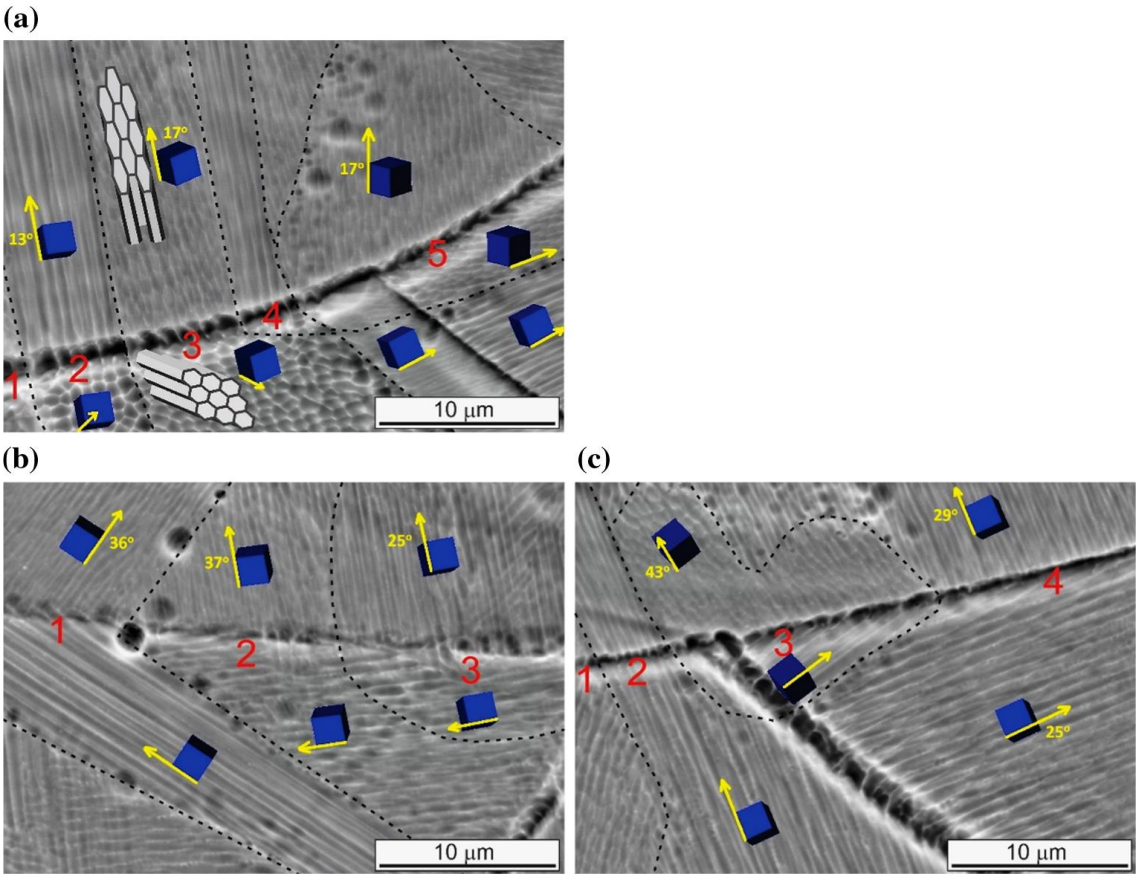

Figure 4-6 High-magnification images: a–c for locations marked a, b and c in Figure 4-5, respectively. Dotted lines represent grain boundaries. Unit cells with growth directions are indicated. Values of Θ for each grain are given. Schematics of grown cells with 2D projected cells on metallography plane are presented for grain 3.

Figure 4-7 shows the top surface of the sample normal to the building direction. As was expected from the cells growing towards the top in the cross-section observation, a cellular microstructure is detected. According to the Co-Cr-Mo ternary phase diagram [121], the Ɛ-Co hcp phase forms only when the Cr content is less than 37.6 wt%. In the CoCrMo alloy, the Cr content is in the range of 26 and 30 wt% and due to the lack of austenitic stabilizers like ‘C’, together with the high cooling rates reached during the SLM process, leads to the formation and stabilization of the Ɛ -Co phase [63].

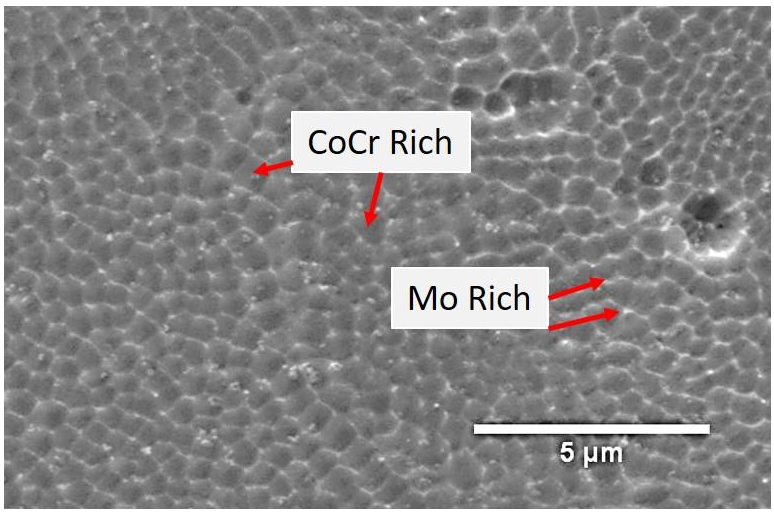

Figure 4-7 SEM micrograph of top surface of 180W sample

Furthermore, the ternary phase diagram in Figure 4-8 shows the possibility for the formation of a $Co_{49}Cr_{21}Mo_{30}$ phase (R' phase on ternary graph). Nonetheless, the amount of Mo in the CoCrMo system is < 7 wt%, which is not sufficient for the formation of the $Co_{49}Cr_{21}Mo_{30}$ phase. Thus, the CoCrMo system can be considered as a pseudo-binary system, with CoCr and Mo as the two phases (even though three elements Co, Cr and Mo are present). As a pseudo-binary system, the solubility of Mo in the CoCr phase is almost negligible and hence, the CoCr phase forms from the melt and ejects Mo since the formation of the $Co_{49}Cr_{21}Mo_{30}$ phase is not favourable. In the CoCrMo alloy, the solidification range of CoCr is ~1450 C° and Mo has a melting point of 2623 C°. These properties favour the solidification of the low melting phase in the first step by ejecting the high melting solute at the solid-liquid interface and the low melting phase will form the core of the cells. The high melting phase solidifies then subsequently and surrounds the cell cores, thus forming the cell boundaries.

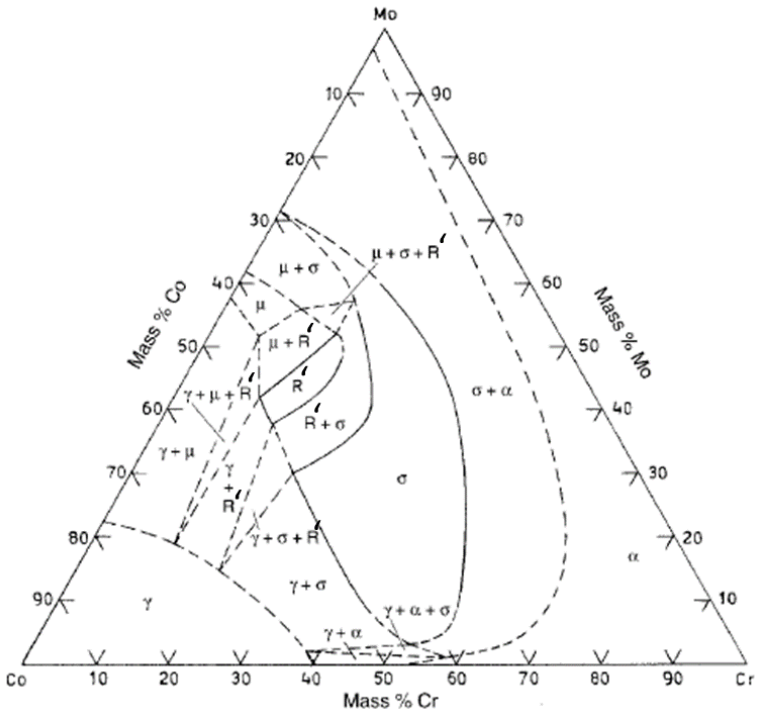

Figure 4-8 suggested 1300 °C isothermal section of Co-Cr-Mo system [121]

4.2 Thermodynamic and Kinetic Reasons for Absence of Planar Growth

As has been understood in the literature, solidification in each track during SLM starts with epitaxial growth. This is also demonstrated in the present study using EBSD analysis where colours in the orientation (normal, rolling or transverse) maps represent the crystal unit cell orientations, although only one map is provided (Figure 4-5b). At any boundary location, a grain before and after the boundary has the identical unit cell (colour). In this work, we have further illustrated the growth orientation of cells that can change during epitaxial growth.

In Figure 4-6, each pair of identical unit cells represents solidification in each grain along track boundaries being epitaxial. Cell growth direction before the boundary can be the same as one after the boundary or in exactly 90° change. This epitaxial growth feature depending on the heat flux direction and orientation of the existing (in previous track) cells adjacent to melt boundary will be discussed further when growth direction response to scan direction is discussed.

Extensive examination along the track boundaries, as shown in Figures 4-2 and 4-6, has revealed the absence of planar growth. In any track, cellular growth has started immediately from the melt boundary, and the new cells have grown directly from the unmelted portions of cells in the track below or adjacent. In normal fusion welding, growth velocity (*R*) should be zero at the fusion boundary and increasing to a value close to the welding speed in the central location of the melt.

Temperature gradient (*G*) should be high at weld boundary and decreasing toward the weld center. These *R* and *G* trends, not their values, should be applicable to an individual scan track during SLM. Thus, the absence of observable planar growth may not first appear reasonable, as *G/R* should be very high, and thus, the solidification mode should be planar adjacent to the track boundary. However, as already reviewed in Introduction, Rajamaki's study [69] has suggested that high welding speeds favour non-planar growth. Scanning speed during SLM is very high (0.7 m/s in the present work) in comparison with laser welding in which speed appears to be normally much <0.2 m/s [122]. Thus, the absence of a planar zone adjacent to track boundary during SLM is consistent with Rajamaki's suggestion.

Rapid solidification conditions relevant to laser surface treatment and welding have been explained in the analysis by Kurz and Trivedi [59] and are applicable to SLM as analyzed by Harrison et al. [123]. Important in Kurz and Trivedi's analysis is the prediction of the mode of solidification, based on the constitutional supercooling criterion:

$$R_c = GD_L/\Delta T_o \qquad \text{Equation 4-1}$$

where R_c is the critical growth velocity, G as has already been introduced is the temperature gradient, D_L is the diffusion coefficient in liquid and ΔT_o is the equilibrium liquidus–solidus interval. It should be noted that equation is the same as equation 1-6 as $m_l = \frac{-\Delta T_o}{c_o/_k - c_o}$. If $R<R_c$ the growth is planar, if R is higher than R_c the growth is cellular and if R further increases the growth becomes dendritic. There have not been direct or

indirect experimentally measured maximum G (G_{Max}) values that can be found in the literature for SLM. Simulation has suggested G_{Max} to be up to 10^5 K/mm [38, 124]. Data of the Co–Cr–Mo system by Wang et al. [125] may suggest ΔT_o to be ≈10°C. Value of D_L is in the order of 10^{-5} cm^2/s. Then, R_c is 0.01 m/s.

We now consider R when growth has started from the melt boundary (as actual growth rate R_{actual}) during SLM. A simple schematic illustration is given in Figure 4-9 to aid the discussion on the possible R_{actual} value (to compare with R_c) in the location indicated as ‘‘Solidification begins’’. The average width of track, W_{tk} (equal to twice the radius in the head portion of melt, 2 x $r_{mp\text{-}h}$), from the current SLM condition, is ≈125 µm. Observing the solidified ‘‘tear drops’’ along the sample surface (last built layer) indicates that the length of the melt pool is up to 3 x W_{tk}. Also, for approximation, the radius of melt pool in the tail portion ($r_{mp\text{-}t}$) is taken as $r_{mp\text{-}h}/4$. Then, η in Fig. 82 is 7.98° and referring to L_f (distance travelled along the scanning direction) and L_s (solidified thickness) after Δt (= t_2 - t_1) in location of ‘‘Solidification begins’’:

$$R_{actual} = \frac{L_s}{t} = \frac{Sin\ 7.98° \cdot L_f}{L_f / V_{scan}} = sin7.98° \cdot V_{scan} = sin7.98° \cdot \frac{700mm}{s} = 0.10m/s$$ Equation 4-2

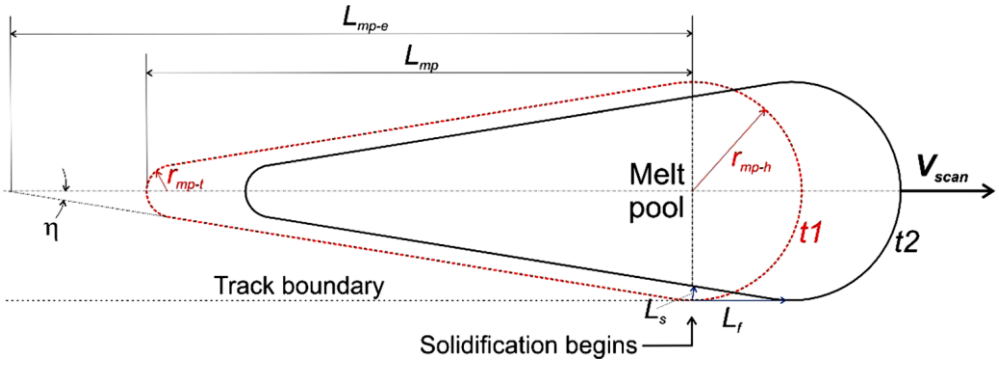

Figure 4-9 Schematic illustration of a melt pool that travels at the same speed as SLM scan speed (v_{scan}). The red and dash outline represents the melt boundary at t_1 and the black and solid outline represents at t_2.

This means R_{actual} >> R_c. Thus, growth from the melt boundary should not be planar and is immediately cellular instead, as shown in Figure 4-9. Note that if η reduces to 5°, R_{actual}

is still 0.06 m/s, many times larger than R_c. Although a more reliable value of G and a more accurate ΔT_o value cannot be obtained presently, the consideration here still strongly suggests that scanning speed during SLM is sufficiently high for planar growth to be absent. Estimation of G will be provided later in this thesis.

Location of ‘‘Solidification begins’’ is further discussed in relation to the results on the orientation of cellular growth presented in Figures 4-2, 4-3, 4-4, 4-5 and 4-6. The location is schematically illustrated with a solidified grain consisting of a group of cells in a previous (n-1 layer) track and growing (solidifying) cells in the new (n layer) track, as shown in Figure 4-10. For a general discussion, the orientation of cellular growth in [010] in a n-1 layer track is arbitrary and is in an angle ϕ to the normal direction of the track boundary. A large ϕ value means a high angle between the growing direction in the n layer track and the direction opposite to the heat flux direction if the crystal growth direction does not change. A change in growth direction is thus favourable, as suggested in Figure 4-10 where the growth has changed to another <100> direction and the change is 90°. In this case, $\phi + \Theta = 90°$. If u is a negative value, growing in the n layer track in the same [100] direction should be favourable, then $\Theta = -\phi$.

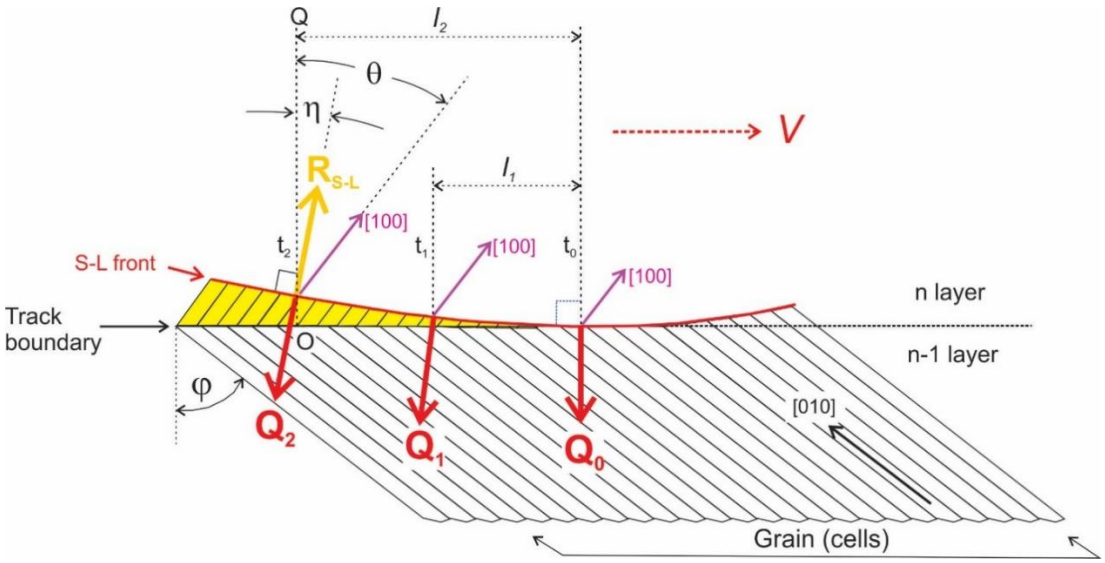

Figure 4-10 Schematic illustration of directions of laser scan (v), heat flux (Q), solidification (R_{S-L}) and cellular growth direction (Θ) in relation to orientation of cells (ϕ) of previous track in location of ‘‘Solidification begins’’.

Note that, as clearly shown in Figures 4-2 and 4-6, the growth direction is not the same as heat flux direction, which is normal to the track boundary, as growth is also dictated by the preferred crystal growth orientation. One of the preferred growth directions, meaning one of <100> crystallographic directions that is the nearest to the temperature gradient, should be the direction of the cellular growth into the next track.

The angle between the growth direction and temperature gradient should be one from zero when the growth direction is the same as temperature gradient to 54.7° when the temperature gradient is in the same angle to each of the three <100> directions. Values of Θ determined and presented in Figure 4-6 are within this range. Thus, a grain (group of cells) starts cellular growth in the track boundary epitaxially with two possibilities, either continuing the same cell growth direction in the previous track or at a 90° change across the boundary. The growing grain can either be stopped as a result of impinging onto another grain or continue to grow to the surface. A grain with a smaller angle to thermal gradient direction is more favourable to continue the growth. Extensive examination on surface regions in cross sections (parallel to build direction) has revealed cellular growth always reaching the track surface as shown in Figure 4-4. No equiaxed grains are expected to be observed which agrees with the data.

4.3 Effect of Laser Power on Cellular Growth Direction (180-360 W)

Optical micrographs of samples built with different laser powers were shown and discussed in the previous chapter. For better understanding the relation between the microstrcutre and track geometry in Figure 4-11, five optical micrographs of samples built with P ranged from 180 to 360 W track along with the width (W_{Tk}) and penetration (P_{Tk}) are illustrated. For clarity of the figure, no values are stated for the reinforcement (R_{Tk}). Two features are important to note. First, as indicative in Figure 4-11, increasing P increases the size of the track (cross sectional area, A_{Tk}). Second, although the shape of TBs have varied from close to being parabolic to slightly bell shape and then back to more

parabolic as P increases from 180 to 360 W, aspect ratio ($AR = W_{Tk} \times \cos 20° / P_{Tk}$ = 3.0, 2.7, 3.5, 2.8 and 2.7 for 180, 220, 280, 320 and 360 W, respectively) values from 2.7 to 3.5 has not changed greatly.

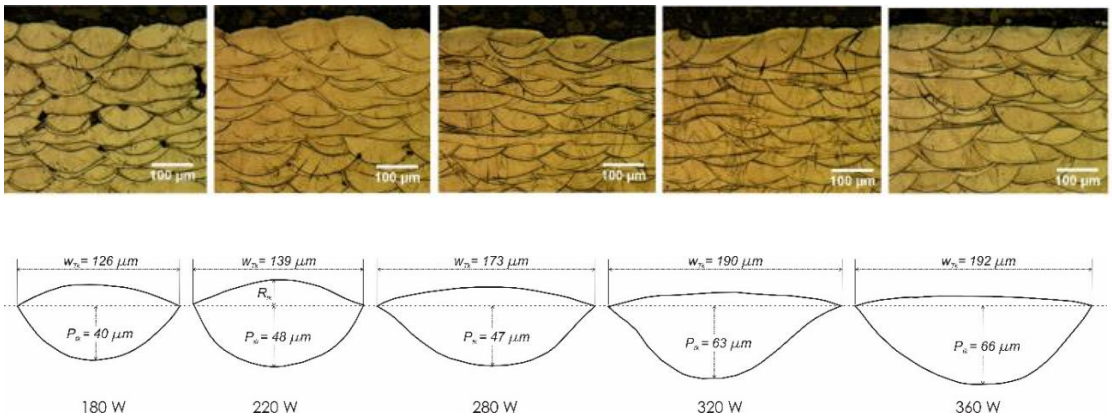

Figure 4-11 Optical micrographs of samples made with various P values, (a) 180 W, (b) 220 W, (c) 80 W, (d) 320 W and (e) 360 W. Representative outlines of track cross sections of top layers for are indicated.

Microstructures in and adjacent to TB are shown by SEM micrographs in Figure 4-12a to Figure 4-12c displaying that the distinctive features of solidification identified for 180 W are the same for SLM over the range of 180-360 W. The first feature is epitaxial growth with cells having grown either in the same direction or with a change of 90°. This suggests that, although the track size increases with P, heat flux direction has not varied significantly. This is consistent with the lack of a significant change in AR of the tracks as P varies. The second feature is cellular growth immediately from TB without planar solidification. This means $(G/R)_P$ values to be all within the values for cellular growth. The third feature is growth stopping of a grain (a group of cells) or both when they impinge onto each other as can be seen in these micrographs. A further feature, as shown In Figure 4-12d to Figure 4-12f, is that cellular growth continues in the tracks to the top surface (central) region without equiaxed grains forming. This also means that the (G/R) values are within the values for columnar (cellular) growth, well above that for equiaxed grain solidification.

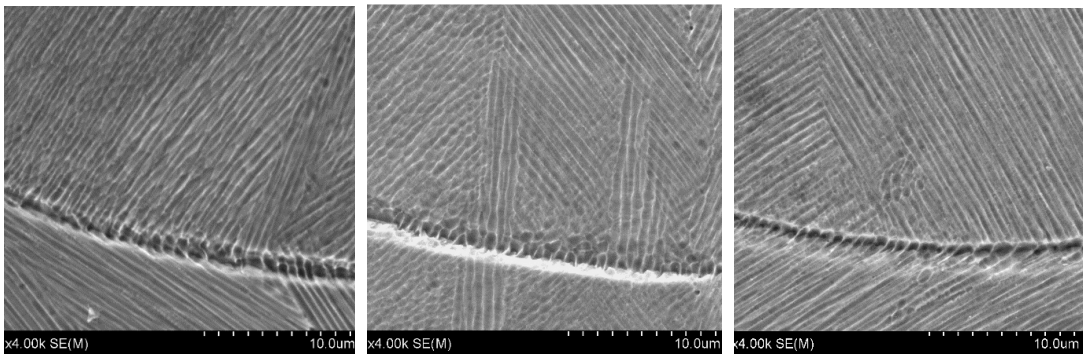

a. 180 W b. 280 W c. 360 W

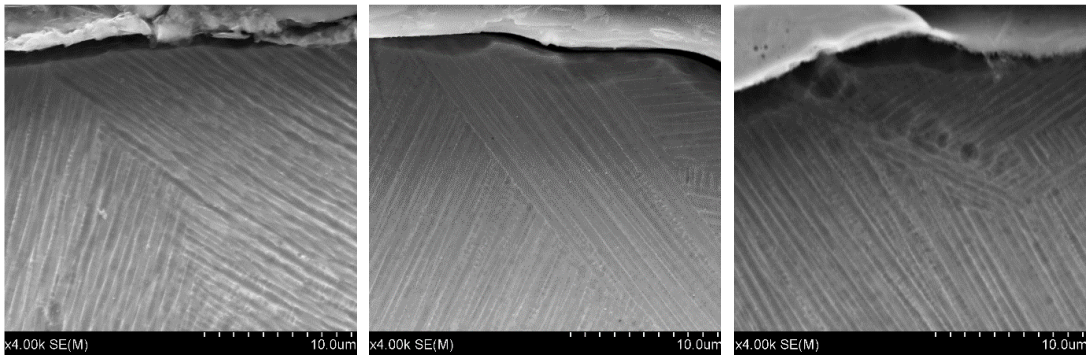

d. 180 W e. 280 W f. 360 W

Figure 4-12 SEM micrographs illustrating cellular microstructure of SLM samples: (a), (b) and (c) adjacent to TB, (d), (e) and (f) in central top location of tracks with P indicated.

Solidification proceeds with S-L front moving directly opposite to the heat flux direction. Thus, in a location along TB, solidification starts with S-L front normal to TB in that location. However, as shown in Figure 4-12a, grains have not grown normal to TB. In Figure 4-13, an example is provided to show the determined ϕ (in regard to micrograph plane) from which θ (in regard to the plane normal to SD) can be determined by rotating around BD for 20°. In the EBSD orientation map of Figure 4-13 (left), epitaxial growth can readily be identified, as each grain on both side of TB is in same colour. However, a change of growth direction (by 90°) in the same grain when it epitaxially grows across TB can only be detected in the SEM micrograph (Figure 4-13 – right). This mode of solidification, as has already been explained and shown in Figure 4-12, is clearly the same during SLM over the 180–360 W range. As has also been explained, the insignificant change in AR of tracks and thus insignificant change of heat flux direction over the range

of *P* is consistent with the similar feature of growth direction that grain growth can readily change direction during epitaxial growth.

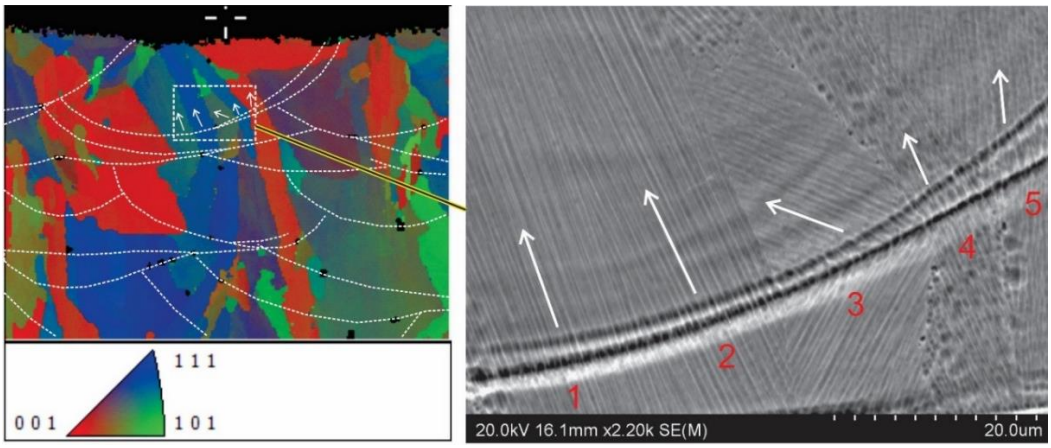

Figure 4-13 Orientation map (left) of a sample made with P = 320 W and SEM image (right) corresponding to the small area marked in orientation map. TBs are outlined in the orientation map and growth directions are indicated.

It is worthwhile to refer further to Popovich et al.'s [67] study that has demonstrated the ability to control growth orientation during SLM. They have not measured AR. However, it is clear in their micrographs that the tracks in the zone with grain orientation being "chaotic" are narrow (small w_{Tk}) and tracks in the zone with very strong {100} texture are wide (large w_{Tk}) while P_{Tk} may seem not to have varied significantly. Examination of their track profiles suggested AR ≈ 1.4 for zone "chaotic" and AR ≈ 6.2 for zone highed orienated. If P_{Tk} is the same, a wider (higher AR) track should mean heat flux direction is more dominantly one direction and downward, providing a more favourable condition for celular growth upward without changing direction during epitaxial growth. On the other hand, a narrow track should be the opposite and there is overall a higher need for direction change during epitaxial growth. The current samples of 180-360 W with AR values of tracks varring from 2.7-3.5 are not sufficiently different and thus epitaxial growth with both cellular growth direction continuing and with a 90°change can be seen in all the tracks.

EBSD orientation map of samples built with 180 W, 220 W, 280 W, 320 W and 360 W laser powers as shown in Figure 4-14 is used to identify the cellular growth direction and microstructure in a range of samples built with different laser powers. The orientation map of all the samples are similar however, there is still a difference between the grains in the samples built with low laser powers (180 W & 220 W) and high laser power (280 W, 320 W, 360 W). Columnar grains, which are divided by high angle boundaries, reveal different lengths crossed over multiple tracks influenced by the used laser power. It can also be seen that the average grain size of 280 W sample is larger and consequently less grains in one melt pool than the samples built with 180 W & 220 W laser powers. However, the grain growth does not seem to be influenced by increasing the laser power to 360W.

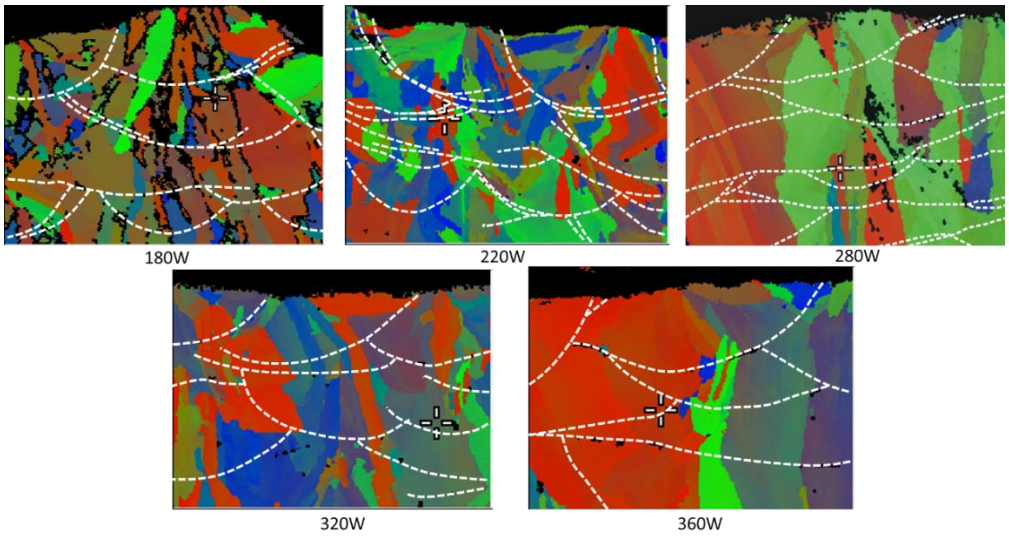

Figure 4-14 EBSD orientation maps of samples built with 180 W, 220 W, 280 W, 320 W and 360 W laser power show columnar grains along the building direction.

This can be explained using the shape of the melt pool. The melt pool shape influences the orientation of the heat flow and accordingly the solidification pattern. As discussed in the chapter 3 although increasing the laser power led to change in size of the melt pool, yet the melt mode remained unchanged in all the samples. The melt pool cross section of

samples built with high laser powers is more flat, while 180 W and 220 W samples have rather round melt shapes.

Inside the melt pools of 280 W, 320 W and 360 W samples the grains are coarser and mostly grow along the building direction as illustrated in Figure 4-14. This is due to short height of the melt pool and good re-melting of the previous layer, which results in easy epitaxial growth and creation of elongated grains. However, inside the 180 W and 220 W melt pools the growth direction of grains depends on the location of grain in the melt pool. In areas near the centreline of melt pool grains mostly elongate along the building direction. In the areas far from the centreline, growth of the grain is mostly towards the centreline depending on the shape of the melt pool boundaries. In general, shape of melt pool did not change dramatically in this experiment and only a slight change was observed over the range of laser powers. Thus, the growth direction in the samples did not alter significantly.

4.4 Effect of Laser Power on Cellular Spacing

Measured values of λ_1 near TB (~ 5 μm from TB) from various P samples are given in Figure 4-15, ranging from 0.48 to 0.74 μm. As can be seen in Figure 4-12, λ_1 values may be more close to 0.7 μm near the top of tracks. These measured values (for Co-29Cr-6Mo) are reasonably close to the range (0.31-0.74 μm) of Wang et al. [66] for 316L stainless steel and the range (0.38-0.77 μm) of Arisoy et al. [90] for Inconel 625 Ni-alloy. In those two studies, extensive measurements on λ_1 have been made to investigate how SLM parameters, except P, affect λ_1. On the other hand, the extensive measurements in the present study of λ_1 plotted in Figure 4-15a have demonstrated that P does not appear to affect λ_1. The average values, from 0.59 μm at 180 W to 0.62 μm at 360 W (thus $\Delta\lambda_1$ = 0.03 μm), change little. The scatters of λ_1 data for each condition in Figure 4-15a, similar to the data in Arisoy et al.'s study/plots [90], are however relatively high. As is

shown in Figure 4-12 and Figure 4-13, a grain (a group of cells) has grown in a direction normally different to the direction of the grain next. Thus, the source of the scatters may be attributed to the differences in growth direction. Measured values of λ_1 are plotted as a function of θ in Figure 4-15b. In this figure a trend is identifiable that, as θ increases from 3 to 50°, λ_1 almost linearly decreases from ~ 0.71 μm to ~ 0.47 μm (using linear regression) and the rate of this decrease being $d\lambda_1/d\theta \approx 0.05$ μm per 10° is however small.

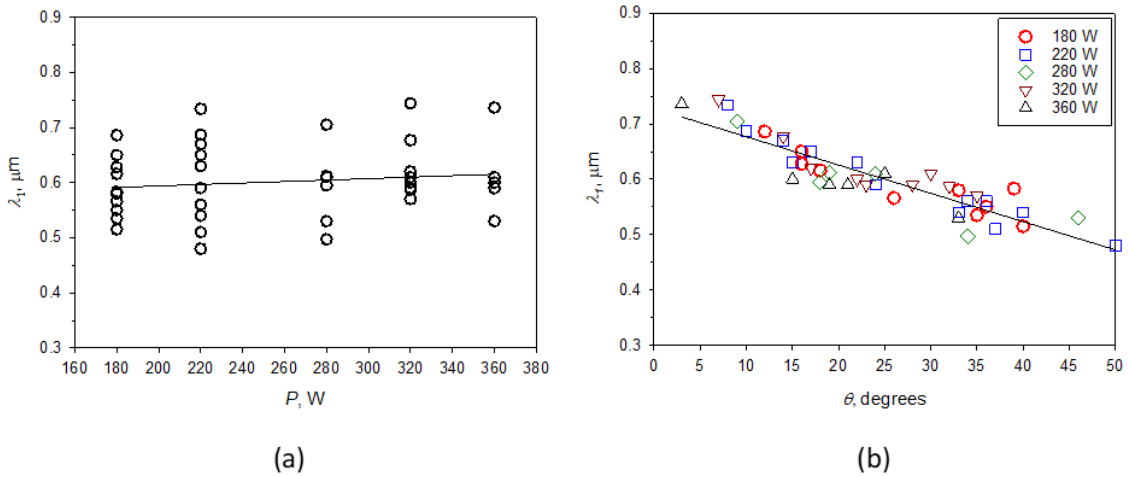

Figure 4-15 Intercellular spacing plotted as a function of (a) laser power and (b) the angle between growth direction and normal to track boundary.

To further explain the meaning of θ in relation to heat flux direction, a 2D plane normal to a tangential plane of TB and parallel to SD, as shown in Figure 4-10, is used to aid the discussion. Direction Q (each red arrow) represents maximum heat flux direction of local solidification. S-L front (outline) moves with v and this is achieved by local solidification in the direction (direction $R_{S\text{-}L}$) which is normal to the S-L front and opposite to heat flux direction Q. After melting, as the laser beam moves forward, solidification starts at t_0 with direction $R_{S\text{-}L}$ opposite to direction Q_0. However, cells grow in a <100> direction which is not the same as direction $R_{S\text{-}L}$. A <100> growth direction expressed by θ in Figure 4-10 depends on the cell growing angle in the previous layer, φ. For a high φ, $\theta + \varphi = 90°$. If φ is negative, $\theta = \varphi$. Considering fcc grain growth during solidification and thus three possible <100> directions near the direction of G_{max}, θ could range from zero to 54.7°.

Thus, the determined θ values up to 50° in Figure 4-15b are reasonable. The reason for the slight reduction in λ_1 as θ increases is however unclear. An increase in θ should mean an increase in R thus a reduction in λ_1 according to Equation 1-16 but the equation also suggests λ_1 to increase when G reduces. The increase in θ should mean a reduction in G.

4.5 Possible Explanation on Relationship Between Cellular Spacing and Growth Angle

As was discussed in the previous chapter, despite the increase in laser power the size of the cells does not change. It is possible that the growth direction of cells may influence the cell size using different laser powers. Equation 1-16 is based on directional solidification and the growth angle of cells is not considered in the equation. For better understanding the effect of growth direction, a schematic drawing of two melt pools moving with speed of v but formed with different laser powers is presented in Figure 4-16.

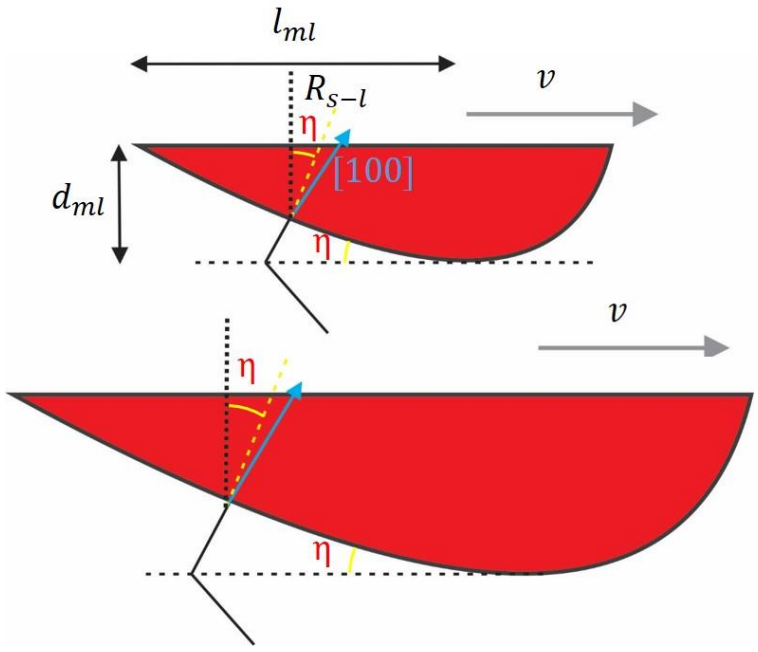

Figure 4-16 Schematic illustration of angle between the growth direction and building direction Ŋ for a melt pool formed using a) low laser power b) high laser power.

The effect of laser power on the size of the melt pool was given in the previous chapter. Figure 4-16a represents a melt pool formed using low laser power in comparison to melt pool in Figure 4-16b. Consequently, the depth and length of the melt pool in Figure 4-16a are smaller than Figure 4-16b.

The cells in Figure 4-16a have growth rate of *R* and the angle between the direction normal to *S/L* interface and building direction is η. This angle is equal to $\tan^{-1}\frac{d_{ml}}{l_{ml}}$ and the values of depth and length are already defined as per our measurements from the melt pools in the final layer of the build. The correlation between η and laser power is plotted in Figure 4-17. It is clear from the graph that the η value does not change significantly with increasing the power from 180 W to 360 W and it is in the range of 6.68 - 8.35µm.

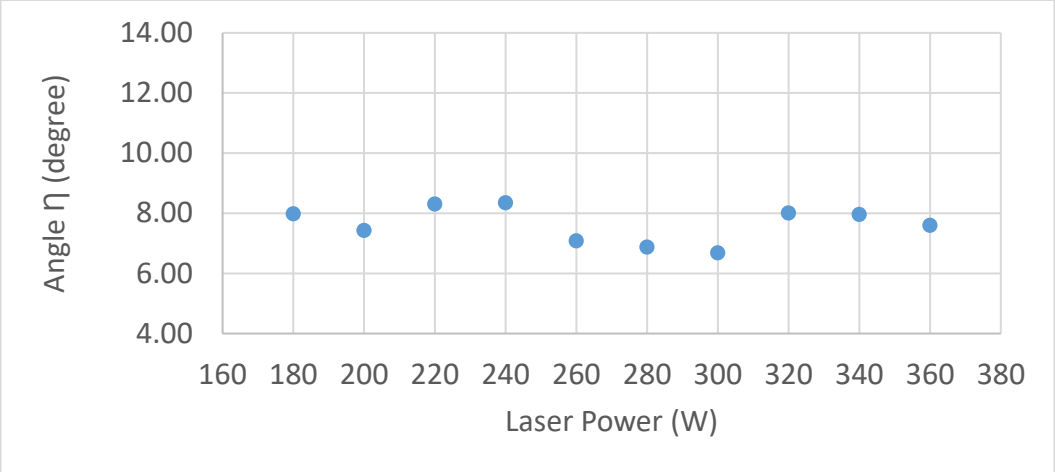

Figure 4-17 The angle between the growth direction and building direction η as a function of laser power.

Although Equation 1-16 is a good representative for the relationship between thermal gradient, growth rate and cell size but, it is possible that it does not justify the effect of growth angle on the cell size as there is no change in the size of cell with increasing the laser power. This angle is influenced by fusion boundary which is governed by the shape and size of the melt pool. It can be stated that if the depth to length of ratio (AR) was high, similar to the depth of melt pool in keyhole mode melting, the fusion boundary would have been different to what we have observed in our samples. This change in shape

and size of melt pool would lead to a higher growth angle and consequently can lead to a change in the cell size. In this study, increase in laser power increases the volume of melt pool which influences the heat extraction of the melt pool, but increase of laser power is also accompanied by increase in the melt boundary which is another influencing factor on the heat extraction from the melt pool. It can be suggested that thermal gradient and growth rate influenced by the melt pool shape and size (AR) do not change by increasing the laser power from 180 W to 360 W which could be the reason for the similar cell size in all the samples.

4.6 Thermal Condition of SLM Solidification

In the comprehensive review on processing science of MAM, Sames et al. [126] state that both P and v affect G and R. While R should increase with v, it is unclear how G may relate to P. The understanding of their relationships is however very important. This is because, as explained by Sames et al., calculation and prediction for columnar-to-equiaxed transition (CET) if G and R are known may then be possible.

Such knowledge should help process control for obtaining equiaxed grains when it is necessary as well as for controlling grain size since, empirically, $\dot{T}$ (= $G \cdot R$) inversely relates to the sizes of microstructures. Experimentally determined G may not be possible although, as will be explained, $\dot{T}$ has been determined based on measured λ_1 values and on the empirical $\dot{T}$-λ_1 relationship. Therefore, as has also been explained by Sames et al. [126] and Collins et al. [32] in their comprehensive reviews of MAM, recent effort on modelling and simulation to predict the complex thermal conditions and microstructure evolution during MAM has been strong. It is thus worthwhile that, since λ_1 has been extensively measured and R can be estimated, G and $\dot{T}$ are estimated and compared to available data from simulation and from estimation based on the empirical $\dot{T}$-λ_1 relationship from literature.

As Equation 1-16 was developed based on cell growth direction normal to S-L plane, only λ_1 with low θ values is applicable. Similar to fusion welding, tear-drop ripples on SLM tracks together with fish-scale shape in track cross sectional view can suggest the melt pool shape, as in Figure 2-15. The average value of η for 180W sample from observation of track surface and cross section view is to be ~8°, as an approximation.

Then, from Figure 4-15b, $\lambda_1(\theta \approx 7.98°) \approx 0.69$ μm should be taken for applying Equation 1-16. Taking $\eta = 7.98°$, $R \approx \sin 7.98° \cdot v = \sin 7.98° \times 700$ mm/s = 97 mm/s. Data of Γ listed by Kurz and Fisher [61] for a number of metallic alloys are quite similar at $\Gamma \approx 2 \times 10^{-7}$ K m and this is adopted in the present calculation.

Also as listed for D_L by Kurz and Fisher [61], $D_L = 3 \times 10^{-9}$ m^{-2}/s, which is for a number of high melting point metals and is used in the present calculation. According to Harris and Sikkenda [127], for F75 CoCrMo alloy, ΔT_o is 44°C determined by differential scanning calorimetry method. Value of k for the alloy is however not published. The most recent experimental determination of liquidus and solidus of Co-Cr binary system is the study by Allibert et al. [128]. Their data based on differential thermal analysis suggest $\Delta T_o \approx 10$°C and $k \approx 0.9$ for Cr = 29wt%. If $\Delta T_o = 44$°C in F75 CoCrMo alloy due to Mo as the major element added, k should decrease slightly and is assumed to be ~ 0.8. Then, following Equation 1-16 to approximately relate λ_1 to G, $G = 1.8 \times 10^7$ K/m. Accordingly, $\dot{T} = G \cdot R = 1.8 \times 10^7$ K/m × 0.12 m/s = 2.2×10^6 K/s.

The available G and $\dot{T}$ data from literature are listed in Table 4-1. Direct G measurement during SLM cannot be made and data from Lee and Zhang [93] and from Keller et al. [91] are based on SLM simulation studies. Data from these two sources are relevant to solidification microstructures as the G values at S-L front or solidus contour are provided. It appears that the experimentally estimated G (≈ 1.8×10^7 K/m) in the current study,

although ΔT_o and k are not highly certain, is close to the predicted values by simulation from the two sources in literature.

Data from Lee and Zhang [93] for the tail end of the melt pool has not been included in Table 4-1. This is because the value of R in their simulation is 0.7 m/s for the tail end, meaning solidification direction is close to scan direction. As is indicative in Figure 4-4, there is no equiaxed solidification and epitaxially grown grains have continued the growth to the top. Thus, R does not change and is low, being ~ 0.1 m/s rather one close to v at 0.7 m/s. In Keller et al.'s [91] simulation of solidification, they also predict that R_{max} is only 0.2v. Using Equation 1-16, based on their predicted values of G and R, Lee and Zhang further predicted λ_1 ranged from 1.8 to 2.2 μm and they thus stated that this λ_1 range is consistent with their measured λ_1 range, being 1-1.8 μm as listed in Table 1-2.

Table 4-1 Maximum temperature gradient and cooling rate in various published work of SLM. Values from this work are also listed. Note: np means "not provided".

Material	**Method**	***G*, 10^7 K/m**	**$\dot{T}$, 10^6 K/s**	**Reference**
Inconel 718	Simulation	0.8-1.8	0.7-0.9	Lee & Zhang et al. [93]
Ni-4%Nb alloy	Simulation	0.6-2.2	-	Keller et al. [91]
316L stainless steel	Measured $\lambda_1 = 80\dot{T}^{-0.33}$	np	0.2-4.8	Sun et al. [41]
Ni alloy	Measured $\lambda_1 = 97\dot{T}^{-0.36}$	np	0.2-0.4	Harrison et al. [128]
Ni CM247LC	Measured $\lambda_1 = 97\dot{T}^{-0.36}$	np	0.9	Wang et al. [129]
Inconel 625	Measured $\lambda_1 = 50\dot{T}^{-0.33}$	np	0.1-15	Li et al. [89]
AlSi10Mg	Measured $\lambda_1 = 43\dot{T}^{-0.32}$	np	0.3-16	Tang et al. [99]
Co-29Cr-6Mo	Measured $\lambda_1 = \frac{1.6\times10^{-3}}{R^{0.25}G^{0.5}}$	1.8	2.2	This work

The experimentally estimated $\dot{T}$ value (2.2×10^6 K/s) in this work may also be seen quite close to the values, being $(0.7\text{-}0.9)\times10^6$ K/s, from Lee and Zhang by simulation. Keller et al. do not provide values of $\dot{T}$ at S-L front. They consider the average cooling rate within a thermal cycle meaning the temperature difference between the peak temperature and lowest temperature within the cycle over the time for the scan of a track. Their average cooling rate (~ 1×10^5 K/s) thus cannot be compared with one for local solidification. Experimentally estimated $\dot{T}$ values (Table 4-1) from other work are based on:

$$\lambda_1 = c\dot{T}^n \qquad \text{Equation 4-3}$$

Where c is an experimentally determined constant and n is equal to or close to -0.33. As has been explained, Equation 1-16 is theoretically derived by Kurz and Fisher [61]. This is done by considering the distance of the mushy zone being equal to the temperature difference between the tip and root of the arms in the mushy zone divided by G in the zone and by assuming the envelope of the cell tip being approximately an ellipse. As has also been pointed out by Kurz and Fisher, λ_1 does not obey the simple relationship as Equation 4-3 which is empirical but is often used in literature. However, the empirical relationship identifying the constant c has not been established for Co alloys in literature.

For comparison purpose, $G(\lambda_1)$ and $\dot{T}(\lambda_1)$ based on Equation 1-16 and Equation 4-3 for the commonly observed range of λ_1 are given in Figure 4-18 for λ_1 ranging 0.3 to 1.8 μm although from the extensive measurements from Arisoy et al. [90], Wang et al. [66] and from this work, λ_1 is dominantly less than 1 μm. For Inconel 718, to compare with our $G(\lambda_1)$ and $\dot{T}(\lambda_1)$ based on Equation 1-16 for Co-29Cr-6Mo, R is taken the same at 0.12 m/s together with ΔT_o = 84 K and k = 0.48 as used by Lee and Zhang. As shown in Figure 4-18, the different ΔT_o and k values have resulted in slight increases in both G and $\dot{T}$ for

the same λ_1. Using Equation 4-3 and the constants as stated in Table 4-1, $\dot{T}(\lambda_1)$ curves for Inconel 718 and for Inconel 625 are also plotted in Figure 4-18.

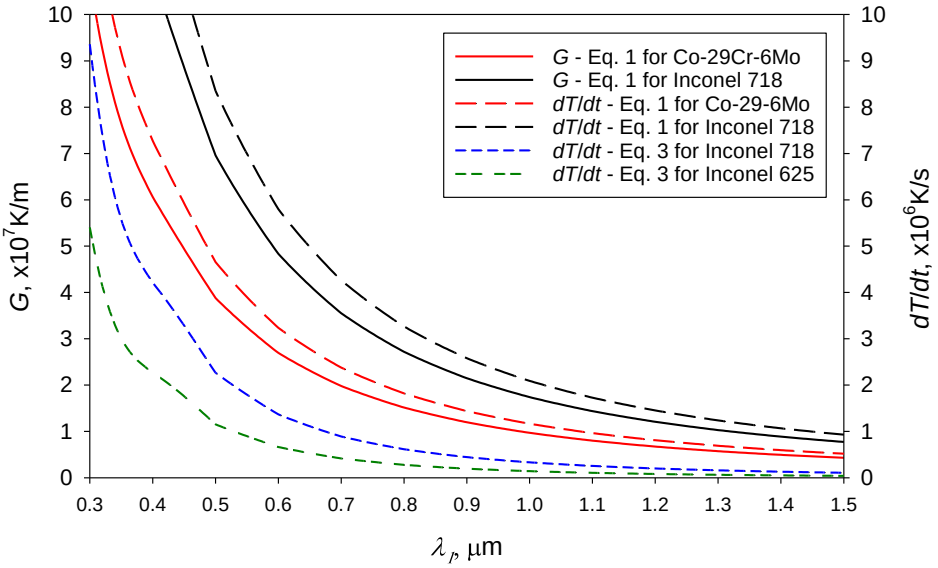

Figure 4-18 G and $\dot{T}$ each as a function of λ_1 plotted according Equation 1-16 for Co-29Cr-Mo and Inconel 718 alloys and $\dot{T}$ as a function of λ_1 plotted according Equation 4-3 for Inconel 718 and Inconel 625 alloys.

Comparing the curve for Inconel 718 using Equation 1-16 to that using Equation 4-3, there is a significant difference, with $\dot{T}$ using Equation 4-3 to be many times lower than that using Equation 1-16. In Table 4-1, lower $\dot{T}$ values from Harrison et al. [123] in which λ_1 = 0.9-1.2 μm than that from Wang et al. [129] in which λ_1 = 0.7 μm as in Table 1-2 is reasonable as $\dot{T}$ decreases with increasing λ_1 in Equation 4-3. Note that λ_1 data are not listed in Table 1-2 from Harrison et al. as SLM condition is not fully provided. In both Li et al.'s [89] and Tang et al's [99] data, $\dot{T}$ varies for almost two order of magnitudes. This is because not only λ_1 varies significantly (for a single E) but also the minimum λ_1 values are low (at 0.3 and 0.2 μm, respectively).

Fig 4-17 clearly shows that $\dot{T}$ needs to increase considerably for a small decrease in λ_1 when λ_1 is small, for using both Equation 1-16 and Equation 4-3. However, as has already been pointed out, λ_1 is dominantly less than 1 μm. The constants for Equation 4-3 which

is empirical for various alloys have been determined largely for solidification conditions where $\dot{T}$ values are considerably lower and λ_1 considerably higher than those found in SLM.

As pointed out above, there could be a significant difference in the values of $\dot{T}$ predicted using Equation 1-16 and Equation 4-3. Thus, it is suggested that the use of empirical relationship expressed in Equation 4-3 with the constants c and n established from solidification conditions where G and $\dot{T}$ could be orders of magnitudes lower could be uncertain for SLM solidification conditions. As has been explained, λ_1 from Wang et al. [66] ranges 0.3-0.7 μm and λ_1 = 0.7 μm for v = 700 mm/s. In Arisoy et al.'s [90] extensive experimentation and measurement, on average, λ_1 = 0.6 μm (for v = 725-875 mm/s). In this work, λ_1 = 0.68 μm for v = 700 mm/s. Then, based on Equation 1-16, G = ~ 2×10^7 K/m and $\dot{T}$ = ~ 2×10^6 K/s should be the representative thermal condition under which microstructures form during SLM solidification. $G(\lambda_1)$ and $\dot{T}(\lambda_1)$ can further be predicted approximately for the use of a significantly higher v value which should decrease λ_1 as demonstrated by Wang et al. [66].

The G vs. R graph (solidification map as normally referred to) taken from Kurz & Fisher's study [61] which summaries the different microstructures that are obtained using a typical alloy superimposed on the calculated G and R values for all the cells in our experiments is presented in Figure 4-19. $G \cdot R$ is equivalent to cooling rate which is shown in the graph as inclined lines. G, R and $\dot{T}$ values from our experiment are reasonable considering the high values of G and $\dot{T}$ in SLM in comparison to casting. The average value of R and G are 0.1 m/s and 2×10^7 K/m, respectively. As presented on the graph the values are on the columnar dendritic side of the graph which is why we did not observe equiaxed grains in our observation. It is possible to get equiaxed grains if the G value decreases. This might be possible to be obtained by preheating to higher temperatures during the SLM process.

More investigation and experimental works in SLM need to be taken to find a way to obtain equiaxed grain in this process. Overall, the estimated values of *G* and *R* are good indicators of thermal condition in SLM which can be used as a measure for other materials in SLM as well.

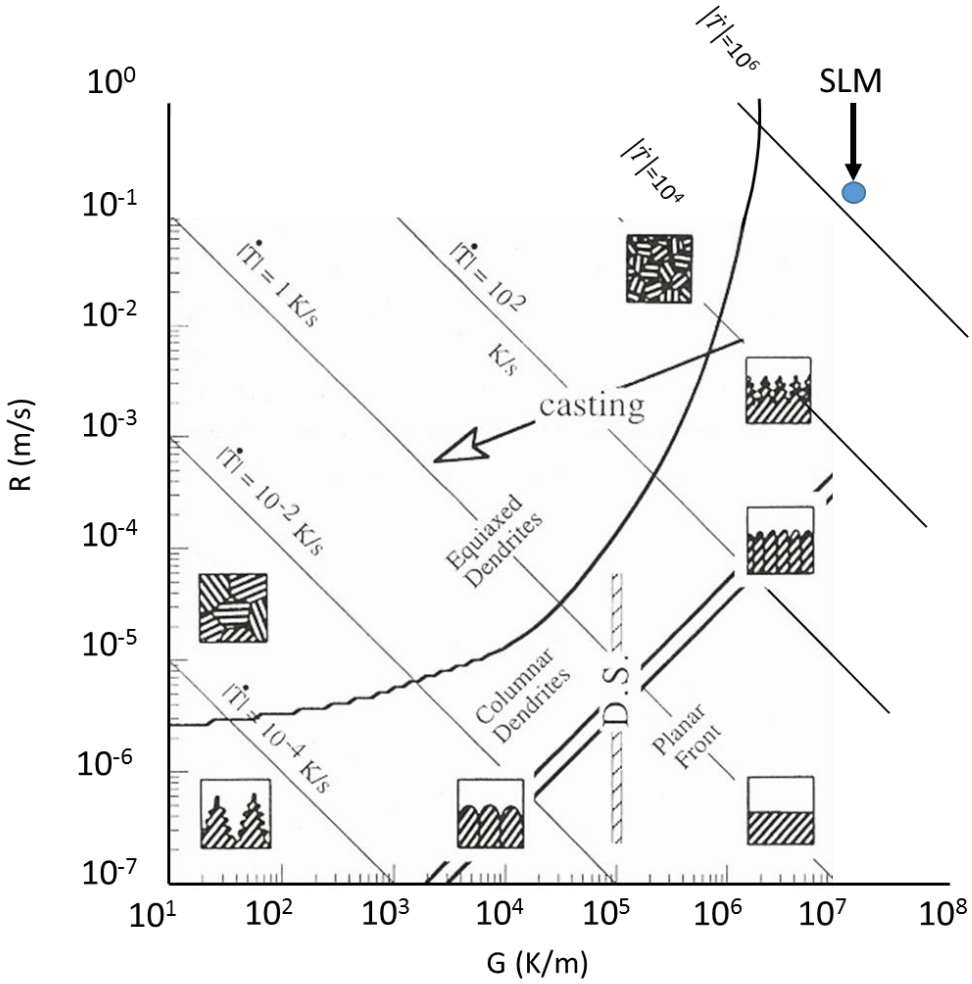

Figure 4-19 Schematic summary of solidification morphologies. The results of this study using SLM is superimposed on the graph of Kurz & Fisher. [61]

5 Conclusion

The main conclusions of this thesis can be summarised as below:

1. Tracks produced during SLM using the recommended selective laser melting (SLM) parameters (power = 180 W, scan velocity = 700 mm/s, hatch spacing = 0.125 mm and layer thickness = 0.03 mm), which corresponds to an energy density value equal to 69 J/mm^3, are not sufficient in their sizes. Geometrically, these tracks have been shown to insufficiently overlay and overlap to result in lack of fusion (LOF) free. Inconsistence in the size and irregular track appearance observed have suggested the insufficient stability of the size of the melt pool during SLM. These inconsistence and irregularity further prevented sufficient overlaying and overlapping, resulting in formation of LOF.

2. Laser power (P) has a strong effect on track profile which is the primary factor affecting the amount of LOF. As P increases from 180 to 220 W, while other parameters remained the same, fraction of LOF (f_{LOF}) decreased rapidly due to the increase in the size of the tracks for the sufficient track coverage. The increase in P has improved melt/track stability and track overlapping consistency during SLM but the further reduction of f_{LOF} was not proportional to the increase in P value. It was found that, above 240 W, reinforcement (R_{Tk}) decreased almost linearly and width of track (w_{Tk}) increased with a decreasing rate as P increased. However, over the range of 260 W to 300 W, penetration (P_{Tk}) values were lower than those of 240 W and of > 320 W. Little reinforcement (very low R_{Tk}) and strong penetration (high P_{Tk}) were observed for the highest P (360 W) sample. Also, the results of LOF fraction area from synchrotron data confirmed the results obtained based on optical micrograph measurement

3. It has been identified that large spatter of over well 100 μm during SLM can cause large and abnormal LOF, due to the insufficient penetration of the laser beam to melt the large spatter. Measurements and observations in this work indicated that a high P_{Tk} value is the determining factor for overcoming the effect of large size spatter on forming large size LOF and for f_{LOF} to be $\ll 0.1\%$. It has also been found that the difference between the morphology of the powder particle and spatter on powder bed is the fine cellular-dendritic microstructure in spatter due probably spatter having solidified in a high cooling rate but, in original powder particles the microstructure is coarse.

4. It was observed that the laser melting (heat transfer) mode did not change by increasing the laser power and was conduction mode over the entire range of P (180-360 W). The reason for this consistent melting mode could be due to the large spot size (140 μm) which will need a very high laser power for transiting to keyhole mode. The theoretical explanation for the threshold of changing from conduction to keyhole melting mode was also given. This theoretical explanation has suggested the consistent conduction melting mode in all the samples despite the increase in laser power to 360 W.

5. It has been demonstrated that cellular solidification started from track boundaries (TBs) and grew epitaxially into the new track, without a planar zone. It has been found that, in relation to the growth direction of cells in the layer below the TB, the (epitaxial) growth direction in the new track either continue exactly in the same cell growth direction or change by 90°. The selection (either 0 or 90°) is for minimizing the angle (θ) between the <100> growth direction and the temperature gradient direction. Once a grain (a group of cells growing in the same direction) has started the cellular growth in TB epitaxially, the growth can either be stopped as a result of impinging on another grain or continue to the track surface. A grain with a high angle

between the growth direction and thermal gradient direction can result in the stoppage readily after impinging on another. Low-angle grains (cells) grow more readily to the track surface.

6. Using the constitutional supercooling criteria and based on the high thermal gradient value suggested for SLM, critical growth rate ($R_{critical}$) below which planar growth should prevail has been calculated. The actual growth rate (R_{Actual}) has also been estimated from knowing the scan velocity and the estimated moving melt pool. R_{Actual} has been found to be considerably higher than $R_{critical}$. This explains why no planar growth has been found in SLM. Also, no equiaxed solidification has been observed in the solidified melt pool in any of the samples, as the result of a high growth rate.

7. Our observation on the tracks showed increasing laser power from 180 W to 360 W while other SLM parameters were kept unchanged has gradually increased the track size but variation of the aspect ratio (AR), which is simply defined as the width over the penetration, was only small. Thus, the selection of cellular growth direction during epitaxial growth in TB, either the continuation or a change of 90°, has occurred for the entire 180–360 W range. This is because an insignificant change of AR means heat flux direction during solidification changes little as the selection of growth direction has largely based on heat flux direction. Over the entire 180–360 W range, the growth features that some cells grow from TB to track surface and some grains (a group of cells) cease growing when they impinge on other grains are also the same.

8. Intercellular spacing (λ_1) has been found to be affected little by P over 180–360 W. This may also be the result of AR having changed little that the heat from a larger melt simply transferred through a large TB in the same direction. Thus, the thermal condition in solidification front may have changed little and thus the size of cells remained relatively consistent. However, λ_1 linearly decreased slightly as the growth

angle (θ), defined as one between the growth direction to the solid-liquid (S-L) front moving direction, increased. The reason for this growth angle dependence of λ_1 is not clear.

9. Using a theoretical model of primary arm spacing, thermal condition in the solidification front has been estimated. From the determined λ_1 and R, which can be estimated based on track appearance and since scan speed (v) is unchanged, average G and thus cooling rate ($\dot{T}$) have been calculated to be $\sim 2 \times 10^7$ K/m and $\sim 2 \times 10^6$ K/s, respectively. It is suggested that G during SLM is about an order of magnitude higher than the value below which the more desirable solidification mode of equiaxed grains may dominate.

6 Recommendations for Further Research

In this research only laser power changed for building the samples while all the other laser parameters were kept constant. Changing the spot size as an influencing factor on the melt pool mode and microstructure solidification would be beneficial in SLM research field. In this study the spot size was 140 µm for all the builds. It is recommended to use a smaller spot size. Laser spot size of 75 µm is another common spot size that was used in the SLM experiment on CoCrMo by other researchers.

As was discussed in our results it is possible that the width of laser spot was the main reason for the conduction melting mode in all the samples. Changing the spot size to 75 µm would result in smaller width of melt pool and higher depth of penetration that this study which would lead to keyhole mode melting. The alteration in melting mode changes the depth, width and aspect ratio of the melt pool. This change would lead to a higher growth angle and consequently can lead to change in the cell size. This cannot be confirmed until a research on CoCrMo alloy with the same laser parameters as this study and a smaller spot size is implemented.

Another potential area for future work is the influence of laser parameters on fatigue properties of SLM. In this research the effect of laser power on LOF and solidification were investigated. An in-depth study on the effect of laser power on fatigue life and crack growth would be valuable since it can help in evaluating the fatigue failures that occur in SLM products. We understand how LOF forms but how it affects the crack propagation and how increasing laser power to lower the fraction of LOF may have an effect on fatigue life is important to be understood. Therefore, fatigue testing using different laser powers is recommended.

References

1. Milewski, J.O., *Additive Manufacturing of Metals.* Springer Series in Materials Science, 2017. **258**.
2. Herzog, D., et al., *Additive manufacturing of metals.* Acta Materialia, 2016. **117**: p. 371-392.
3. Ford, S. and M. Despeisse, *Additive manufacturing and sustainability: an exploratory study of the advantages and challenges.* Journal of Cleaner Production, 2016. **137**: p. 1573-1587.
4. Tofail, S.A.M., et al., *Additive manufacturing: scientific and technological challenges, market uptake and opportunities.* Materials Today, 2018. **21**(1): p. 22-37.
5. Murr, L.E., et al., *Fabrication of Metal and Alloy Components by Additive Manufacturing: Examples of 3D Materials Science.* Journal of Materials Research and Technology, 2012. **1**(1): p. 42-54.
6. Vandenbroucke, B. and J. Kruth, *Selective laser melting of biocompatible metals for rapid manufacturing of medical parts.* Rapid Prototyping Journal, 2007. **13**(4): p. 196-203.
7. Zhang, B., H. Liao, and C. Coddet, *Effects of processing parameters on properties of selective laser melting Mg–9%Al powder mixture.* Materials & Design, 2012. **34**(0): p. 753-758.
8. Thijs, L., et al., *A study of the microstructural evolution during selective laser melting of Ti–6Al–4V.* Acta Materialia, 2010. **58**(9): p. 3303-3312.
9. Monroy, K., J. Delgado, and J. Ciurana, *Study of the Pore Formation on CoCrMo Alloys by Selective Laser Melting Manufacturing Process.* Procedia Engineering, 2013. **63**(0): p. 361-369.
10. Wataha, J.C., *Alloys for prosthodontic restorations.* The Journal of Prosthetic Dentistry, 2002. **87**(4): p. 351-363.
11. Davis, J.R. and A.S.M.I.H. Committee, *Nickel, Cobalt, and Their Alloys*. 2000: ASM International.
12. Klarstrom, D.L., *Wrought cobalt- base superalloys.* Journal of Materials Engineering and Performance, 1993. **2**(4): p. 523-530.

13. Harris, I.D., *Additive manufacturing: A transformational advanced manufacturing technology.* Advanced Materials and Processes, 2012. **170**(5): p. 25-29.
14. Koutsoukis, T., et al., *Selective Laser Melting Technique of Co-Cr Dental Alloys: A Review of Structure and Properties and Comparative Analysis with Other Available Techniques.* Journal of Prosthodontics, 2015. **24**(4): p. 303-312.
15. Kellner, T., *An Epiphany Of Disruption: GE Additive Chief Explains How 3D Printing Will Upend Manufacturing.* 2017.
16. Kellner, T., *The FAA Cleared the First 3D Printed Part to Fly in a Commercial Jet Engine from GE.* 2015.
17. Li, P., et al., *Critical assessment of the fatigue performance of additively manufactured Ti–6Al–4V and perspective for future research.* International Journal of Fatigue, 2016. **85**: p. 130-143.
18. Frazier, W.E., *Metal Additive Manufacturing: A Review.* Journal of Materials Engineering and Performance, 2014. **23**(6): p. 1917-1928.
19. Adrián, U., E.-M. Manuel, and P. Suresh, *The present and future of additive manufacturing in the aerospace sector: A review of important aspects.* Proceedings of the Institution of Mechanical Engineers, Part G: Journal of Aerospace Engineering, 2015. **229**(11): p. 2132-2147.
20. Everton, S.K., et al., *Review of in-situ process monitoring and in-situ metrology for metal additive manufacturing.* Materials & Design, 2016. **95**: p. 431-445.
21. Rafi, H.K., et al., *Microstructures and Mechanical Properties of Ti6Al4V Parts Fabricated by Selective Laser Melting and Electron Beam Melting.* Journal of Materials Engineering and Performance, 2013. **22**(12): p. 3872-3883.
22. Takaichi, A., et al., *Microstructures and mechanical properties of Co–29Cr–6Mo alloy fabricated by selective laser melting process for dental applications.* Journal of the Mechanical Behavior of Biomedical Materials, 2013. **21**(0): p. 67-76.
23. Odahara, T., H. Matsumoto, and A. Chiba, *Mechanical Properties of Biomedical Co-33Cr-5Mo-0.3N Alloy at Elevated Temperatures.* MATERIALS TRANSACTIONS, 2008. **49**(9): p. 1963-1969.
24. EOS. *EOS CobaltChrome MP1*. 2011 [cited 2015 7-may]; Available from: http://www.eos.info/material-m.

25. Arcam. *ASTM F75 CoCr Alloy*. [cited 2015 07- may]; Available from: http://www.arcam.com/technology/products/metal-powders/.
26. Lee, B.S., H. Matsumoto, and A. Chiba, *Fractures in tensile deformation of biomedical Co–Cr–Mo–N alloys.* Materials Letters, 2011. **65**(5): p. 843-846.
27. Song, C., et al., *Research on rapid manufacturing of CoCrMo alloy femoral component based on selective laser melting.* The International Journal of Advanced Manufacturing Technology, 2014. **75**(1-4): p. 445-453.
28. Lu, Y., et al., *Microstructure, mechanical property and metal release of As-SLM CoCrW alloy under different solution treatment conditions.* Journal of the Mechanical Behavior of Biomedical Materials, 2016. **55**: p. 179-190.
29. Yamanaka, K., M. Mori, and A. Chiba, *Mechanical properties of as-forged Ni-free Co–29Cr–6Mo alloys with ultrafine-grained microstructure.* Materials Science and Engineering: A, 2011. **528**(18): p. 5961-5966.
30. Yamanaka, K., M. Mori, and A. Chiba, *Effects of carbon concentration on microstructure and mechanical properties of as-cast nickel-free Co–28Cr–9W-based dental alloys.* Materials Science and Engineering: C, 2014. **40**(0): p. 127-134.
31. Babu, S.S., *Scripta Viewpoint Set: Materials science aspects related to additive manufacturing.* Scripta Materialia, 2017. **135**: p. 97-99.
32. Collins, P.C., et al., *Microstructural Control of Additively Manufactured Metallic Materials.* Annual Review of Materials Research, 2016. **46**(1): p. 63-91.
33. Wei, K., et al., *Effect of energy input on formability, microstructure and mechanical properties of selective laser melted AZ91D magnesium alloy.* Materials Science and Engineering: A, 2014. **611**: p. 212-222.
34. Aboulkhair, N.T., et al., *Reducing porosity in AlSi10Mg parts processed by selective laser melting.* Additive Manufacturing, 2014. **1–4**(0): p. 77-86.
35. Read, N., et al., *Selective laser melting of AlSi10Mg alloy: Process optimisation and mechanical properties development.* Materials & Design, 2015. **65**: p. 417-424.
36. Abele, E., et al., *Selective laser melting for manufacturing of thin-walled porous elements.* Journal of Materials Processing Technology, 2015. **215**(0): p. 114-122.

37. Gong, H., et al., *Influence of defects on mechanical properties of Ti–6Al–4 V components produced by selective laser melting and electron beam melting.* Materials & Design, 2015. **86**: p. 545-554.
38. Li, Y. and D. Gu, *Thermal behavior during selective laser melting of commercially pure titanium powder: Numerical simulation and experimental study.* Additive Manufacturing, 2014. **1–4**: p. 99-109.
39. Weingarten, C., et al., *Formation and reduction of hydrogen porosity during selective laser melting of AlSi10Mg.* Journal of Materials Processing Technology, 2015. **221**(0): p. 112-120.
40. Kamath, C., et al., *Density of additively-manufactured, 316L SS parts using laser powder-bed fusion at powers up to 400 W.* The International Journal of Advanced Manufacturing Technology, 2014. **74**(1): p. 65-78.
41. Sun, Z., et al., *Selective laser melting of stainless steel 316L with low porosity and high build rates.* Materials & Design, 2016. **104**: p. 197-204.
42. Qiu, C., et al., *On the role of melt flow into the surface structure and porosity development during selective laser melting.* Acta Materialia, 2015. **96**: p. 72-79.
43. Kasperovich, G., et al., *Correlation between porosity and processing parameters in TiAl6V4 produced by selective laser melting.* Materials & Design, 2016. **105**: p. 160-170.
44. Zhou, X., et al., *3D-imaging of selective laser melting defects in a Co–Cr–Mo alloy by synchrotron radiation micro-CT.* Acta Materialia, 2015. **98**: p. 1-16.
45. Jia, Q. and D. Gu, *Selective laser melting additive manufacturing of Inconel 718 superalloy parts: Densification, microstructure and properties.* Journal of Alloys and Compounds, 2014. **585**: p. 713-721.
46. Carter, L.N., et al., *Process optimisation of selective laser melting using energy density model for nickel based superalloys.* Materials Science and Technology, 2016. **32**(7): p. 657-661.
47. Faidel, D., et al., *Investigation of the selective laser melting process with molybdenum powder.* Additive Manufacturing, 2015. **8**: p. 88-94.
48. Qiu, C., N.J.E. Adkins, and M.M. Attallah, *Selective laser melting of Invar 36: Microstructure and properties.* Acta Materialia, 2016. **103**: p. 382-395.

49. Teng, C., et al., *Simulating Melt Pool Shape and Lack of Fusion Porosity for Selective Laser Melting of Cobalt Chromium Components.* Journal of Manufacturing Science and Engineering, 2016. **139**(1): p. 011009-011009-11.
50. Xia, M., et al., *Porosity evolution and its thermodynamic mechanism of randomly packed powder-bed during selective laser melting of Inconel 718 alloy.* International Journal of Machine Tools and Manufacture, 2017. **116**: p. 96-106.
51. Taheri Andani, M., et al., *Spatter formation in selective laser melting process using multi-laser technology.* Materials & Design, 2017. **131**: p. 460-469.
52. Taheri Andani, M., et al., *A study on the effect of energy input on spatter particles creation during selective laser melting process.* Additive Manufacturing, 2018. **20**: p. 33-43.
53. Wang, D., et al., *Mechanisms and characteristics of spatter generation in SLM processing and its effect on the properties.* Materials & Design, 2017. **117**: p. 121-130.
54. Liu, Y., et al., *Investigation into spatter behavior during selective laser melting of AISI 316L stainless steel powder.* Materials & Design, 2015. **87**: p. 797-806.
55. Simonelli, M., et al., *A Study on the Laser Spatter and the Oxidation Reactions During Selective Laser Melting of 316L Stainless Steel, Al-Si10-Mg, and Ti-6Al-4V.* Metallurgical and Materials Transactions A, 2015. **46**(9): p. 3842-3851.
56. Gunenthiram, V., et al., *Experimental analysis of spatter generation and melt-pool behavior during the powder bed laser beam melting process.* Journal of Materials Processing Technology, 2018. **251**: p. 376-386.
57. Brody, H.D., *Segregation and structure in the weld zone.* Advances in Welding Science and Technology, 1986: p. 83-91.
58. McLean, M.A.S., G. J. & Steen, W. M, *Laser direct casting high nickel alloy components.* Advances in powder metallurgy and particulate materials, 1997. **3**(21): p. 3-15.
59. Kurz, W. and R. Trivedi, *Rapid solidification processing and microstructure formation.* Materials Science and Engineering: A, 1994. **179**: p. 46-51.
60. Lancaster, J.F., *Metallurgy of Welding.* 1980.
61. W. Kurz, D.J.F., *Fundamentals of Solidification.* 1998(4).
62. Kou, S., *Welding Metallurgy.* 2002(2).

63. Kruth JP, D.S., Vrancken B, Kempen K, Vleugels J, Humbeeck JV *Additive manufacturing of metals via Selective Laser Melting: Process aspects and material developments.* Additive Manufacturing, 2016: p. 69-99.
64. Basak, A. and S. Das, *Epitaxy and microstructure evolution in metal additive manufacturing.* Annual Review of Materials Research, 2016. **46**: p. 125-149.
65. Cloots, M., P.J. Uggowitzer, and K. Wegener, *Investigations on the microstructure and crack formation of IN738LC samples processed by selective laser melting using Gaussian and doughnut profiles.* Materials & Design, 2016. **89**: p. 770-784.
66. Wang, D., et al., *Investigation of crystal growth mechanism during selective laser melting and mechanical property characterization of 316L stainless steel parts.* Materials & Design, 2016. **100**: p. 291-299.
67. Popovich, V.A., et al., *Functionally graded Inconel 718 processed by additive manufacturing: Crystallographic texture, anisotropy of microstructure and mechanical properties.* Materials & Design, 2017. **114**: p. 441-449.
68. Kou, S., *Weld Metal Solidification II: Microstructure within Grains*, in *Welding Metallurgy*. 2003, John Wiley & Sons, Inc. p. 199-215.
69. Rajamaki, P., *Fusion weld metal solidification: continuum from weld interface to centerline.* 2008. **Ph.D. thesis**.
70. Casati, R., J. Lemke, and M. Vedani, *Microstructure and Fracture Behavior of 316L Austenitic Stainless Steel Produced by Selective Laser Melting.* Journal of Materials Science & Technology, 2016. **32**(8): p. 738-744.
71. Casati, R., et al., *Aging Behaviour and Mechanical Performance of 18-Ni 300 Steel Processed by Selective Laser Melting.* Metals, 2016. **6**(9): p. 218.
72. Garibaldi, M., et al., *Metallurgy of high-silicon steel parts produced using Selective Laser Melting.* Acta Materialia, 2016. **110**: p. 207-216.
73. Li, S., et al., *Microstructure Characteristics of Inconel 625 Superalloy Manufactured by Selective Laser Melting.* Journal of Materials Science & Technology, 2015. **31**(9): p. 946-952.
74. Chlebus, E., et al., *Effect of heat treatment on the microstructure and mechanical properties of Inconel 718 processed by selective laser melting.* Materials Science and Engineering: A, 2015. **639**: p. 647-655.

75. Dilip, J.J.S., et al., *Selective laser melting of HY100 steel: Process parameters, microstructure and mechanical properties.* Additive Manufacturing, 2017. **13**: p. 49-60.

76. Vrancken, B., et al., *Heat treatment of Ti6Al4V produced by Selective Laser Melting: Microstructure and mechanical properties.* Journal of Alloys and Compounds, 2012. **541**(0): p. 177-185.

77. Vrancken, B., et al., *Microstructure and mechanical properties of a novel β titanium metallic composite by selective laser melting.* Acta Materialia, 2014. **68**: p. 150-158.

78. Wauthle, R., et al., *Effects of build orientation and heat treatment on the microstructure and mechanical properties of selective laser melted Ti6Al4V lattice structures.* Additive Manufacturing, 2015. **5**: p. 77-84.

79. Cain, V., et al., *Crack propagation and fracture toughness of Ti6Al4V alloy produced by selective laser melting.* Additive Manufacturing, 2015. **5**: p. 68-76.

80. Yadroitsev, I., P. Krakhmalev, and I. Yadroitsava, *Selective laser melting of Ti6Al4V alloy for biomedical applications: Temperature monitoring and microstructural evolution.* Journal of Alloys and Compounds, 2014. **583**: p. 404-409.

81. Cloots, M., et al., *Microstructural characteristics of the nickel-based alloy IN738LC and the cobalt-based alloy Mar-M509 produced by selective laser melting.* Materials Science and Engineering: A, 2016. **658**: p. 68-76.

82. Zhou, X., et al., *Textures formed in a CoCrMo alloy by selective laser melting.* Journal of Alloys and Compounds, 2015. **631**: p. 153-164.

83. Zhang, P., J. Liu, and A.C. To, *Role of anisotropic properties on topology optimization of additive manufactured load bearing structures.* Scripta Materialia, 2017. **135**: p. 148-152.

84. Panwisawas, C., et al., *Mesoscale modelling of selective laser melting: Thermal fluid dynamics and microstructural evolution.* Computational Materials Science, 2017. **126**: p. 479-490.

85. Iveković, A., et al., *Selective laser melting of tungsten and tungsten alloys.* International Journal of Refractory Metals and Hard Materials, 2018. **72**: p. 27-32.

86. Zinoviev, A., et al., *Evolution of grain structure during laser additive manufacturing. Simulation by a cellular automata method.* Materials & Design, 2016. **106**: p. 321-329.
87. Lopez-Botello, O., et al., *Two-dimensional simulation of grain structure growth within selective laser melted AA-2024.* Materials & Design, 2017. **113**: p. 369-376.
88. Yadroitsev, I., et al., *Energy input effect on morphology and microstructure of selective laser melting single track from metallic powder.* Journal of Materials Processing Technology, 2013. **213**(4): p. 606-613.
89. Li, C., Y.B. Guo, and J.B. Zhao, *Interfacial phenomena and characteristics between the deposited material and substrate in selective laser melting Inconel 625.* Journal of Materials Processing Technology, 2017. **243**: p. 269-281.
90. Arısoy, Y.M., et al., *Influence of scan strategy and process parameters on microstructure and its optimization in additively manufactured nickel alloy 625 via laser powder bed fusion.* International Journal of Advanced Manufacturing Technology, 2017. **90**(5-8): p. 1393-1417.
91. Keller, T., et al., *Application of finite element, phase-field, and CALPHAD-based methods to additive manufacturing of Ni-based superalloys.* Acta Materialia, 2017. **139**: p. 244-253.
92. Choi, J.-P., et al., *Densification and microstructural investigation of Inconel 718 parts fabricated by selective laser melting.* Powder Technology, 2017. **310**: p. 60-66.
93. Lee, Y.S. and W. Zhang, *Modeling of heat transfer, fluid flow and solidification microstructure of nickel-base superalloy fabricated by laser powder bed fusion.* Additive Manufacturing, 2016. **12**: p. 178-188.
94. Vilaro, T., et al., *Microstructural and mechanical approaches of the selective laser melting process applied to a nickel-base superalloy.* Materials Science and Engineering: A, 2012. **534**(0): p. 446-451.
95. Hedberg, Y.S., et al., *In vitro biocompatibility of CoCrMo dental alloys fabricated by selective laser melting.* Dental Materials, 2014. **30**(5): p. 525-534.
96. Liverani, E., et al., *Fabrication of Co–Cr–Mo endoprosthetic ankle devices by means of Selective Laser Melting (SLM).* Materials & Design, 2016. **106**: p. 60-68.
97. Jialin, Y., *Selective laser melting additive manufacturing of advanced nuclear materials V-6Cr-6Ti.* Materials Letters, 2017. **209**: p. 268-271.

98. Thijs, L., et al., *Fine-structured aluminium products with controllable texture by selective laser melting of pre-alloyed AlSi10Mg powder.* Acta Materialia, 2013. **61**(5): p. 1809-1819.

99. Tang, M., et al., *Rapid Solidification: Selective Laser Melting of AlSi10Mg.* JOM, 2016. **68**(3): p. 960-966.

100. Huang, W.-C., et al., *Microstructure-controllable Laser Additive Manufacturing Process for Metal Products.* Physics Procedia, 2014. **56**: p. 58-63.

101. Yin, H. and S.D. Felicelli, *Dendrite growth simulation during solidification in the LENS process.* Acta Materialia, 2010. **58**(4): p. 1455-1465.

102. Wheeler, A., *The Renishaw AM250 Additive Manufacturing System.* 3D PRINTING, 2015

103. Insight, E.E.S., *Orientation Imaging Microscopy (OIM™) Data Analysis.* 2014).

104. Warren, B.E., *X-ray Diffraction.* 1969.

105. Darvish, K., et al., *Selective laser melting of Co-29Cr-6Mo alloy with laser power 180–360W: Cellular growth, intercellular spacing and the related thermal condition.* Materials Characterization, 2018. **135**: p. 183-191.

106. Chan, C., J. Mazumder, and M.M. Chen, *A two-dimensional transient model for convection in laser melted pool.* Metallurgical Transactions A, 1984. **15**(12): p. 2175-2184.

107. Dai, D. and D. Gu, *Influence of thermodynamics within molten pool on migration and distribution state of reinforcement during selective laser melting of AlN/AlSi10Mg composites.* International Journal of Machine Tools and Manufacture, 2016. **100**: p. 14-24.

108. Dou, L., et al., *Surface tension of molten Al-Si alloy at temperatures ranging from 923 to 1123 K.* Chinese Science Bulletin, 2008. **53**(17): p. 2593-2598.

109. Zhou, X., et al., *Balling phenomena in selective laser melted tungsten.* Journal of Materials Processing Technology, 2015. **222**: p. 33-42.

110. Louvis, E., P. Fox, and C.J. Sutcliffe, *Selective laser melting of aluminium components.* Journal of Materials Processing Technology, 2011. **211**(2): p. 275-284.

111. Miranda, G., et al., *Predictive models for physical and mechanical properties of 316L stainless steel produced by selective laser melting.* Materials Science and Engineering: A, 2016. **657**: p. 43-56.

112. Mukherjee, T., et al., *Printability of alloys for additive manufacturing.* Scientific Reports, 2016. **6**: p. 19717.

113. Lu, L.-X., N. Sridhar, and Y.-W. Zhang, *Phase field simulation of powder bed-based additive manufacturing.* Acta Materialia, 2018. **144**: p. 801-809.

114. Yang, J., et al., *Role of molten pool mode on formability, microstructure and mechanical properties of selective laser melted Ti-6Al-4V alloy.* Materials & Design, 2016. **110**: p. 558-570.

115. Sadowski, M., et al., *Optimizing quality of additively manufactured Inconel 718 using powder bed laser melting process.* Additive Manufacturing, 2016. **11**: p. 60-70.

116. Scipioni Bertoli, U., et al., *On the limitations of Volumetric Energy Density as a design parameter for Selective Laser Melting.* Materials & Design, 2017. **113**: p. 331-340.

117. Khairallah, S.A., et al., *Laser powder-bed fusion additive manufacturing: Physics of complex melt flow and formation mechanisms of pores, spatter, and denudation zones.* Acta Materialia, 2016. **108**: p. 36-45.

118. Song, B., et al., *Process parameter selection for selective laser melting of Ti6Al4V based on temperature distribution simulation and experimental sintering.* The International Journal of Advanced Manufacturing Technology, 2012. **61**(9-12): p. 967-974.

119. Hann, D.B., J. Iammi, and J. Folkes, *A simple methodology for predicting laser-weld properties from material and laser parameters.* Journal of Physics D: Applied Physics, 2011. **44**(44): p. 445401.

120. Mills, K.C., *Co - X-45*, in *Recommended Values of Thermophysical Properties for Selected Commercial Alloys*. 2002, Woodhead Publishing. p. 80-87.

121. Gupta, K.P., *The Co-Cr-Mo (Cobalt-Chromium-Molybdenum) System.* Journal of Phase Equilibria and Diffusion, 2005. **26**(1): p. 87-92.

122. Franco, A., L. Romoli, and A. Musacchio, *Modelling for predicting seam geometry in laser beam welding of stainless steel.* International Journal of Thermal Sciences, 2014. **79**: p. 194-205.

123. Harrison, N.J., I. Todd, and K. Mumtaz, *Reduction of micro-cracking in nickel superalloys processed by Selective Laser Melting: A fundamental alloy design approach.* Acta Materialia, 2015. **94**: p. 59-68.

124. Xia, M., et al., *Influence of hatch spacing on heat and mass transfer, thermodynamics and laser processability during additive manufacturing of Inconel 718 alloy.* International Journal of Machine Tools and Manufacture, 2016. **109**: p. 147-157.
125. Wang, W., et al., *Experimental Investigation and Thermodynamic Calculation of the Co-Cr-Mo System.* Journal of Phase Equilibria and Diffusion, 2014: p. 1-11.
126. Sames, W.J., et al., *The metallurgy and processing science of metal additive manufacturing.* International Materials Reviews, 2016. **61**(5): p. 315-360.
127. K. Harris, S.S., *Investment cast cobalt alloys.* in the Proceedings of the 24th BICTA Investment Casting Conference: New Horizons and Process Capabilities, 1999.
128. Allibert, C., et al., *CoCr binary system: experimental re-determination of the phase diagram and comparison with the diagram calculated from the thermodynamic data.* Journal of The Less-Common Metals, 1978. **59**(2): p. 211-228.
129. Wang, X., et al., *Microstructure and yield strength of SLM-fabricated CM247LC Ni-Superalloy.* Acta Materialia, 2017. **128**: p. 87-95.